



UCGE Reports

Number 20242

Department of Geomatics Engineering

**Registration for the In-Vivo Studies of Osteoarthritis
based on Magnetic Resonance Imaging**

(URL: <http://www.geomatics.ucalgary.ca/research/publications/GradTheses.html>)

by

Wai Ting Rita Cheng

April 2006



UNIVERSITY OF CALGARY

Registration for the In-Vivo Studies of Osteoarthritis based on Magnetic Resonance
Imaging

by

Wai Ting Rita Cheng

A THESIS

SUBMITTED TO THE FACULTY OF GRADUATE STUDIES
IN PARTIAL FULFILLMENT OF THE REQUIREMENTS FOR THE
DEGREE OF MASTER OF SCIENCE

PROGRAM OF BIOMEDICAL ENGINEERING

CALGARY, ALBERTA

APRIL, 2006

© Wai Ting Rita Cheng 2006

Abstract

Osteoarthritis (OA) affects cartilage and bones of weight bearing joints. To understand OA, assessments of joint properties and health status are needed. For these analyses, magnetic resonance imaging (MRI) can provide accurate in-vivo 3D surfaces of joint structures. Alignment of these surfaces through a registration process can allow direct comparisons between datasets. Registrations are commonly used in Geomatics engineering where temporal geographic data are compared for change detection. Therefore, the main objective of this thesis is to translate a Geomatics algorithm to register MR joint surfaces for quantitative studies of joint conditions. Experiments with Geomatics and MRI data confirmed that the algorithm could successfully register and detect discrepancies between the surfaces. Validation and repeatability studies showed that the algorithm achieved an accuracy of an image pixel size and the digitization and registration processes were highly repeatable. Applications' results also confirmed the feasibility of the algorithm for in-vivo studies of OA.

Acknowledgements

I would like to express my sincere thanks and appreciation for my supervisors, Dr. J. Ronsky and Dr. A. Habib, for their guidance, enthusiasm, dedications, encouragement, and constant support throughout the course of my Masters program. I would also like to thank Dr. N. El-Sheimy and Dr. R. Frayne for serving on my examination committee.

I would also like to acknowledge the National Sciences and Engineering Research Council and Alberta Ingenuity Fund for their funding support.

I would like to acknowledge Dr. R. Frayne, Kim Connolly, David, and Joanne for their collaborative effort in MR data collections and making the long scanning sessions enjoyable. I would like to thank Ion Robu for his wood-working talent and for helping me in the construction of the validation frame. I also like to thank Dr. R. Lambert and Dr. J. Jaremko, University of Alberta, for their collaboration. I also appreciate the test volunteers who contributed a significant amount of time for the MR scanning. I would like to give special thanks to all my group members for their help, advice, encouragement, and friendships.

Finally, I would like to recognize my parents, my sister, my friends, and my dog for their constant love and support.

Table of Contents

Abstract.....	ii
Acknowledgements	iii
Table of Contents	iv
List of Tables	vii
List of Figures.....	ix
List of Abbreviations	xiv
Chapter One: Introduction	1
1.1 Background.....	1
1.2 Objective and Specific Aims	5
1.3 Thesis Outline	6
Chapter Two: Literature Review	8
2.1 Introduction.....	8
2.2 Imaging Applications in Assessment of Joint Injuries and Diseases.....	8
2.3 Magnetic Resonance Imaging.....	11
2.3.1 Principles of Magnetic Resonance.....	12
2.3.2 MR Imaging Parameters	14
2.3.3 MR Imaging Considerations of the Knee	16
2.3.4 Accuracy of MR Measurements of Joint Properties	21
2.3.5 Studies of Joint Biomechanics and Diseases with MRI.....	23
2.4 Surface Modeling.....	26
2.5 Registration Techniques.....	29
2.5.1 Medical Image Registration.....	30
2.5.1.1 Elastic Registration based on Intensity Variations	30
2.5.1.2 Genetic Algorithm for 3D MR-CT Registration.....	32
2.5.1.3 Elastic Registration for Detecting Cartilage Changes	35
2.5.2 Geomatics Registration.....	37
2.5.2.1 Registration of Laser Data to Photogrammetric Surfaces.....	39
2.5.2.2 Least Squares 3D Surface Matching.....	41
2.5.2.3 Automatic Registration of 3D Views based on Spin-Image.....	43
2.5.3 Registration Requirements and the Proposed Algorithm.....	46
2.6 Summary	47
Chapter Three: Surface Matching Algorithm	49
3.1 Introduction.....	49
3.2 Registration Paradigm.....	49
3.2.1 Registration Primitives.....	49
3.2.2 Transformation Function	51
3.2.3 Similarity Measure.....	53

3.2.4	Matching Strategy	56
3.3	Automated Surface Matching and Registration Methodology	58
3.4	Outcome Measures.....	62
3.5	Summary of Surface Matching Methodology.....	63
3.6	Summary	64
Chapter Four: Algorithm Limitation, Implemented Modifications, and Verifications with Geomatics Applications		66
4.1	Introduction.....	66
4.2	Algorithm Limitation for High Density Datasets	66
4.3	Modifications to Accommodate High Density and Noisy Datasets	69
4.3.1	Iterative Closest Point	69
4.3.2	Modified surface matching algorithm with MIHT and ICP	70
4.4	Geomatics Applications	74
4.4.1	Light Detection and Ranging Data of Urban City	75
4.4.1.1	Data and Experiments	76
4.4.1.2	Surface Matching Results and Discussion.....	77
4.4.2	Stereophotogrammetry for Facial Measurements.....	82
4.4.2.1	Data and Experiments	83
4.4.2.2	Surface Matching Results and Discussion.....	86
4.4.3	Close-range Laser Scanning of Small Object	89
4.4.3.1	Data and Experiments	90
4.4.3.2	Surface Matching Results and Discussion.....	91
4.5	Summary	93
Chapter Five: Registration of 3D MR Data		94
5.1	Introduction.....	94
5.2	Data Acquisition and Descriptions	94
5.3	Feature Segmentation.....	97
5.4	Surface Modeling.....	98
5.5	Registration Experiments.....	100
5.6	Results and Discussion	105
5.7	Summary	110
Chapter Six: Accuracy Validation and Repeatability Studies for the Surface Matching Algorithm		112
6.1	Introduction.....	112
6.2	Accuracy Validation	112
6.2.1	Experimental Design and Setup.....	113
6.2.1.1	Absolute Orientation Procedure.....	114
6.2.1.2	Required Accuracy for Validation	114
6.2.1.3	Joint Specimen	115
6.2.1.4	Fiducial Markers	116
6.2.1.5	Materials for Markers	125

6.2.1.6	Validation Frame Design and Setup	126
6.2.2	MR Scanning	128
6.2.3	Surface Matching and Absolute Orientation Results.....	129
6.2.4	Accuracy Analysis and Discussions	132
6.3	Repeatability Studies	135
6.3.1	Digitization and Registration	136
6.3.2	Repeatability Analysis and Discussion.....	137
6.4	Summary	141

Chapter Seven: Applications of In-Vivo Studies of Degenerative Joint Conditions

.....		143
7.1	Introduction.....	143
7.2	Registration for Disease Monitoring.....	144
7.2.1	Data.....	144
7.2.2	Methods.....	146
7.2.3	Results and Discussion	150
7.3	Patellar Tracking.....	154
7.3.1	Data.....	155
7.3.2	Methods.....	155
7.3.3	Results and Discussion	158
7.4	Changes in Contact Area Locations.....	162
7.4.1	Data.....	162
7.4.2	Methods.....	163
7.4.3	Results and Discussion	164
7.5	Summary	166

Chapter Eight: Conclusions and Future Work..... 167

8.1	Conclusions.....	167
8.2	Future Work.....	173

References..... 179

Appendix A: Ethics Approval..... 188

Appendix B: Subject Consent Form 191

List of Tables

Table 4-1: Initial approximations, expected parameters, estimated transformation parameters, and registration results of the LIDAR data.	78
Table 4-2: Transformation parameters derived from on linear features and surface matching for the LIDAR data.	81
Table 4-3: Involved facial datasets for the three registration experiments performed. ...	85
Table 4-4: Comparisons of the registration results between the proposed surface matching algorithm and the Spin-Image technique.	92
Table 5-1: Registration experiments performed for Subject 2 to Subject 5.	102
Table 5-2: Directional terms for the human body (Van De Graaff and Fox, 1989).	104
Table 5-3: Registration results for the femoral and patellar surfaces of the four subjects.	106
Table 6-1: The MR scans acquired for each type of fiducial markers for the pilot study.	122
Table 6-2: RMSE of the coordinate differences between FaroArm and MR measurements for the three spherical markers after point-based absolute orientation.	124
Table 6-3: RMSE of the coordinate differences between FaroArm and MR measurements for five linear markers after line-based absolute orientation.	124
Table 6-4: MR scans acquired for the validation frame with the porcine joint and markers.	128
Table 6-5: The MR scans (refer to Table 6-4) used for the registrations in the validation study.	130
Table 6-6: The RMSEs of the coordinate differences between the markers after the absolute orientation procedures.	132
Table 6-7: The transformation parameters derived from surface matching and point-based absolute orientation procedure between two datasets.	133

Table 6-8: The RMSEs of the coordinate differences of the box between surface matching and absolute orientation procedure with markers.	135
Table 6-9: RMSEs of XYZ coordinate differences of the box between the transformations for the repeatability study.	139
Table 6-10: ANOVA results for the XYZ coordinates of the box for the three registration categories.	140
Table 7-1: Information of the subjects with normal knees and knees with OA.	146
Table 7-2: Tibial surface registration results and medial tibial cartilage volume changes for the nine healthy subjects.	150
Table 7-3: Tibial surface registration results and medial tibial cartilage volume changes for the OA patients.	151
Table 7-4: The effects of digitization techniques on the registration and cartilage volume changes for normal and OA subjects.	152
Table 7-5: Transformation parameters and relative patellar movements from 15° to 30° knee flexion.	160
Table 7-6: Transformation parameters and relative patellar movements from 30° to 45° knee flexion.	161
Table 7-7: Movements of contact area centroids from 15° to 30° flexions and from 30° to 45° flexions for four female subjects.	165

List of Figures

Figure 1-1: Anatomy of the knee (The University of Chicago Hospitals, 2005).	2
Figure 1-2: Knee with signs of osteoarthritis (Zimmer, Inc., 2006).	3
Figure 2-1: Joint space narrowing observed from radiograph of OA knee (Felson et al., 1997)	9
Figure 2-2: 3-telsa General Electric MR unit at the Seaman Family MR Research Centre, Calgary (a) and MR image slices (b)	12
Figure 2-3: Trajectory of the tip of the magnetization vector (arrow) showing the return to the longitudinal direction or Z axis (T1 relaxation) and the decay of the transverse components in the X and Y directions (T2 relaxation) (Haacke et al., 1999).	14
Figure 2-4: MR knee image acquired with the 3D SPGR sequence (a) and with the T2-weighted FSE sequence (b) (Disler et al., 2000).	18
Figure 2-5: MR knee image acquired with a balanced SSFP sequence (an image from a dataset used in this thesis research).	19
Figure 2-6: Sagittal, coronal, and axial planes (San Diego Center for Spinal Disorders, 2006)	19
Figure 3-1: Registration primitives for the proposed surface matching algorithm: points for S_1 (a) and triangular patches for S_2 (b).....	51
Figure 3-2: Coplanarity condition describes the correspondence between a point in S_1 and a patch in S_2 after performing 3D similarity transformation.	54
Figure 3-3: Relationship between the seven transformation parameters and the orientation/geometry of the surface patches (Habib et al., 2001).	56
Figure 3-4: An accumulator array with the peak indicating the most probable solution for the parameter in question.	59
Figure 3-5: An accumulator array with a large cell size can result in all solutions contributing to one distinct peak (a), while a cell size that is too small will have no distinct peak to indicate the best solution (b).....	61
Figure 3-6: Methodology of the proposed surface matching algorithm.	64

Figure 4-1: MR image of a knee joint acquired by a proton density fast spin echo sequence (a). A zoomed-in portion of the image shows the presence of noise (b)..	68
Figure 4-2: Rough convergence for the angle φ based on the MIHT approach with the ending iterations showing oscillations between different solutions	68
Figure 4-3: Matching criterion (i): shortest normal distance (a) and matching criterion (ii): projected point is inside the patch (b and c).	71
Figure 4-4: Surface matching algorithm with the combined MIHT/ICP approach.	73
Figure 4-5: Convergence for the angle φ using only the MIHT approach (250 iterations) (a) and using the combined MIHT/ICP approach (10 MIHT with 40 ICP iterations) (b).	74
Figure 4-6: Overlapping LIDAR range images over an urban area: first (a) and second surfaces (b).	77
Figure 4-7: Sections of the first LIDAR surface represented by 44,156 points (a) and of the second surface modeled by 45,520 triangular patches (b).	77
Figure 4-8: Matched (blue) and unmatched-points (red) of the first surface (S_1) displayed on an ortho-photo of the target area (a), with the unmatched-points located mainly along edges of the buildings and vegetated areas (b).	80
Figure 4-9: Two Canon digital cameras mounted on a rigid frame for capturing stereo-images of the face.	84
Figure 4-10: Left and right stereo-images of a subject's face, with projected grid points to allow identification of conjugate features.	84
Figure 4-11: Surface model of a human's face generated by the TPS algorithm.	84
Figure 4-12: Facial images used in the three experiments (two time points (a), non-smiling versus smiling (b), and two different subjects (c)).	86
Figure 4-13: Co-registered face models of subject 1 with the green mesh representing the model from the first time point and the points (blue: matches, red: non-matches) representing the second time point.	87
Figure 4-14: Co-registered face models of subject 1 with the green mesh representing the non-smiling face and the blue (matched) and red (unmatched) points representing the smiling face (a); unmatched points projected onto the original image (b).	88

Figure 4-15: Co-registered face models of two different subjects with clear indications of different facial features by the non-matches (red points).	89
Figure 4-16: Two views of a rubber cat object acquired by a close-range laser scanner. 91	
Figure 4-17: Co-registered laser scanning views with the proposed surface matching algorithm (a) and with the Spin-Image technique (b) (green mesh represents the reference scan, blue points are the matches and red points are the non-matches for the second scan).	92
Figure 5-1: Subject imaged with the 3-telsa MRI unit and a flex coil at the Seaman Family MR Research Centre, Calgary.	96
Figure 5-2: Subject positioned at 0° knee flexion (full extension) (a) and 30° knee flexion (b).	96
Figure 5-3: MR images (sagittal balanced SSFP sequence) of a healthy knee at full extension (a) and with the knee at 30° flexion under loading condition (b). The red lines were the manually digitized points for the femoral bone-cartilage interfaces. 96	
Figure 5-4: Contours of the femoral condyle surface formed by digitized points of the MR image slice.	98
Figure 5-5: Digitized bone (red for patella, purple for femur) and cartilage (green for patella, blue for femur) surfaces of the articulating area of the patellofemoral joint (Connolly, 2005).	98
Figure 5-6: Femoral (a) and patellar surface (b) resampled and modeled by TPS (figures are not to scale), and a section of the triangular patches formed by Delaunay triangulation using the resampled points (c).	99
Figure 5-7: Coordinate system for the femur (X: Posterior (+) – Anterior (-), Y: Medial (+) – Lateral (-), Z: Proximal (+) – distal (-)) (a) and for the patella (X: Proximal (+) –Distal (-), Y: Medial (+) – Lateral (-), Z: Posterior (+) – Anterior (-)) (b).	105
Figure 5-8: Patellar (a) and femoral condyle (b) surfaces (Gray's Anatomy of the Human Body, 2006).	107
Figure 5-9: Registered femoral surfaces (30° with 0°) (a) and patellar surfaces (30° with 15°) (b) for subject 2, with the green mesh representing the reference surface, and blue points representing the matches and red points the non-matches from the transformed surface (figures are not to scale).	108

Figure 5-10: Mosaics showing a good match of the femur between the reference image (background: 0°) and its corresponding image from the second dataset (foreground/small windows: 30°).....	109
Figure 5-11: Mosaics showing a good match of the femur but different positions for the tibia and the patella due to the different knee flexion angles (background: 0° and foreground 30°).....	110
Figure 6-1: Spherical markers (ping-pong balls) being measured with the FaroArm. ...	120
Figure 6-2: Six linear markers mounted on wooden frame (white: 5 mm diameter; black: 3 mm diameter) (a) with end points measured by the FaroArm (b).	121
Figure 6-3: MR images of the spherical (a) and linear markers (b) for the pilot study..	122
Figure 6-4: Digitized edges (green points) of the spherical (a) and linear markers (b) with NMS (figures are not to scale).....	123
Figure 6-5: MR image of spherical markers filled with different materials.	125
Figure 6-6: Validation frame (a) constructed with wood and plastic (Robu, 2006), and the porcine knee specimen was fixed using construction cement (b).....	127
Figure 6-7: Six spherical markers were rigidly attached to the frame with three markers on each side of the joint (a, b).....	127
Figure 6-8: MR image of the porcine knee specimen (a) and the spherical markers (b) (figures are not to scale).....	129
Figure 6-9: Registered femoral surfaces of the porcine specimen with the green mesh representing the reference surface, blue points representing the matches, and red points representing the non-matches.....	130
Figure 6-10: 3D coordinates of a box were transformed using parameters from surface matching (SM) and absolute orientation (AO), and the resulting locations were compared.....	134
Figure 6-11: Ten surfaces generated from different digitization with arrows indicating each set of registration (red: category 1: 0° with 0°, green: category 2: 30° with 30°; blue: category 3: 30° with 0°).....	137
Figure 6-12: The 3D coordinates of a box were transformed with each set of transformation parameters and the resulting locations were compared.....	138

Figure 7-1: Image of a healthy knee at full extension acquired by a 1.5T MRI unit with a T1-weighted 3D spoiled gradient-echo fat-saturated sequence.	145
Figure 7-2: Digitized tibial intercondylar eminence (green line) manually by SliceOmatic (a) and with semi-automatic digitization using Canny edge detection (b).	147
Figure 7-3: ROI selected to enclose tibial cartilage (a); image enhancement applied to increase cartilage contrast (b); automatic thresholding selected cartilage voxels within the ROI (c).	149
Figure 7-4: Patellar surfaces at 30° and 45° transformed to the reference frame of 15° femur, using transformation parameters (TF) derived from surface registration, which related the 45° and 30° femurs to the 15° femur (a). The patellar surface at 15° was registered to the transformed patellar surface at 30°, and the one at 30° was registered to the one at 45° (b). The resulting parameters (TP) were used to quantify the patellar movement with respect to the 15° femur (b).	156
Figure 7-5: Patellar surfaces at different flexion angles with respect to the reference frame of the femoral surface at 15° flexion (3D view (a), 2D front view(b)) (units are in millimeters).	157
Figure 7-6: Patellar tracking system adapted from van Kampen and Huiskes (1990). ..	157
Figure 7-7: Mosaic shows a good match of the femur between the reference image (background, 15° flexion) and its corresponding image from the transformed dataset (foreground/small window, 30° flexion).	158
Figure 7-8: Detectable patellar translations and rotations based on the RMS distance from the registration.	159
Figure 7-9: Cartilage contact areas (color maps) on the patellar surfaces at 15°, 30°, and 45° flexion after registering to the same reference frames for subject 2 (units are in millimeters).	164

List of Abbreviations

2D	Two Dimensional
3D	Three Dimensional
ACL	Anterior Cruciate Ligament
ANOVA	Analysis of Variance
CoV	Coefficient of Variation
CT	Computer Tomography
FOV	Field of View
FSE	Fast Spin Echo
GA	Genetic Algorithm
GPS	Global Positioning System
ICP	Iterative Closest Point
INS	Inertial Navigation System
LIDAR	Light Detection and Ranging
MIHT	Modified Iterated Hough Transform
MR	Magnetic Resonance
MRI	Magnetic Resonance Imaging
NEX	Number of Excitation
NMR	Nuclear Magnetic Resonance
NMS	Non-Maxima Suppression
OA	Osteoarthritis
PFPS	Patellofemoral Pain Syndrome
RF	Radiofrequency
RMS	Root Mean Square
RMSE	Root Mean Square Error
ROI	Region of Interest
RSA	Roentgen Stereo-photogrammetry Analysis
SA	Specific Aim
SD	Standard Deviation
SNR	Signal to Noise Ratio
SPGR	Spoiled Gradient
SSFP	Steady State Free Precession
TE	Echo Time
TPS	Thin Plate Spline
TR	Repetition Time

Chapter One: Introduction

1.1 Background

The knee joint is the largest and most complex joint in our body, and it provides bearing of tremendous loads, stability, and mobility for a wide range of locomotive activities. The tibiofemoral joint (tibia and femur) and the patellofemoral joint (patella and femur) are the main articulations within the joint capsule. These articulations are surrounded by tissues like meniscus, cartilage, ligaments, and muscles that serve to distribute the load of the joint, enhance the stability, and control the movements of the knee (Figure 1-1). Due to its complex functions and high load environment, the knee is prone to many injuries and disorders, such as anterior cruciate ligament tears, meniscus tears, and patellofemoral pain syndrome (Hall, 2003).

Degenerative joint diseases, such as osteoarthritis (OA) that is marked by the deterioration of cartilage (Figure 1-2), also affects a large population (1/10 Canadians) and is a large burden to the health care system (The Arthritis Society, 2006). Although the exact etiology of OA is not well understood, there is evidence suggesting that genetic factors, biomechanical aggravations, and joint injuries play a role in the development of OA (Andriacchi et al., 2004, Eckstein et al., 2001, Felson et al., 2000, Holderbaum et al.,

1999). A recent review reports that a large percentage of young adults with traumatic joint injuries such as anterior cruciate ligament and meniscus tears will develop OA (Roos, 2005). These injuries often lead to instability, joint malalignment, increased load-bearing, and abnormal knee kinematics, which all are common risk factors that are associated with the development of OA. Therefore, to increase the understanding of the etiology and pathology of OA, in-vivo (i.e., inside the living body) quantitative assessments of morphological and mechanical properties of cartilage, joint kinematics, and joint health status (e.g., the disease stage of OA) are needed. The insights gained with these quantitative assessments can in turn lead to better diagnosis, evaluation, and treatments in patients.

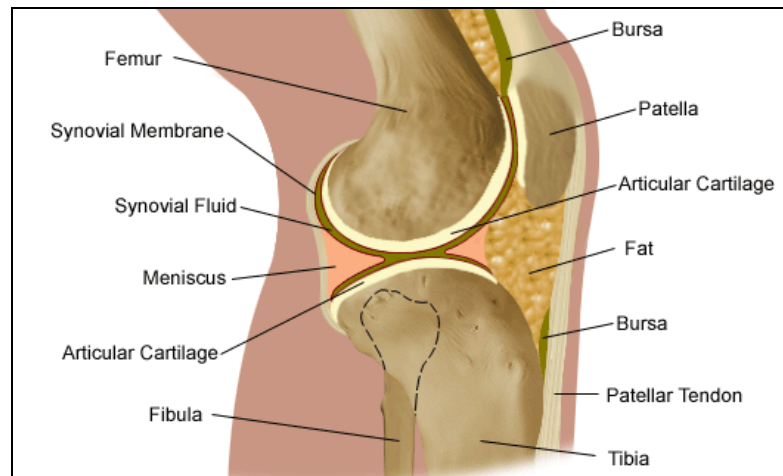


Figure 1-1: Anatomy of the knee (The University of Chicago Hospitals, 2005).

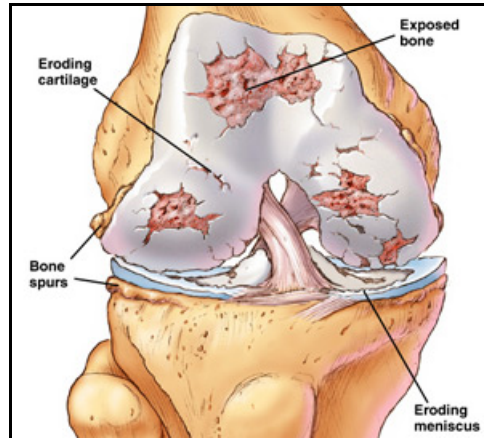


Figure 1-2: Knee with signs of osteoarthritis (Zimmer, Inc., 2006).

Medical imaging modalities, such as radiography (X-ray), computer tomography (CT), and magnetic resonance imaging (MRI) have been utilized for the diagnosis of musculoskeletal injuries and diseases, as well as for biomechanics studies and analysis. MRI is the preferred modality due to its capability in providing multi-planar cross-sectional images with superior soft tissue contrast and high spatial resolution, and has minimal risk to patients (Disler et al., 2000, Eckstein et al., 2001). MRI can capture accurate and high-density 3D data of joint structures for quantitative evaluation of mechanical and morphological properties of cartilage, joint kinematics, and joint health status, which can advance the understanding of OA.

Practically, it is difficult (and unlikely) that subjects can be positioned in precisely the same location between scans with MR imaging. Thus, it is typically impossible to capture the same cross-sections at identical anatomic locations and orientations. Moreover, injuries and disease progression can lead to local morphological changes.

Thus for MRI applications where the identifications and analysis of anatomically corresponding features are needed, registration is a necessary procedure for aligning two or more datasets together for direct comparisons.

Similar to medical imaging, 3D data or surfaces also play an important role in the field of Geomatics engineering for photogrammetric and remote sensing applications such as change detection, city modeling, and ice sheet monitoring (Habib et al., 2001, Habib et al., 2004, Wehr and Lohr, 1999). These geographic data are commonly acquired by ground-based, air-borne, and/or space-borne sensors, and can be multi-resolution and multi-temporal. These data are usually described by randomly distributed points that are measured with respect to different reference frames and have unknown correspondences. Thus registration is a necessary procedure for applications that require manipulation and comparison of these data.

This thesis research introduces a novel idea of translating registration techniques originally developed in the field of Geomatics engineering for biomedical applications. The proposed registration algorithm, originally developed by Habib et al. (2001), is a robust surface matching algorithm that allows simultaneous establishment of correspondences and determination of transformation parameters between two sets of data. With the increasing use of imaging in medical applications, research relating to medical image registration is a growing discipline that can benefit from ideas and knowledge in other fields.

1.2 Objective and Specific Aims

The main objective of this research is to translate and modify the proposed surface matching algorithm originally developed in Geomatics engineering to create novel approaches that will enable accurate registration of 3D MR data of joint structures, for the purpose of quantitative assessment of joint properties and diseases. This research focuses on the modifications of the algorithm, validation of the registration accuracy for MR data, and evaluation of repeatability. Experimentations with MR images of the knee joint were performed and the algorithm was employed in different applications to aid in disease monitoring and biomechanics studies. The objective of this thesis research is achieved through four specific aims (SA):

SA1) Investigate whether the algorithm can work with high density data in the presence of noise, implement necessary modifications, and perform verifications using Geomatics engineering applications.

SA2) Apply the modified surface matching algorithm to register 3D MR data of knee joint structures acquired at different positions and under different alignment and loading conditions.

SA3) Validate the registration accuracy obtained with the algorithm, and analyze the repeatability of the digitization and registration algorithm for matching knee joint surfaces generated from MR data.

SA4) Apply the modified surface matching algorithm to register 3D MR data of healthy and pathologic knees to aid in the in-vivo study of joint biomechanics and joint health status.

1.3 Thesis Outline

The thesis is organized into eight chapters. Chapter two summarizes literature review on studies of joint properties and diseases with MRI and presents some fundamentals of MR imaging. It also includes detailed reviews of published registration techniques in the field of medical imaging and Geomatics engineering, their experimental results, and the strengths and limitations of these methods. Chapter three provides detailed descriptions of the methodology of the proposed surface matching algorithm. The next four chapters represent the research to complete each of the study specific aims. Chapter four (SA1) describes the limitation of the algorithm when working with high density data and modifications required to overcome this issue. This chapter also includes verifications of the modified algorithm with three Geomatics engineering applications. The next chapter discusses the datasets, data processing steps (i.e., segmentation and surface modeling), and experimental results of the registration of knee joint surfaces generated from 3D MR data using the modified algorithm (SA2). Chapter six includes in-depth explanations of the experiments and results for accuracy validation and repeatability studies for the modified surface matching algorithm for registering MR data (SA3). Chapter seven

shows the data, procedures, and results for three applications of in-vivo studies of joint biomechanics and disease conditions using the modified algorithm, including: 1) monitoring changes in cartilage thickness for healthy and OA patients, 2) patellar tracking for healthy subjects, and 3) quantifying changes in contact locations of the patellar cartilage during knee flexions (SA4). Finally, the last chapter offers conclusions on the thesis research project and recommendations for future directions.

Some of the works described in this thesis have been presented in conferences and accepted for publication in peer-reviewed journals. The modified surface matching algorithm and preliminary experimental results with MRI and Light Detection and Ranging (LIDAR) data were presented at the International Geoscience and Remote Sensing Symposium, Seoul, Korea, July 2005, and at the Workshop Italy – Canada 2005 “3D Digital Imaging and Modeling: Applications of Heritage, Industry, Medicine, and Land”, Padua, Italy, May 2005. This work will also be published in the Electronics and Telecommunications Research Institute Journal, Volume 28 (Number 2), April 2006. The methodology and experimental results for the first MRI application in SA3, the monitoring of cartilage thickness changes, were presented at the 52nd Annual Meeting of the Orthopaedic Research Society, Chicago, USA, March 2006. This work is also accepted to be published in the journal Osteoarthritis and Cartilage. The second and third applications of SA4 were presented at the International Society for Optical Engineering Medical Imaging Conference, San Diego, USA, February 2006.

Chapter Two: Literature Review

2.1 Introduction

This chapter first presents background information on traditional technologies for assessments of joint diseases and biomechanics studies. Then, more recent studies using magnetic resonance imaging will be introduced along with a brief summary of magnetic resonance principles and imaging considerations for knee joint structures. The need of registration will then be emphasized, followed by critical review of existing registration techniques in both medical imaging and Geomatics engineering fields. Based on this literature review, this chapter ends with concluding remarks to rationalize the motivations and objectives of this research.

2.2 Imaging Applications in Assessment of Joint Injuries and Diseases

Many imaging techniques are available both clinically and in research for assessments of joint conditions and health status. Conventional radiography (X-ray) is widely used for diagnosis of osteoarthritis (OA) by the evaluation of joint space narrowing (narrowing of joint space due to thinning of cartilage) (Figure 2-1), and evaluation of pathological lesions such as osteophytes and bone sclerosis (Altman et al., 1996, Felson et al., 1997, Vignon et al., 1999). Due to its high variability and low sensitivity, many studies

attempted to standardize the clinical protocol and measurement techniques so that radiographic diagnosis could be more accurate, reproducible, and reliable (Altman et al., 1987, Altman et al., 1996, Vignon et al., 1999). Despite these standardized protocols, radiographs only permit an indirect evaluation of cartilage degeneration based on a 2D measurement. Additionally, planar radiography does not display any information about soft tissues like cartilage, ligaments, and meniscus. Studies have also revealed no correlation between radiographic and clinical changes for 500 subjects with knee OA (Dieppe et al., 1997), and no correlation between longitudinal changes in cartilage volume and joint space width (Cicuttini et al., 2005). Arthroscopy is another gold standard tool for diagnosis and surgical instrumentation for joint injuries and OA, which can provide magnified and direct viewing of soft tissue conditions (Oakley and Lassere, 2003, Oakley et al., 2005). However, only surface details are captured with little information for the morphological properties of the soft tissues. Its invasive manner also makes it unfavorable, especially for research.



Figure 2-1: Joint space narrowing observed from radiograph of OA knee (Felson et al., 1997)

For kinematics studies, numerous groups have reported results on patellar tracking (i.e., track the movement of the patella with respect to the femur) to understand normal and pathological biomechanics of the patellofemoral joint. Early studies, which mainly based on cadaveric measurements, employed roentgen stereo-photogrammetry analysis (RSA) and X-ray photogrammetric techniques (van Kampen and Huiskes, 1990, Veress et al., 1979). These techniques utilized traditional photogrammetric principles to measure 3D movement of bone-implanted markers during knee flexions. Hefzy et al. (1992) measured the motions of cadaveric joints using the 3-SPACE digitizer and tracking system, which utilized low-frequency magnetic field technology to provide measurements with six degrees of freedom. Koh et al. (1992) tracked the in-vivo patellar motions with bone-implanted markers in the patella, femur, and tibia for one male subject, using video and motion analysis systems for seated and squatting knee flexion/extension exercises. These in-vivo results were in general agreement with cadaveric measurements (van Kampen and Huiskes, 1990). Ahmed et al. (1983) measured contact area and pressure distribution of patellofemoral cartilage in-vitro using transducers attached to 24 amputated limbs. Their results indicated that the contact area increased from 0° to 60° flexion, remained constant between 60° to 90°, and decreased from 90° to 120° flexion. A more recent study measured patellar tilt, patellar displacement, and anatomic shapes of the joint based on 2D radiographs (lateral and axial views at 35° flexion) to determine whether alignment abnormalities were found in subjects with patellofemoral pain syndrome (PFPS) (Laprade and Culham, 2003). These experiments with 33 PFPS

subjects matched with 33 controls found no significant differences in patellar tilt and displacement between the two groups for loaded and un-loaded conditions. Stereophotogrammetry was also employed for accurate in-vitro measurements of cartilage topography and thickness maps of articular surfaces (Ateshian et al., 1991).

Although these pioneering studies developed accurate techniques and reported important findings on joint structures and kinematics, in-vitro measurements on cadavers likely do not reflect the true in-vivo environment and kinematics of viable joints, and the use of invasive bone markers might alter normal kinematics. Furthermore, 2D measurements on radiographs cannot capture and represent 3D characteristics of the joint. With recent advancements in magnetic resonance imaging (MRI) technologies, non-invasive in-vivo evaluation of joint properties and disease conditions became possible. Unlike X-ray and CT that are based on ionizing radiation, MRI has no known risks to subjects, thus is widely accepted for clinical and research applications.

2.3 Magnetic Resonance Imaging

MRI (Figure 2-2a) is capable of providing multi-planar cross-sectional images of high resolution and soft-tissue contrast (Nishimura, 1996) (Figure 2-2b). It is highly flexible for controlling the image content and quality, and can provide both anatomic and metabolic information. This section includes background information about MR principles and imaging considerations. As the focus of this research is on registration,

only a brief summary of MR principles is provided here. Emphasis is placed on why MRI is used for quantitative assessment, rather than how MRI works to provide quantitative information. More detailed information about MR fundamentals is provided in Nishimura (1996) and Haacke et al. (1999). MR imaging considerations for the knee joint will be presented, as they influence the registration process and the achieved accuracy. This section also includes a review of the accuracy of MRI to measure joint properties and studies that used MRI for evaluation of joint diseases and kinematics.

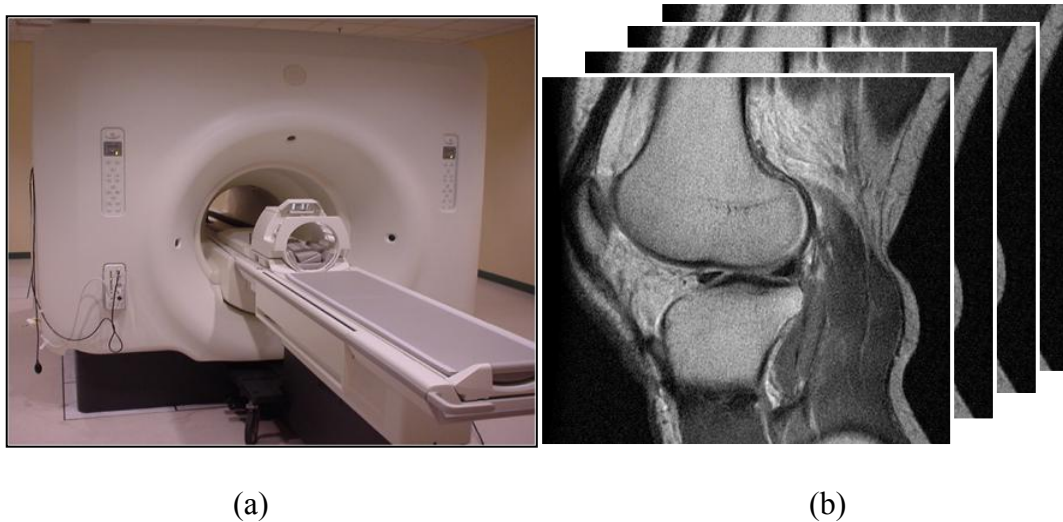


Figure 2-2: 3-telsa General Electric MR unit at the Seaman Family MR Research Centre, Calgary (a) and MR image slices (b)

2.3.1 Principles of Magnetic Resonance

MRI, a tomographic medical imaging technique that is based on the phenomenon of nuclear magnetic resonance (NMR), was first proposed by Edward Purcell and Felix Bloch in 1946. In 1973, Paul Lauterbur showed the first MR image obtained based on this principle. The quantum mechanics of NMR describes the nuclear spin angular

momentum of atoms. For MR, the hydrogen proton (^1H) is the nucleus of interest, as it is most abundant in the human body and gives the largest MR signal.

Three types of magnetic fields influence the nuclear spins of the hydrogen protons to produce MR signals: 1) main magnetic field, 2) radiofrequency (RF) field, and 3) linear gradient field. With the presence of the main magnetic field, the magnetic moment vectors (originally in random orientation) tend to align in the direction of this main field (longitudinal direction), which gives a net moment in the equilibrium state. The nuclear spins also precess at a resonance frequency called the Larmor frequency. To generate MR signal pulses, radiofrequency tuned to the resonant frequency of the spins is applied in the transverse plane, exciting the spins out of the equilibrium state. This excitation causes the net magnetization vector of the spins to flip (e.g., by 90°) and lie on the transverse plane. Once the RF excitation is turned off, the spins relax back to their equilibrium state and give off an electromotive force. This electromotive force is received by an RF receiver coil and recorded as the MR signal. The relaxation process is characterized by two time constants, known as T1 and T2 relaxation times (Figure 2-3). T1 describes the time required for the magnetization vector to return to the longitudinal direction (Z axis) while T2 describes the decay of the vector component in the transverse direction (X and Y axes). Different tissues in the human body have different T1 and T2 values. Additionally, abnormal tissues also show altered values compared to normal tissues. These relaxation values, along with different atomic densities, provide different MR signals (i.e., contrast) for different tissues.

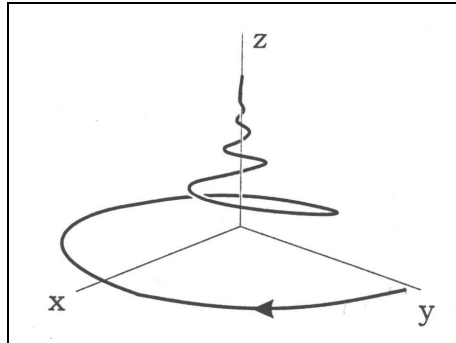


Figure 2-3: Trajectory of the tip of the magnetization vector (arrow) showing the return to the longitudinal direction or Z axis (T1 relaxation) and the decay of the transverse components in the X and Y directions (T2 relaxation) (Haacke et al., 1999).

To determine the spatial locations of the received signal, linear gradient magnetic fields are used in three directions (slice selection, frequency-encoding, and phase-encoding directions) to give varying field strength with respect to location. This enables the signal to be spatially encoded to produce a proper image. After processing, the received signals are stored in a matrix form known as the k-space (spatial-frequency space). Each point in this k-space contains information for all parts of the image. Fourier transform is subsequently performed to form a pixel image with grey scale intensities.

2.3.2 MR Imaging Parameters

For MR imaging, several parameters must be considered that can affect the image resolution, tissue contrast, scan time, and signal to noise ratio (SNR) of the images. These parameters provide the flexibility of MR imaging to produce image content that is

best suited for different applications, with different parameter combinations resulting in different imaging sequences.

The flip angle describes the amount of rotation (angle of excitation) of the magnetization vector, and is proportional to the RF power. Flip angle affects the amount of scan time and also the intensity of the signal. The repetition time (TR) describes the time between consecutive RF pulses, and the gradient echo time (TE) describes the time between the RF pulse and the echo (signal measurement). TR and TE are important parameters for adjusting image contrast. Scan time is influenced proportionally by the TR parameter, while the TE parameter has no effect. Number of excitation (NEX) is the number of signal measurements, or in practical terms, the number of averages of the signals. Thus, increasing NEX can increase SNR, but can also increase the scan time. The receiver bandwidth is the rate at which the signal is sampled, and it directly affects the SNR. A larger bandwidth will decrease the SNR, but can improve spatial resolution (faster sampling). The acquisition matrix contains the number of data samples acquired in the frequency and phase encoding direction, with a larger matrix giving higher resolution but also requiring longer scan time. Field of view (FOV) is defined as the size of the spatial encoding area and can also be defined as the sampling rate in k-space. The FOV should be large enough (i.e., sufficient sampling rate) to encompass the object of interest to avoid aliasing (wrap around of the object). To summarize, the relationships between SNR and the imaging parameters can be explained by the following equation:

$$SNR \propto \frac{(\Delta x \times \Delta y \times \Delta z) \times \sqrt{N_x \times N_y \times N_z \times NEX}}{\sqrt{bandwidth}} \quad (2-1)$$

Where: $\Delta x, \Delta y, \Delta z$ are the resolution of the voxel in the x, y, and z directions, and
 N_x, N_y, N_z are the number of samples/measurements collected.

Clearly all the imaging parameters are interrelated; indicating that a tradeoff between parameters may be required to obtain the optimal image. For example, increasing matrix size or decreasing FOV increases spatial resolution, but at the expense of either decreased SNR or increased scan time. To improve SNR, a higher NEX can be used, but this also increases the scan time. Therefore, for each application, it is important to define the required resolution and tissue contrast, and the acceptable scan times, in order for the best imaging sequence (i.e., combination of parameters) to be chosen to produce the most suitable images. It is also important to keep in mind that image quality is constrained by machine and hardware limitations.

2.3.3 MR Imaging Considerations of the Knee

Quantitative assessments of the complex composition of the knee joint structures and properties based on MRI require the tissues of interest to be delineated clearly and accurately from their surrounding tissues. For example, for the monitoring of OA and kinematics studies such as patellar tracking, the underlying bone surface, the bone-cartilage interface, and the cartilage surface should all be clearly presented in the MR images. Achieving high spatial resolution is also important as knee structures such as

cartilage is extremely thin, on the order of 0.1 mm to 7 mm, depending on the joint and species (Disler et al., 2000). Therefore, MR imaging sequences employed to acquire the images must maximize tissue contrast and spatial resolution while maintaining a sufficient SNR and an imaging time that is acceptable for the application (Hardy et al., 2000).

A T1-weighted 3D spoiled gradient-echo (SPGR) imaging sequence with fat-suppression is commonly employed for quantitative assessments of cartilage, as it allows detection of cartilage defects with high sensitivity and specificity. Cartilage appears bright with this sequence when compared to surrounding tissues (e.g., bone appears darker), and chemical shift artifacts are minimized (Figure 2-4a) (Disler et al., 2000, Eckstein et al., 2001, Suh et al., 2001). Although this sequence can provide sufficient SNR and resolution, one limitation is that it produces little contrast between cartilage and synovial fluid (Hargreaves et al., 2003). A fat-suppressed intermediate- or T2-weighted fast spin echo (FSE) sequence is also commonly used for imaging cartilage of the knee, as it is also highly sensitive to cartilage defects (Figure 2-4b) (Disler et al., 2000, Suh et al., 2001). Cartilage appears as an intermediate signal for this imaging sequence, with fluid brighter and bone darker. Due to the better contrast between cartilage and fluid, FSE can typically reveal cartilage lesions more clearly than the 3D SPGR sequence. More information about gradient echo, spin echo, and image sequences can be found in Nishimura (1996) and Haacke et al. (1999).

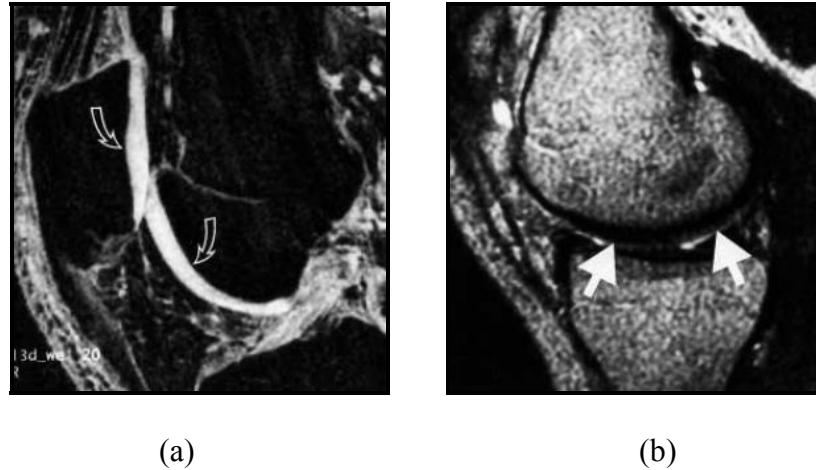


Figure 2-4: MR knee image acquired with the 3D SPGR sequence (a) and with the T2-weighted FSE sequence (b) (Disler et al., 2000).

Recently, with the technological advancement in MR hardware and sequences, a balanced steady state free precession (SSFP) sequence has become more popular as it can provide fast imaging with strong contrast between tissues and high SNR (Scheffler and Lehnhardt, 2003). For knee imaging, balanced SSFP sequences have shown to increase contrast between cartilage and synovial fluid (Figure 2-5), improve SNR, and minimize scan times relative to the 3D SPGR and FSE sequences (Hargreaves et al., 2003). The TR has to be kept short as these methods are very sensitive to magnetic field variations and susceptibility variations, which can lead to banding artifacts in the acquired images. In fact, a shorter TR can increase SNR efficiency (SNR normalized by the square-root of scan time) for the balanced SSFP sequences.



Figure 2-5: MR knee image acquired with a balanced SSFP sequence (an image from a dataset used in this thesis research).

The imaging orientations/planes are also important to showcase the tissues of interest. Medial and lateral compartments of articular cartilage surfaces are best captured by images in the coronal and sagittal planes (Figure 2-6). The geometry of the patellofemoral joint (e.g., patellar surface, contact between patella and femur) can be best seen on axial and sagittal images. Sagittal views can also be used for patellar tracking (Stoller, 1997).

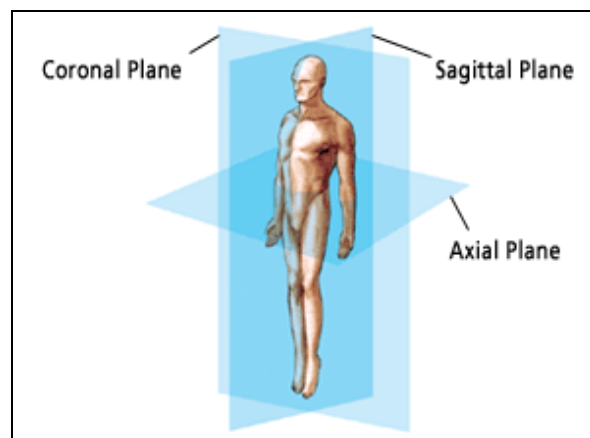


Figure 2-6: Sagittal, coronal, and axial planes (San Diego Center for Spinal Disorders, 2006)

MR imaging artifacts can cause errors and mis-interpretations in knee measurements, which in turn can lead to errors in the registration. Artifacts can be caused by hardware defects, specific biochemical environments of the object of interest, and may also be dependent on the type of imaging sequences used. Susceptibility artifact is caused by variations in the magnetic field strength that occur near the interfaces of substances of different magnetic susceptibility (Ruan, 2003), such as the interface of water and air. The effects of this artifact are bright and dark areas (banding) with spatial distortions in the surrounding shapes, and are commonly found with gradient-echo sequences. Lower field strength, higher resolution, and shorter TR are some ways to minimize the effects of this artifact (Ruan, 2003, Hargreaves et al., 2003). Chemical shift artifact causes mis-localization of water and fat pixels in the images due to differences in their resonance frequencies (Lamour frequencies) (Disler et al., 2000). Since protons with different precession frequencies are expected to result from different locations (e.g., the effect of the gradient fields), spins from fat and water molecules in the same imaging voxel (same physical location) can therefore be encoded into different voxels. This artifact can be apparent at the knee cartilage and fat interfaces. Chemical shift artifact can be eliminated using fat-suppression for the imaging sequences (Disler et al., 2000), by imaging at lower magnetic field strength, or by decreasing voxel size (Ruan, 2003). Magic angle artifact is found in tissues with highly anisotropic arrangement of molecules, such as the collagen fibers in articular cartilage. When the long axes of the collagen fibers are oriented at 55° (the magic angle) to the main magnetic field, the cartilage appears brighter than other

tissues (Xia, 2000). This increase in signal can mimic cartilage defects, especially for T2-weighted imaging sequences, and can lead to false diagnoses. Re-imaging by changing the relative angles can usually help to detect and avoid this artifact, while a longer TE can also give a smaller increase in the signal intensity. Partial volume artifact describes the effect of signal averaging when a large image pixel encompasses more than one type of tissue. This artifact most typically occurs in the slice-direction, which usually has the largest voxel dimension (Ruan, 2003). This artifact can simulate abnormalities and can blur the affected tissue. Decreasing the voxel size and imaging in multiple image planes can help to detect and reduce this artifact. Although these artifacts can be minimized or compensated for, they cannot be fully avoided, thus can affect the accuracy of MR measurements of joint structures.

2.3.4 Accuracy of MR Measurements of Joint Properties

With increasing use of MR imaging in clinical examinations and research, studies were needed to analyze the accuracy, reproducibility, and reliability of MR measurements of joint properties. Cohen et al. (1999) validated knee cartilage thickness measurement based on manual segmentation using MR images of six cadaveric knees (fat-suppression spoiled gradient-recalled sequence, resolution: $0.47 \text{ mm} \times 0.47 \text{ mm} \times 1.0 \text{ mm}$) against ones obtained using stereophotogrammetry. An average deviation of 7% between the two methods was reported (RMS difference in the thickness between MRI and photogrammetry measurements). The authors also validated surface topography derived

from MRI and found root mean square (RMS) errors of 0.23 mm for the cartilage surface and 0.14 mm for the bone surface. Graichen et al. (2004) compared cartilage thickness measurements by MRI (T1-weighted 3D SPGR sequence, resolution: 0.31 mm × 0.31 mm × 1.5 mm) with morphological measurements obtained using an image analysis system on surgically removed cartilage. An absolute difference of 8.9% was found between the measurements from each technique, with higher errors for tibial cartilage than patellar cartilage. Stammberger et al. (1999) tested the in-vivo reproducibility of cartilage thickness with MRI, and found that the mean thickness was reproducible to 2.5% for the patella, 2.8% for the lateral tibia, and 3.4% for the medial tibia (RMS average of the individual coefficient of variation percent).

For cartilage volumes, Cicuttini et al. (1999) calculated the accuracy of MR measurement (T1-weighted fat saturation 3D gradient recall acquisition in the steady state, resolution: 0.31 mm × 0.31 mm × 1.5 mm) as an average absolute over/under estimation of volume, with volume measured by water displacement of surgically retrieved tissue as a reference. An average difference of 8.3% for the patella, 9.2% for the femur, and 9.2% for the tibia was reported. The intra-observer reproducibility was found to be 3% (coefficient of variation) for the patellar cartilage volume, 2% and 5% for the femoral and tibial volume respectively. Eckstein et al. (2002) investigated long term (up to eight months) and re-segmentation precisions for MR measurements (sagittal, FLASH-3D sequence, resolution: 0.31 mm × 0.31 mm × 1.5 mm). A long term RMS average coefficient of variation (CoV) of 1.4% for cartilage volume was reported for all knee surfaces, and

2.4% for mean thickness measurement. The re-segmentation precisions were found to be 2.6% and 2.5% respectively for volume and mean thickness.

These results indicate that MR measurements of joint structural properties have shown to be accurate, repeatable, and reliable. Thus, these results further confirm the efficacy of MR imaging in research and clinical fields for studying joint injuries and diseases.

2.3.5 Studies of Joint Biomechanics and Diseases with MRI

Many studies have adapted MRI for kinematics studies and disease monitoring. Cicuttini et al. (2004) compared longitudinal changes of femoral and tibial cartilage volumes for 117 patients with knee OA to investigate the correlation of the volume changes between these two surfaces. Subjects were imaged and followed up after a 2-years interval. Results revealed a cartilage loss of $150 \pm 300 \text{ mm}^3/\text{year}$ (mean \pm standard deviation) for the femur and $100 \pm 250 \text{ mm}^3/\text{year}$ for the tibia. A significant correlation was found for the changes of cartilage volume between the femur and the tibia. This correlation suggests that only tibial measurements, which were more reproducible than femoral measurements, may be sufficient for assessing OA. Wluka et al. (2004) determined whether joint cartilage in healthy postmenopausal women remained stable or changed over time. Female subjects (29 subjects with estrogen replacement therapy, and 28 non-users) were imaged with MRI at baseline and at 2.5 years later. An average annual reduction in medial and lateral tibial cartilage volume was recorded as 2.4% and 2.3%

respectively. Studies have also shown that MR-based analyses of OA are highly accurate, precise, and highly reliable for test–retest reliability, between-reader agreement, and patient positioning reliability (Burgkart et al., 2001, Graichen et al., 2004, Raynauld et al., 2003). Thus MRI is evidently an important tool for diagnosis, monitoring, and evaluation of treatment responses for joint diseases.

Knee joint biomechanics have been examined through assessing patellar tracking and joint contact patterns under loading conditions measured from images acquired by open or closed MR scanners (Cohen et al., 1999, Connolly, 2005, Moss, 2001, Patel et al., 2003, Scarvell et al., 2004, Tennant et al., 2001). Tennant et al. (2001) found that medial-lateral movements occurred for the patella at normal knee flexion, measured with an open MR scanner under normal weight-bearing conditions. Patel et al. (2003) also found medial translations and tilts for normal knee joints at early degrees of flexion under loading conditions with a closed MR configuration. This group also reported increases in the patellofemoral cartilage contact areas from 0° to 60° of flexion, and speculated that this minimized the higher contact pressure at increased flexion angles. These results agreed with cadaveric studies (Ahmeh et al., 1983).

To understand the effects of injuries on joint biomechanics, the contact patterns between normal and anterior cruciate ligament (ACL) deficient subjects were compared during knee flexion based on MR measurements (Ronsky, 1994). For the normal subjects, results agreed with various studies that the contact areas increased with increasing flexion

angle, and moved proximally relative to the patellar surface. For ACL deficient subjects, the contact did not show consistent increase in areas during flexion, and the proximal movements were smaller in magnitude. Connolly (2005) characterized patellar tracking in a recent study between ten healthy and ten PFPS subjects by comparing their patellofemoral contact areas and tracking patterns during knee flexion. Statistically significant differences were not found between the two groups from 30° to 45° knee flexions. In the early degrees of flexion, from 15° to 30°, the contact patterns were different between the groups. The normal subjects showed a significant increase in contact areas and proximal migration at these early degrees of flexion, but this consistent pattern was not observed in the PFPS subjects.

With all of these biomechanical studies based on quantifying medical image, the analyses rely heavily on digital image processing techniques, which include segmentation, 3D reconstruction, computation, and registration. By considering all of the potential sources of errors associated with the various image processing procedures, the registration has to be accurate enough to allow reliable detection of changes (e.g., cartilage thickness) with a magnitude of 1~2 mm in the case of disease monitoring, and be sufficient for tracking joint surface movements in the range of 1~2 mm for positions and 1~2° for orientations in biomechanics studies. The following sections provide reviews on surface modeling and registration techniques.

2.4 Surface Modeling

When working with 3D MR image datasets, analysis and manipulations of anatomical surfaces of interest have to be extracted and modeled from the image slices. The Thin Plate Spline (TPS) algorithm for surface modeling of a cloud of 3D points based on MATLAB (The Mathworks, Inc., Natick, MA, version 5.1), implemented and used within our research group (Boyd et al., 1999), is summarized here. More information can be found in Boyd et al. (1999).

The TPS algorithm models a surface by bending a thin plate of infinite dimensions, such that it passes through the original surface points, with the constraint that the bending energy is minimized. The algorithm is applicable for only small deflections of the thin plate. The TPS surface is described by the form $z = f(x, y)$. A radial basis function of $f(x, y) = r^2 \ln(r)$, where $r^2 = x^2 + y^2$, is used to interpolate between the data points. The bending energy of the function $f(x, y)$ has the form:

$$E(f) = \iint_{R^2} \left\{ \left[\frac{\partial^2 f}{\partial x^2} \right]^2 + 2 \left[\frac{\partial^2 f}{\partial x \partial y} \right]^2 + \left[\frac{\partial^2 f}{\partial y^2} \right]^2 \right\} dx dy \quad (2-2)$$

Where R^2 encompasses the x - y plane.

For a dataset that contains points with x_i , y_i , and z_i coordinates with $i = 1, \dots, n$, there is a unique surface function $z_i = f(x_i, y_i)$ where $E(f)$ is minimized. The bending energy

formulation (Equation 2-2) can be expressed in terms of the radial function ($f(x, y) = r^2 \ln(r)$). Descriptions of the derivatives can be found in Lancaster and Salkauskas (1986).

With a surface equation, new surface points with x , y and z coordinates can then be extracted. Thus, the TPS algorithm can model a scattered point cloud by allowing surface re-sampling at a regularly spaced grid with high resolution. For datasets that are noisy, such as MR data, surface smoothing may be needed. This smoothing can be accommodated by incorporating a weighting function with a least squares criterion:

$$J(f) = E(f) + \sum_{i=1}^n w_i [f(x_i, y_i) - z_i]^2 \quad (2-3)$$

Where w_i are weights that determine how close the values $f(x_i, y_i)$ will be to z_i .

The weight is defined by a user specified smoothing parameter (λ) and the standard deviation of the data (σ):

$$w_i = \frac{\lambda}{\sigma_i^2} \quad (2-4)$$

Therefore, for a specific smoothing parameter, a smaller weighting will be used for data that contains more noise (i.e., larger standard deviation). For a small weight or weighing close to zero, little attention is placed on the z_i of the data points, resulting in a highly smoothed surface. Conversely, larger weights will result in less smoothing. Therefore, the smoothing parameter as specified by the user can assist in determining the amount of smoothing of the final TPS surfaces. In addition to the re-sampling and smoothing

capabilities, TPS algorithm can also calculate and provide surface characteristics such as surface curvatures and normals at each resampled point. These measures can be further processed to quantify joint properties such as cartilage thickness, surface area, and joint contact patterns. The algorithm was tested by modeling a feline patellofemoral joint surface measured by multi-station digital photogrammetry (Ronsky et al., 1999). Surface curvatures and cartilage thickness were also calculated. One main limitation of TPS as implemented was identified. The algorithm, based on a 2D projection of the radial basis function, cannot work with data points that share the same XY coordinates but with different Z coordinates. In other words, it cannot model a surface that curves more than 180° (e.g., a sphere) over itself. Another issue is that the curvature fluctuations can occur at the data points, especially at the edges of the surface. Also, dataset with large number of points (more than 2000) can lead to numerical problems with solution convergence and a long run-time. However, experience has demonstrated that joint surfaces captured using medical imaging techniques can be adequately manipulated to minimize these problems (Baker, 2002, Moss, 2001, Connolly, 2005).

Overall, the TPS algorithm is a fast and simple way to model and resample joint surfaces that are represented by scattered 3D points in the presence of noise. It provides a numerical representation of the surface and surface characteristics for analysis. This algorithm will be employed to model joint surfaces acquired by MRI in this thesis research.

2.5 Registration Techniques

Since this research focuses on registration, this section presents in-depth literature reviews of existing techniques in both fields of medical imaging and Geomatics engineering.

Registration is a process to align two or more datasets of the same objects, areas, or features together, which are typically captured by different sensors, at different times, and/or from different viewpoints (Brown, 1992). Therefore, datasets may have different geometric and radiometric characteristics, may be measured with respect to different reference frames, and have unknown correspondences between them. Registration of these datasets thus allows for direct qualitative and quantitative comparisons, typically enabling better inferences and more information to be extracted from the results.

In general, registration for any application requires the definitions of the four issues of the registration paradigm: 1) registration primitives (e.g., points, lines, or surfaces) to represent the data of interest; 2) transformation function that mathematically aligns/maps the reference frame of one dataset onto another; 3) similarity measure that constrains the correspondence of conjugate primitives; and 4) the matching strategy that utilizes the above functions to automate and resolve for the best solution (Brown, 1992). The choices for these four issues depend on many factors, including the types of application and problem, the modalities involved, associated image distortions and noise, required accuracy, and available resources (Maintz and Viergever, 1998).

2.5.1 Medical Image Registration

Medical imaging is a very important tool for diagnosis, surgical planning, monitoring, and research activities. Different imaging modalities such as X-ray, CT, MRI, ultrasound, and nuclear medicines can provide different anatomical and functional information about the human body. Data acquired by different modalities are usually complementary in nature, thus accurate registration is crucial for many medical research and clinical applications. Accurate registration is also required for manipulation and analysis of data that are acquired at different times or under different conditions.

For MR imaging, the registration procedure is challenged by MR imaging artifacts and noise, changes in radiometric characteristics due to different scanner configuration, and anatomical changes resulting from disease progression. With these challenges in mind, research aims to develop registration approaches that are comparatively fast, semi to fully automated, accurate, and reliable for their intended applications (Maintz and Viergever, 1998). The remainder of this subsection provides reviews on some existing medical image registration techniques, as well as critiques of the validity of these techniques for in-vivo studies on joint conditions with MRI.

2.5.1.1 Elastic Registration based on Intensity Variations

Periaswamy and Farid (2003) developed an elastic registration algorithm that could be applied to both 2D and 3D medical images. This technique used intensity levels of pixels

as the primitive for registration, and the formulation was based on motion estimation. A local affine model (linear affine and translations parameters) was chosen as the transformation function to model motion between the source and target images. In addition, two parameters were added to capture the spatially-varied contrast and brightness. The parameters allowed a successful registration that accommodated local intensity variations. To avoid a degenerate solution where two images were mapped only based on intensity modulation, a global smoothness constraint was employed on the contrast and brightness parameters. An error function, which described the differences between the transformed source and target images, was minimized to ensure the correspondence of the primitives. Finally, a Gaussian pyramid (composed of local averages of the images at various scales, where each level contained down-sampled images of the preceding level) was used as a matching strategy where the algorithm is iterated through a coarse-to-fine scheme to warp the source image towards the target image. This elastic registration algorithm consisted of a geometric model that produced a locally affine but globally smooth transformation while the intensity model accounted for the contrast and brightness differences.

Synthetically transformed images were tested with the algorithm and demonstrated good registration results. Clinical images of different subjects or of subjects at different times were also registered using the proposed algorithm. Images acquired from different modalities showed good matches even when there were significant intensity differences between images. Since the results were only visually evaluated, it is difficult to assess

the accuracy of the algorithm without having a numerical measure to quantify the validity of the registration. Nonetheless, as a general assessment, the incorporation of the intensity variation parameters and smoothness constraint should increase the accuracy of the algorithm.

Using pixel intensities as a basis/primitive for registration might not be feasible for MR images of knee joint structures. The quality of the images is frequently altered by scanner configurations, MR imaging artifacts, and noise, which can lead to changes in the signal intensity of tissues such as cartilage (Disler et al., 2000, Suh et al., 2001). Another issue of an intensity based approach is the required computational effort as reported as one of the technique shortcomings.

2.5.1.2 Genetic Algorithm for 3D MR-CT Registration

Rouet et al. (2000) presented the usage of Genetic Algorithm (GA) as the matching strategy and optimization process for a robust 3D MR-CT registration through a three-step procedure: rigid registration, search space sampling, and local optimization. GA is an optimization procedure that resides on the concepts of natural selection and survival of the fittest. The chosen primitives were classified point sets based on curvature from both CT and MRI surfaces, and a Euclidean map of the MRI volume. A global rigid registration (step 1) was performed to provide a good initial approximation for the alignment of the surfaces. GA was used with real numbers in a bounded search space

and controlled selection to determine the six transformation parameters (three translations and three rotations). The images used in this study were MR and CT head scans. As it was suspected that rigid registration was not sufficient to model the MR distortions and soft tissue structure, a trilinear transformation was selected as the global elastic transformation function to perform warping. 24 parameters were estimated with a minimum requirement of eight corresponding pairs of points from both scans. GA was used on an indexed search space (step 2) to find eight pairs of points that would result in good elastic transformation. To reduce the size of the search space, only point pairs belonging to the same curvature class and having a median error distance (derived from step 1) less than a threshold were considered. Therefore, GA was used in this step to sample the search space for a reduced population of point pairs. The last step of the algorithm was to fine tune/optimize the solution by merging and/or removing point pairs selected from step 2 until the fitness between the surfaces was maximized.

To assess the quality of the registration, a visual analysis of the superposition of the bone and tissue structures and a direct multivolume rendering were performed. CT scan and MRI volume of the head were of different matrix sizes (CT: $256 \times 256 \times 91$; MRI: $256 \times 256 \times 68$) and artifacts were noticed on the CT images. The rigid registration step achieved a fitness of 74.9%. For the elastic point-matching step, point-pairs were generated based on the stated criterion. The inclusion of the curvature class resulted in a significant improvement in the computation time of the point-pairs generation. GA converged to 100 couples in the final population and gave a fitness of approximately 79%.

After fine tuning the solution, the fitness improved to about 80%. Visual assessments showed good alignment of the two surfaces. To validate the method, registrations were performed on the data of Vanderbilt Retrospective Registration Evaluation Project, which was designed to provide a database of CT and MR images and for comparison of different rigid registration techniques. The rigid registration step (step 1) gave average results when compared to the other techniques that participated in the Vanderbilt project (e.g., Hemler et al., 1995, Maintz et al., 1996).

This technique based on GA did not require the use of landmarks for aligning the surfaces, which could be advantageous for the knee joint with its lack of clear anatomical point landmarks. Despite the fact that GA produced good registration of MR-CT head images, it has its limitations. GA has the risk of premature convergence to local maxima but could be avoided by having good initial approximations and an adequate control of the search space. Also, GA requires a tuning of different parameters (e.g., stopping criteria, population size, and mutation and crossover parameters) which might lead to different results. Although the authors reported that changing the parameters could only influence the processing time, further validations on the sensitivity of GA are required for the registration of MR images of joint structures. Sanden and Ronsky (2003) looked at using GA to register patellar cartilage surfaces generated from MR image slices. However, the algorithm failed to perform due to the large number of sampled points. Decreasing the number of points could result in inaccurate representation of the cartilage surfaces. Also, because cartilage surfaces are generally of low curvature, the use of

curvature classes to reduce the search space might not be as effective as for other anatomical structures.

2.5.1.3 Elastic Registration for Detecting Cartilage Changes

Stammberger et al. (2000) developed a 3D elastic registration method for measuring local changes in patella cartilage thickness. They also validated the performance and reproducibility of their technique with artificial and in-vivo MR image data. The cartilage surfaces were first segmented with a B-spline snake segmentation algorithm. These contours were processed to form a 3D surface consisting of a network of triangles. Elastic registration was subsequently performed, using a two-stage approach. First, the surfaces of the bone-cartilage interfaces were aligned using a rigid registration. In this step, the primitives were the vertices of the network of triangles and the 3D similarity transformation (three translations and three rotations) was used to map the surfaces. The similarity measure was to align the principal axes with the use of eigenvalue decomposition of the geometric inertia matrices of both surfaces. Elastic registration was performed following the rigid matching step. In this process, the vertices of one surface and surface patches of the other were used as the registration primitives. The similarity measures were based on the Euclidean distance between a vertex and a surface patch, as well as the orientation compatibility of the two patches (quantified the comparison between the normal vectors of the vertices from the two surfaces). The weighted sum of these two measures formed generalized distances. A force field utilized the primitives

and the similarity measures to deform the surfaces, globally then locally, until the mean generalized distance was less than a threshold value. Following registration, corresponding points could be identified on the aligned surfaces. The cartilage thicknesses were measured at the locations of these corresponding points on the original cartilage surfaces (before deformation). Local changes were then determined by calculating the thickness differences between the corresponding locations.

The robustness of the method was tested with artificially corrupted cartilage surfaces at different SNRs and also at different surface resolutions. The results indicated that with a low SNR, the method could detect 67% of the corresponding vertices. Altering surface resolutions (600 versus 2400 triangles) did not produce any significant difference. In fact, the percentage of correctly identified points was slightly less for a higher resolution than a lower one possibly due to over-sampling of points on the surfaces. In-vivo MR data were also acquired for ten healthy subjects with the knee repositioned between datasets, and also with the subjects performing 30 knee bends outside the MR scanners. The measured cartilage thickness differences using the registration were compared to numerical results obtained from the Euclidean distance transformation algorithm (Stammberger et al., 1999), and a high correlation was reported for all cases. It also detected cartilage compression after the knee bend exercises. The authors concluded that local differences in cartilage thickness of approximately 1.0 mm could be reliably detected with this technique (based on image resolution of $0.31 \text{ mm} \times 0.31 \text{ mm} \times 1.5 \text{ mm}$).

Although the results showed successful registration with this elastic method, deforming the cartilage surfaces to impose a fit might pose problem especially when deformations or changes of these surfaces are of interest for studies of degenerative diseases such as OA. Elastic registration could force two surfaces to deform and align with each other even though they could be two different surfaces or contain different local features. However, this should not be an issue with using the bone-cartilage interface as it is valid to assume that this surface remains rigid within the scanning session. The author tested the robustness of the algorithm using simulated data and validated the cartilage thickness values by comparing to a numeric algorithm (Stammerger et al., 1999). However, no direct measure to quantify registration accuracy based on the two sets of MR data was reported by the authors.

2.5.2 Geomatics Registration

In the fields of photogrammetry and remote sensing, accurate surface matching strategies are crucial for the registration of 3D datasets. With advancing technologies in the hardware and software of data acquisition systems (e.g., earth-observation satellites, photogrammetric sensors, Light Detection and Ranging (LIDAR) systems), more accurate, robust, and automated registration approaches are required to handle these multi-source, multi-resolution, and multi-temporal 3D data (Habib et al., 2004, Habib and Al-Ruzouq, 2005). Similar to medical image registration, noise in the data and systematic differences caused by different imaging sensors challenge the registration

process and can affect the resulting accuracy. Also, geometric and radiometric characteristics of the same object can be different from two sets of data. Temporal changes (e.g., urban development) or movements (e.g., ice sheet movements) can further complicate the process.

Many surface matching techniques are developed and different approaches have been proposed to deal with these challenges (Brown, 1992). Conventional surface registration techniques required the interpolation of the datasets into a uniform grid, and the transformation relating the surfaces were solved for by minimizing elevation differences at corresponding grid posts (e.g., Ebner and Ohlhof, 1994). The interpolation process could introduce errors especially when dealing with datasets that have large variations in heights (e.g., urban areas) and minimizing elevation differences would only be valid for horizontal surfaces. Based on the limitations of the traditional methodology, the majority of the more recent techniques utilize a least squares approach that minimizes the distances between corresponding surface elements, without prior interpolation, to solve for the registration problem. The following subsections summarize several of these techniques which used different algorithmic approaches to solve the matching problem for data acquired by different means.

2.5.2.1 Registration of Laser Data to Photogrammetric Surfaces

Postolov et al. (1999) developed a surface registration algorithm for matching airborne laser data to surfaces generated by photogrammetric means. Although deriving transformation parameters using conjugate points between the two datasets would be straightforward, this approach was not feasible as identifying a corresponding point from a laser footprint to the same point captured by photogrammetry is almost impossible. Therefore, registration using higher order primitives (e.g., surfaces) was needed. The developed algorithm divided the transformation relating the surfaces into horizontal and vertical components. The resulting mathematical model was based on these two transformations. The horizontal transformation was characterized by two horizontal shifts, a rotation, and a scale factor. With the horizontal transformation established, the vertical component was introduced to describe the shift in elevation and leveling slopes in two directions. By combining these models, the height differences between the surfaces could be defined with the planar/horizontal parameters in a non-linear formulation. To solve for the parameters, this formulation was linearized and the elevation differences were minimized using standard least squares methods. The design matrix in the least squares algorithm required gradients, which were calculated by reconstructing small surface patches around a point of the photogrammetric data, using a planar or bilinear surface generation approach.

This algorithm was tested and validated using both synthetic and real datasets. A surface with known parametric function formed by randomly distributed points was used as the

synthetic data. Random noise was added to the elevations of these points. To validate the points derived from the surface registration algorithm, the same surface was created using a smaller set of points, and was transformed to a different reference frame using a known set of parameters. The estimated parameters were reported as similar to the true values, and elevation differences between the points of the two registered surfaces were smaller than the added noise. Small numbers of outliers were also reported as having minimal effect on the accuracy of the estimated parameters. The real dataset consisted of Airborne Topographic Mapper laser data and panchromatic aerial photography of the same urban site. Planar roof tops measured from the photographs were used as the reference surface and laser data points representing the same features were identified for the registration. The standard deviations of the parameters were better than 10 cm in both horizontal and vertical directions. The results also indicated that systematic differences existed between the two surfaces and were consistent over the area.

Although this algorithm worked with the original scattered point data without the need to interpolate into regular grid posts, it solved for the parameters by minimizing elevation differences, which would be valid only for horizontal surfaces (like Ebner and Ohlhof's technique, 1994). In fact, the authors emphasized that the algorithm was suitable for surfaces with relatively moderate slopes, and if the surface geometry was not sufficient, then not all the parameters could be accurately determined. The authors did not report numeric results from the experiments with synthetic data. Thus no clear conclusion could be taken from the paper regarding the algorithm accuracy.

2.5.2.2 Least Squares 3D Surface Matching

Gruen and Akca (2005) developed an algorithm for the least squares matching of 3D surfaces that were modeled by 3D point clouds. The transformation parameters were estimated by minimizing the sum of squares Euclidean distances between the surfaces using the Generalized Gauss-Markoff model. Random errors, which might originate from the discrepancies between imaging sensors or environmental conditions between the two sets of data, were also accounted for in the mathematical model. This resulted in observation equations that described for each surface element on the template surface ($f(x, y, z)$), there was an exact correspondent surface patch on the search surface ($g(x, y, z)$) by also considering the involved errors ($e(x, y, z)$):

$$f(x, y, z) - e(x, y, z) = g(x, y, z) \quad (2-5)$$

The 3D similarity transformation (three translations, three rotations, and a scale) was chosen to express the relationship between conjugate surface elements. To solve for the parameters, least squares minimization of the sum of squares Euclidean distances was used, which required linearization of the observation equations. The resultant functions were expressed as a Gauss-Markoff estimation model, which provided unbiased minimum variance estimation for the parameters as the least squares solution. Since local surface normals were required for the search surface as expressed as derivative terms in the mathematical model, the search surface was represented as planar surface patches. The authors also included a weighting scheme on the residual vectors based on the estimated standard deviations of the parameters to eliminate large outliers. Two

extensions to this basic mathematical model were also provided. The first extension allowed simultaneously matching of multiple sub-surface patches with relevant information, instead of the use of the full dataset, to provide a more computationally effective solution. The second extension enabled simultaneous matching of both surface geometry and intensity information, for data with geometrically-weak information.

Two applications were used to show the capabilities of the least squares matching method. The first example was the registration of three 3D point clouds of a petrochemical plant acquired by a laser scanner (HDS 2500, Leica Geosystems, average point spacing = 12 mm). The registration was shown to be successful with the average square root of the estimated variance factor to be 2.66 mm, using the full set of data. When the multi-subpatch approach was used for the same dataset, the system redundancy decreased, thus resulting in higher standard deviations for the estimated parameters. However, the square root estimated variance factor reduced to 2.05 mm. The second application utilized the intensity and geometry of the data for 3D matching. Laser scans of a wall painting in Neuschwanstein Castle, Germany, were matched (IMAGER 5003 laser scanner, Zoller+Frohlich, average point space = 3 mm) and results were successful with a root-mean-square error of 1.16 mm.

This least squares 3D surface matching technique allowed matching of two surfaces at any orientation, by minimizing Euclidean distances between conjugate features, instead of minimizing elevation differences. Also, by including intensity information, the

extension provided flexibility and allowed for more accurate estimation of the parameters when the geometrical information alone was not sufficient. The basic mathematical model could be modified with any transformation functions and surface representations. Thus it could be suitable for different applications and to properly model the deformations between surfaces. Consistent with the well known issue associated with least squares estimation, the convergence behavior of this method depended on the quality of the initial approximations and the datasets. The search for correspondent elements of the template surface on the search surface was computationally complex and required optimization algorithms and sophisticated software programs. These matters were not reported in this paper by Gruen and Akca as it was not the scope of their study. Additionally, although a weighting scheme was incorporated to suppress large outliers, occlusions and smaller outliers could also affect the estimated parameters. Overall, this developed algorithm successfully utilized the generalized least squares matching concept and allowed flexibility and extensions for any 3D matching applications.

2.5.2.3 Automatic Registration of 3D Views based on Spin-Image

Guarnieri et al. (2005) proposed a unique idea of using a Spin-Image approach to automatically recognize corresponding points in two laser scan views so that transformation parameters could be calculated by minimizing distances between the points. Spin-Image was originally developed by Johnson and Hebert (1999). The process describes each point, with a specific orientation and direction, on a surface mesh

by using an object-centered coordinate system (i.e., surface is described with respect to a coordinate system that is independent on the view of the surface). The relationship of the neighboring points to a specific point on a surface mesh can be described by using a cylindrical coordinate system, which comprises of a radial and elevation coordinates. The radial coordinate (α) is defined by the distance between the point and the line through the surface normal of the point of interest, and the elevation coordinate (β) describes a signed perpendicular distance from a point to a tangent plane defined by the vertex normal and position of the point. All the points that lie on a circumference of a circle relative to the point of interest will have the same α and β values. These two coordinates are stored using a 2D accumulator, which can be treated as a 2D image with darker cells indicating more points with a specific coordinate combination relative to the reference point. Spin-Images generated for corresponding points on two views of the same object will be similar, as they are based on the shape and surface characteristics of the object.

For surface matching, Guarnieri et al. generated Spin-Images for each point on two laser scan views and the images were matched to identify corresponding points. For these points, the Spin-Images would be similar but not identical due to the different discretization/sampling of the surface and noise associated with the data. Therefore, to identify corresponding points, a correlation coefficient was developed to identify/match Spin-Images that were strongly correlated. The identified corresponding points were then

used to calculate transformation parameters that were then utilized by the Iterated Closest Point (ICP) algorithm to derive the best alignment between the views.

Two laser scan views (ShapeGrabber 100, ShapeGrabber Inc., Ottawa, Canada) of a rubber cat object were matched using this proposed technique. The laser precision was 50 μm and the point spacing was 2 mm for surface modeling. Spin-Images were created and matched to identify corresponding points between the views. The results showed that by using only the Spin-Image algorithm, the maximum alignment error was 1.45 mm. This error improved to 0.80 mm after applying the ICP algorithm. A second experiment was conducted using a 3D model of a human vertebra, with improvement also found in the alignment (maximum error from 1.4 mm to 0.29 mm) after applying ICP based on the parameters estimated from the Spin-Image algorithm.

This Spin-Image algorithm worked exclusively with the intrinsic characteristics of the surface and did not rely on the coordinate systems of the data. It also had few restrictions on the object shape, thus could deal with data containing highly cluttered objects and occlusions. Although the results have shown accurate alignment of overlapping views, especially with the incorporation of ICP, generating Spin-Images could be computationally intensive especially when dealing with large objects modeled by many surface points. Also, since this technique depended on distinct patterns of surface topography, objects with poor surface geometry (e.g., building models) might result in incorrect alignment with this algorithm. This algorithm also assumed a point-to-point

correspondence between the two laser scan views, which could only be a valid assumption if the point density is high.

2.5.3 Registration Requirements and the Proposed Algorithm

Based on the literature review of existing techniques, some conclusions can be drawn regarding the requirements of the registration methodology. The following are the basic requirements of the methodology to be proposed for this research. Although these requirements can be generalized for most registration applications, they are specifically important for 3D MR data of joint structures.

- 1) Base on a rigid transformation (i.e., no deformation) to relate the surfaces,
- 2) Establish correspondence and solve for the transformation parameters,
- 3) Use proper matching criteria for surfaces at any orientation,
- 4) Need to be robust (i.e., errors or discrepancies would not affect accuracy), and
- 5) Has measures to quantify the quality (e.g., accuracy) of the registration.

With these requirements in mind, the proposed algorithm for this thesis research, developed by Habib et al. (2001) originally for geographic data, is a robust algorithm that allows simultaneous establishment of correspondences and estimation of transformation parameters. It can work with surfaces that are represented by randomly distributed points with unknown correspondences. A 3D similarity transformation is used to rigidly align the surfaces. The modified iterated Hough transform (MIHT) is used as the matching

strategy that is based on a voting scheme for solving for the transformation parameters and the correspondence between the surfaces. Matching between surfaces is performed locally, in that the smallest surface element (i.e. each point) is matched individually, which resulted in high registration accuracy. Matches and non-matches (i.e., errors or discrepancies) are identified and a least squares adjustment is used only on the matches to derive a robust registration solution. The accuracy of the algorithm was validated with different scenarios where noise and blunders were added to synthetic data (Habib et al., 2001). The results were accurate even with a 75% difference between the surfaces. The algorithm also correctly detected changes (blunders) between the two surfaces up to an accuracy of 99.9%. Overall, this algorithm can accurately estimate the transformation parameters between two surfaces for the synthetic data and can simultaneously identify changes or discrepancies between them.

2.6 Summary

The literature review have shown that in-vivo quantitative studies of joint biomechanics and health status are very important to understand the effects of joint injuries and diseases on joint and related tissue structures. Although many techniques are available for these studies, MRI is superior as it provides accurate measurements of joint properties non-invasively and allows studies of joint conditions without any harm to the subjects. Registration, along with other image processing techniques such as segmentation and reconstruction, are very important for analyses and comparisons of MR data that are

acquired under different conditions and at different times. Several existing registration techniques developed for both medical imaging and Geomatics engineering applications were reviewed and requirements were derived as a result for registration of 3D MR data of joint structures. The proposed algorithm for this thesis research, originally developed in the field of Geomatics engineering, was introduced as it meets the requirements of the registration methodology.

Chapter Three: Surface Matching Algorithm

3.1 Introduction

This chapter provides a detailed review of the methodology of the proposed surface matching algorithm (Habib et al., 2001). The rationale behind the choices of the four registration paradigm components: registration primitives, transformation function, similarity measure, and matching strategy, will also be addressed. This surface matching algorithm was employed in this thesis research to achieve the four study specific aims, and details of these will be presented in the following chapters.

3.2 Registration Paradigm

3.2.1 Registration Primitives

Primitives are the utilized features for representing and relating the involved datasets in the registration process. For surfaces, the most commonly used registration primitives include points, lines, and areal patches. The chosen primitives depend on the characteristics of the involved data and will directly influence the mechanics and formulation of subsequent components of the registration paradigm. Thus it is important to decide on appropriate primitives to represent the surfaces. The proposed surface

matching algorithm works with the raw format of the data, thus the two surfaces can be represented by irregularly distributed 3D points that are not necessarily conjugate (i.e., there is no known point-to-point correspondence between the two surfaces). The two surfaces can also be given relative to different reference frames. Point primitive is suitable for both geographic and medical data, where features of interest are represented by a cloud of randomly distributed points that are spatially defined by their 3D coordinates, via systems such as the LIDAR laser-scanning systems and MRI. Linear features can be commonly found in man-made scenes (e.g., buildings and roads), but processing is needed to extract them from 3D point clouds. In contrast, linear features are not typically found in anatomical structures. Areal primitives (e.g., regions) can be identified in both geographical (e.g., lakes) and medical (e.g., organs) data but processing of 3D point data is also needed to extract and represent these features.

In general, two sets of data can be acquired from different viewpoints, under different conditions, and/or at different times. Thus no point-to-point correspondence should be assumed between the surfaces. To allow the surface matching algorithm to identify conjugate surface elements, points in one of the surfaces are further processed to form triangular patches, similar to a triangular irregular network. If the two datasets are acquired by the same sensor (e.g., registration of two MR datasets), they would exhibit the same data characteristics (e.g., point density). Consequently, the algorithm and results would not be affected by the choice of surface presentation for each dataset (i.e., which surface is represented by points and which is represented by patches). Deviations

between a set of results and those obtained after swapping the representation schemes would not exceed the noise level in the implemented data. To summarize, the registration primitives used in the proposed surface matching algorithm were selected as points for the first surface (S_1) and triangular patches for the second surface (S_2) (Figure 3-1).

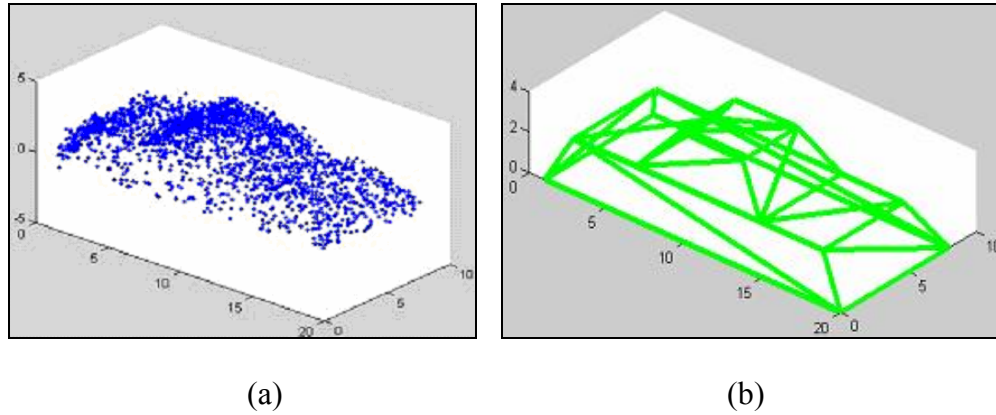


Figure 3-1: Registration primitives for the proposed surface matching algorithm: points for S_1 (a) and triangular patches for S_2 (b).

3.2.2 Transformation Function

Generally, the involved datasets for the registration are given with respect to different reference frames. The transformation function describes the mathematical relationship or mapping function between the reference frames associated with the two surfaces. More specifically, the transformation parameters of the chosen function align the primitives from S_1 onto the corresponding primitives from S_2 , with S_2 being the reference surface for registration. The chosen transformation function for the proposed surface registration is 3D similarity. This includes seven parameters: three translations along the X, Y, and Z coordinate axes (X_T , Y_T , Z_T), three rotations about the three coordinate axes

(ω, ϕ, κ) , and a scale factor (S) describing the overall scale difference between the two surfaces (Equation 3-1). These seven parameters relating S_1 and S_2 are assumed to be unknowns and are solved for as part of the registration problem.

$$\begin{bmatrix} X' \\ Y' \\ Z' \end{bmatrix} = \begin{bmatrix} X_T \\ Y_T \\ Z_T \end{bmatrix} + S \times R(\omega, \phi, \kappa) \begin{bmatrix} X \\ Y \\ Z \end{bmatrix} \quad (3-1)$$

Where: X, Y, Z are the coordinates of a point on the first surface S_1 ,

X', Y', Z' are coordinates of the transformed point with respect to the second surface S_2 reference frame, and

R is a 3 by 3 matrix that describes the rotational relationship between the involved reference frames.

The 3D similarity transformation is a global rigid body transformation, implying that one set of transformation parameters is used to entirely relate the two surfaces. Moreover, a rigid transformation assumes the absence of any deformations between the two surfaces that cannot be modeled by a rigid body transformation. However, the presence of these deformations can be inferred by evaluating the quality of fit between the registered surfaces. 3D similarity preserves shapes (i.e., preserves angles) after the transformation; and if the scale factor is fixed at one, this transformation will also preserve distances between surface points. Although the 3D similarity transformation was chosen, any other transformation functions could also be adapted into the algorithm to model the geometric relationships and deformations between the surfaces.

3.2.3 Similarity Measure

The similarity measure mathematically describes the coincidence of conjugate registration primitives after performing the appropriate transformation function. The formulation of the similarity measure depends on the choice of primitives as well as the utilized transformation function. Since points and patches are used as the registration primitives to describe the involved surfaces (S_1 and S_2 , respectively), the similarity measure has to constrain the correspondence between a point from S_1 to a conjugate triangular patch from S_2 after performing the transformation. The constraint can specify that a transformed point, q' , from S_1 , is coplanar (i.e., belongs to the same plane) with its conjugate patch from S_2 as defined by its vertices p_a , p_b , and p_c (Figure 3-2). Thus, if the point q is assumed to belong to a specific surface patch, the normal distance (d) between q' , obtained after applying the appropriate 3D similarity transformation on q , and the corresponding patch in S_2 should be zero. This condition is known as the coplanarity condition (Equation 3-2), which states that the volume enclosed by a point and the corresponding patch is zero. The seven unknown 3D similarity transformation parameters are implicitly expressed in the first row of this coplanarity condition matrix (Equation 3-3). This coplanarity condition can also be expressed in terms of the normal distance (d) (Equations 3-4 and 3-5).

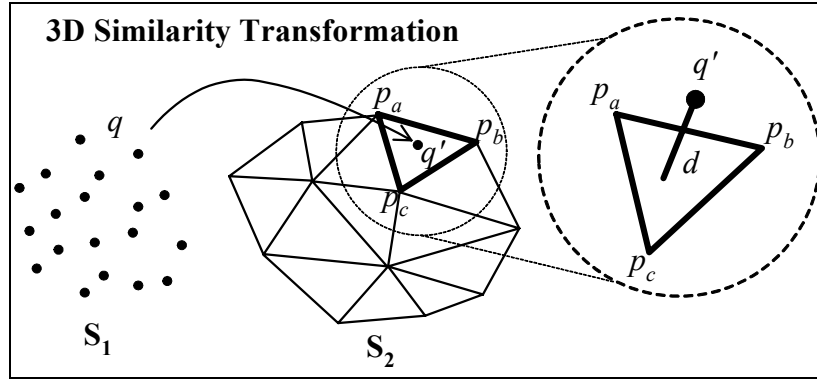


Figure 3-2: Coplanarity condition describes the correspondence between a point in S_1 and a patch in S_2 after performing 3D similarity transformation.

$$V = \begin{vmatrix} X_{q'} & Y_{q'} & Z_{q'} & 1 \\ X_{p_a} & Y_{p_a} & Z_{p_a} & 1 \\ X_{p_b} & Y_{p_b} & Z_{p_b} & 1 \\ X_{p_c} & Y_{p_c} & Z_{p_c} & 1 \end{vmatrix} = 0 \quad (3-2)$$

$$\text{Where: } \begin{bmatrix} X_{q'} \\ Y_{q'} \\ Z_{q'} \end{bmatrix} = \begin{bmatrix} X_T \\ Y_T \\ Z_T \end{bmatrix} + SR(\omega, \phi, \kappa) \begin{bmatrix} X_q \\ Y_q \\ Z_q \end{bmatrix} \quad (3-3)$$

$$d = \frac{V}{\sqrt{V_1^2 + V_2^2 + V_3^2}} = 0 \quad (3-4)$$

Where:

$$V_1 = \begin{vmatrix} Y_{p_a} & Z_{p_a} & 1 \\ Y_{p_b} & Z_{p_b} & 1 \\ Y_{p_c} & Z_{p_c} & 1 \end{vmatrix} = 0, \quad V_2 = \begin{vmatrix} X_{p_a} & Z_{p_a} & 1 \\ X_{p_b} & Z_{p_b} & 1 \\ X_{p_c} & Z_{p_c} & 1 \end{vmatrix} = 0, \quad V_3 = \begin{vmatrix} Y_{p_a} & Y_{p_a} & 1 \\ Y_{p_b} & Y_{p_b} & 1 \\ Y_{p_c} & Y_{p_c} & 1 \end{vmatrix} = 0 \quad (3-5)$$

If more than seven conjugate point-patch pairs are identified, the seven unknown transformation parameters (Equation 3-3) can be solved for by satisfying the coplanarity constraints (Equation 3-2) through a least squares adjustment procedure. It should be noted that this similarity measure minimizes the normal distances between corresponding points and patches to solve for the parameters, rather than reducing elevation differences between the surfaces (e.g., Ebner and Ohlhof's technique, 1994). Thus, it is valid for surfaces with any orientation as in the case for large-scale laser-scan data and MR imagery.

Accurate solution of the parameters of the transformation function requires surface patches with varying orientation. For example, planes normal to the X axis will only allow for estimating the shift component in the X direction, X_T , as well as the rotations φ and κ (Figure 3-3). Planes normal to the Y axis can help to solve for Y_T , ω and κ . In the same manner, planes normal to the Z-axis will estimate the Z_T and the rotation angles ω and φ . Two parallel patches in any orientation are needed to derive the scale factor. Therefore, in generally, four planes (e.g., three intersecting planes and another plane that is parallel to one of the three planes) are the minimum requirement to solve for the seven parameters. The importance of surface geometry can be visualized with a simple example: consider the registration of two spheres. Any orientations or rotations along the main axes of the spheres can result in a perfect match. However, if a square pyramid is attached to the spheres, then this unique geometry will constrain the registration where the pyramids have to align for the two surfaces to match. Therefore, as a rule of thumb,

the involved surfaces should have sufficient geometry (i.e., patches with varying orientations) to allow accurate estimations of the transformation parameters.

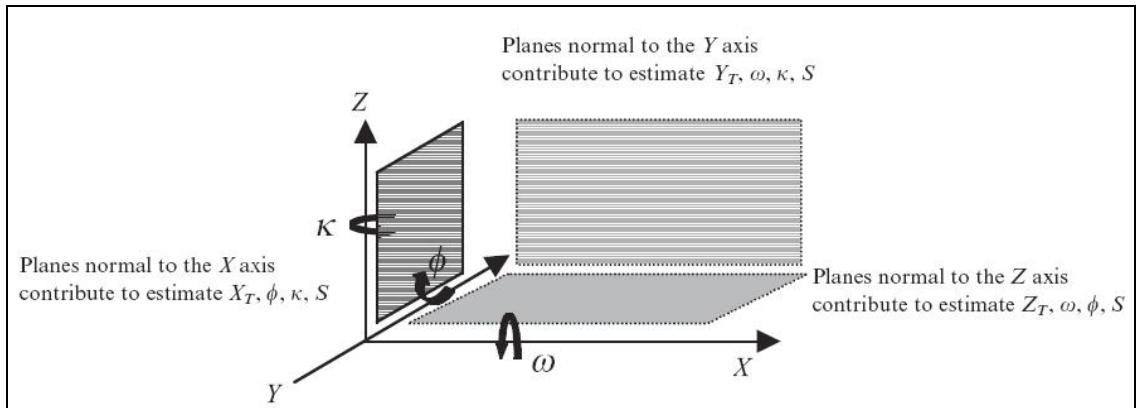


Figure 3-3: Relationship between the seven transformation parameters and the orientation/geometry of the surface patches (Habib et al., 2001).

3.2.4 Matching Strategy

The matching strategy is an optimization procedure that utilizes the primitives, transformation function, and similarity measure to automate the registration procedure by establishing the correspondences between conjugate surface elements as well as estimating the parameters of the transformation function. As discussed, if seven or more conjugate point-patch pairs are identified, the transformation parameters can be solved for using the coplanarity constraints (Equation 3-2). However, since the correspondences between the two surfaces are typically unknown, conjugate point-patch pairs have to be identified either manually or automatically. Manual identification of conjugate point-patch pairs is difficult if not impossible especially when considering the volume and density of involved datasets. Also, with anatomical features, it is extremely difficult to

identify conjugate surface elements especially for smooth and contiguous joint surfaces. Therefore, matching strategies are adapted to overcome this issue by automatically search for correspondences between datasets. For the proposed surface matching algorithm, the Modified Iterated Hough Transform (MIHT) is utilized as the matching strategy, which is based on a voting scheme to simultaneously establish the correspondences between surface elements and solve for the transformation parameters.

The role of the voting scheme within the MIHT is to identify the most probable solution (the highest vote) for the transformation parameters by considering all possible matches between points in S_1 and patches in S_2 . To illustrate this voting concept, one can consider any seven points in S_1 and any seven patches in S_2 . If each of the seven points is assumed to match with one of the seven patches, the relationship between these seven pairs can be described by a set of 3D similarity transformation parameters that results from the solution to the seven coplanarity constraints (Equation 3-2). Another seven point-patch pairs can be chosen to derive another set of parameters. If this process is repeated for all possible matches between the surfaces, while keeping track of the derived solutions for the parameters, the correct matches should result in the same set of solutions. Therefore, the voting scheme will simultaneously establish the correspondences between conjugate primitives as well as derive an estimate of the transformation parameters.

To keep track of the parameter solutions from all the hypothesized matches, a seven-dimensional accumulator array is required, where the cells of the array are used to record

the frequency of each solution vector. The same solution set resulting from the correct matches will have the highest votes/counts and will manifest itself as a peak in the accumulator array, and these values are the most probable estimates for the transformation parameters. However, when dealing with a large number of primitives, the use of a seven-dimensional accumulator array to keep track of possible primitive pairings is computationally intensive and will eventually lead to a combinatorial and memory explosion. To overcome this problem, the MIHT approach solves for the parameters sequentially and iteratively by implementing a one-dimensional accumulator array while considering one parameter and one hypothesized matching pair at a time. Thus, the MIHT procedure replaces the seven-dimensional accumulator array with seven one-dimensional accumulator arrays while working only with a single matching pair at a time.

3.3 Automated Surface Matching and Registration Methodology

The proposed matching and registration methodology begins by setting up initial approximations for the seven unknown parameters of the 3D similarity transformation. Although the algorithm has shown to produce accurate results with poor initial approximations (Habib et al., 2001), it is beneficial to have educated estimates for the approximations based on a-priori information obtained from the involved datasets (e.g., visual evaluation of the geometrical relationship between the two surfaces). The points from S_1 are transformed using this set of initial approximated parameters. Using the

MIHT approach, correspondence is established and the parameters are estimated in an iterative process. To estimate one of the parameters, for example X_T , the approximated values of the other parameters are considered to be correct. Then each transformed point is hypothesized to match with each of the triangular patches from the reference surface S_2 , and X_T can be solved for as a one-dimensional problem by satisfying the coplanarity constraint. A one-dimensional accumulator array keeps track of the derived solutions for X_T from all the possible hypothesized point-patch pairs. The peak of the populated accumulator array will indicate the most probable solution for X_T (Figure 3-4), and the initial approximation is updated with this peak value. This estimation process is then repeated sequentially for each of the remaining six parameters.

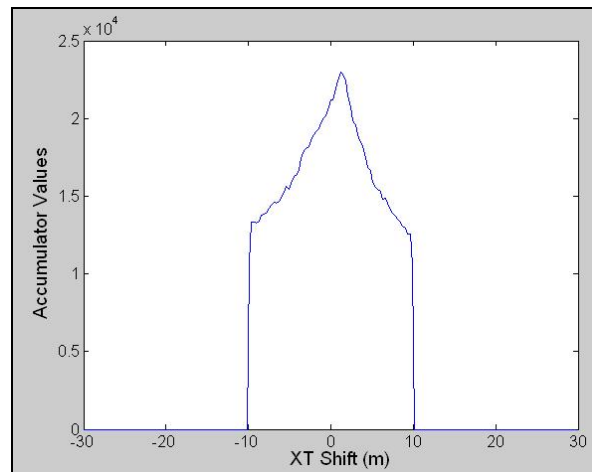


Figure 3-4: An accumulator array with the peak indicating the most probable solution for the parameter in question.

The accumulator array is a discrete tessellation of the expected solution range of the parameter in question. The cell size and range of the accumulator array (i.e., the allowable minimum and maximum values) depend on the quality of the approximate

values for the non-considered parameters (i.e., the remaining six parameters with fixed values). Therefore, rough initial approximations should be compensated for by a larger range of allowable values and larger cell size. After the first round of estimation for the seven parameters, the iteration procedure is repeated while decreasing the cell size of the accumulator array as well as its range to reflect the improvement in the derived estimates of the transformation parameters. A smaller range reflects the improvement in precision of the estimated parameter, while a smaller cell size reflects the improvement in the quality of the remaining parameters. In this manner, the unknown parameters are iteratively solved for in a coarse-to-fine strategy and will converge to the most probable solution. Convergence is achieved when there is no significant change (i.e., below threshold value) in the estimated parameters between two successive iterations.

Clearly, the starting and ending cell sizes and the number of iterations can affect the final quality of the parameter estimates. A larger cell size should be used to compensate for poor approximations, but a cell size that is too large would be meaningless as all solutions (both correct and incorrect) will contribute to the same narrow peak in the accumulator array (Figure 3-5a). In contrast, if the cell size is too small, then the noise effect might lead to two correct point-patch pairs contributing to two slightly different sets of parameters, thus no distinct peak will be apparent to indicate the most probable solutions (Figure 3-5b). Therefore, it is important to assess the qualities of the data (e.g., noise level) and the initial approximations, so the appropriate start and ending cell sizes can be chosen to allow the array to capture the best estimates. Also, the number of

iterations (i.e., the number of reductions in cell size) should be adequate to allow a gradual control of the precisions of the parameter estimates. A small number of iterations will result in a quick jump from a large to small cell size, which means that estimates with poor precision will be used to derive the parameters that are supposed to have much higher precision. This can lead to the convergence to incorrect solutions. Although using a large number of iterations can increase the control of the convergence and the quality of the estimates, it can also significantly increase the run-time of the algorithm.

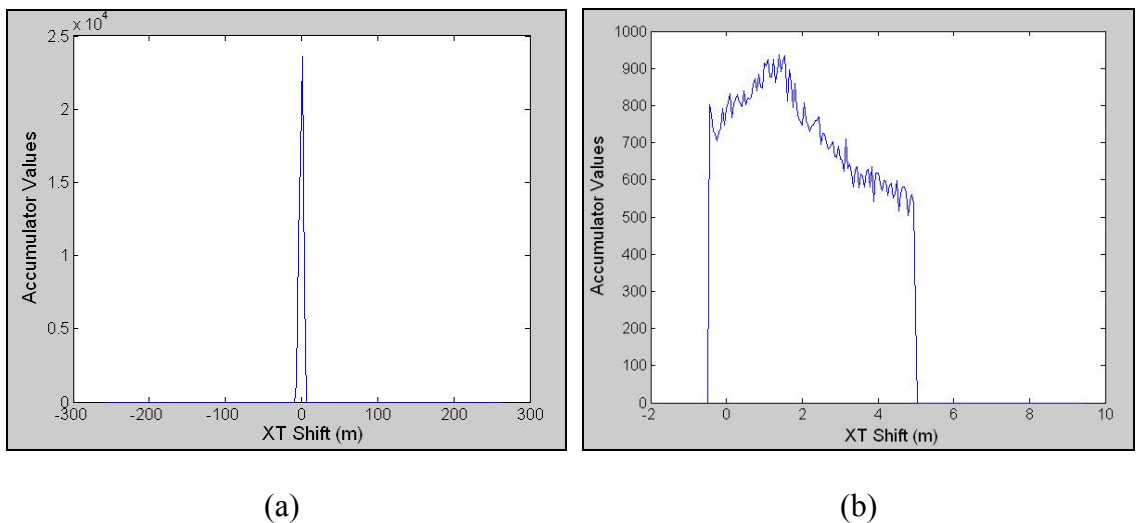


Figure 3-5: An accumulator array with a large cell size can result in all solutions contributing to one distinct peak (a), while a cell size that is too small will have no distinct peak to indicate the best solution (b).

Following the last iteration of the MIHT procedures, the matching points and patches (i.e., the matches that contribute to the peaks of the accumulative arrays) are used in a least squares adjustment to estimate the transformation parameters. The estimates derived from the last iteration of the MITH provide highly accurate approximations for the

adjustment. The non-matching points, which could be errors or differences between the two surfaces, are excluded from the adjustment process thus resulting in a highly robust registration. Habib et al. (2001) reported that the estimated parameters were accurate even with a 75% difference between the surfaces. The algorithm also correctly detected blunders between the two surfaces up to an accuracy of 99.9%.

3.4 Outcome Measures

The quality of fit between the registered surfaces can be measured by the estimated variance component (also known as the a posteriori variance factor) resulting from the least squares adjustment procedure. A smaller variance component indicates a better fit. This variance component is only a relative measure for comparisons between different results. A direct measure to quantify the quality of the registration is the Root Mean Squares (RMS) of the normal distances between the matched point-patch pairs after performing the transformation with the final parameter estimates. The RMS of the normal distances provides a meaningful measure to quantify the quality of fit between the two surfaces, but it does not describe the absolute accuracy of the registration. The RMS distance is calculated only from the matching point-patch pairs but does not account for the non-matches. Consequently, a small RMS distance can be achieved even though only a small section of the surfaces are matching. Thus, the percentages of the matched and unmatched points can provide indications about both the quality of the registration and also the amount of difference between the surfaces. To truly evaluate the accuracy of the

registration, the estimated transformation parameters can be validated against the true values (i.e., gold standards) if these are available.

In addition to quantitative measures, qualitative assessments of the matching results are also necessary to confirm the success of the registration. This can be performed by displaying the matching and non-matching points from S_1 , transformed using the estimated parameters, onto the reference surface S_2 . This can show how well the surfaces are registered and provide insights on why certain points are classified as non-matches. To further investigate why certain points/areas are not matching, the points can also be projected onto the original images or models of the datasets if they are available, so that the reasons for the non-matches can be justified (e.g., a new building or osteophytes that are found in only one of the datasets). Another visualization tool for assessment is to create image mosaics (i.e., the superimposition of two registered images) for the registered datasets. This can allow direct visualization of the surface alignment and comparisons of the two images.

3.5 Summary of Surface Matching Methodology

The proposed automated surface matching and registration procedure (Figure 3-6) provides a rigid registration between two surfaces based on a 3D similarity transformation and can detect errors and/or differences between them. The algorithm simultaneously establishes correspondence by identifying conjugate surface elements and

estimates the transformation parameters through a voting process. The final least squares adjustment procedure estimates the transformation parameters that best align the surfaces, with the non-matches excluded from the adjustment to produce highly robust results. The RMS of the normal distance provides a direct measure to quantify the quality of the registration.

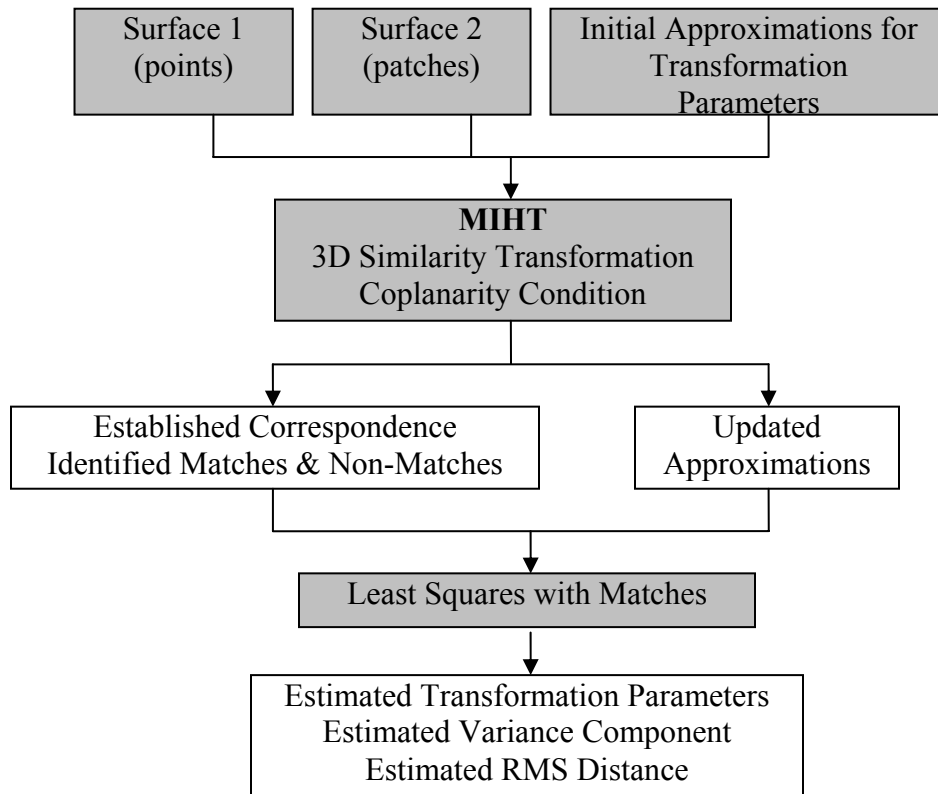


Figure 3-6: Methodology of the proposed surface matching algorithm.

3.6 Summary

This chapter presented in details the proposed surface matching algorithm based on the Modified Iterated Hough Transform developed by Habib et al. (2001). This algorithm

met the proposed requirements for registration of 3D MR data of joint structures defined in section 2.5.3. It works with surfaces at any orientation and can simultaneously establish the correspondence between surface elements and solve for the transformation parameters. It is also a highly robust algorithm that does not deform the surfaces of interest. Quantitative measures are also derived to describe the quality of the registration. A limitation of the surface matching algorithm is that it may not be feasible for handling high density data in the presence of noise (e.g., MRI data). The next chapter presents this limitation and the modifications implemented to address this issue, as part of the work for the first specific aim of this thesis research. Verifications of the modified algorithm with high density data in Geomatics engineering applications will also be presented.

Chapter Four: Algorithm Limitation, Implemented Modifications, and Verifications with Geomatics Applications

4.1 Introduction

This chapter presents a limitation of the proposed surface matching algorithm, which inhibited its use for high density and noisy data such as MRI or LIDAR. Modifications developed to overcome this limitation are described. Verifications of the modified algorithm were performed with high density datasets for three Geomatics engineering applications. The experiments and results are also summarized in this chapter. The research describes in this chapter addresses the first specific aim of this thesis research as outlined in the Introduction chapter (section 1.2).

4.2 Algorithm Limitation for High Density Datasets

Inherent noise in the data acquisition and possible errors introduced by data processing (e.g., measurement units in LIDAR and feature digitization in MRI) introduced convergence problems for the MIHT algorithm. The probability of non-convergence increases with increase in the density of the surface points, reaching a critical stage when

this density is almost equivalent to the level of the noise in the acquired points. This problem should be expected to occur when dealing with high resolution laser scanning and MRI data, where the triangular patches formed from the high density point clouds are very small in size, and this size is similar to the noise level. For example, LIDAR point clouds can have an average point spacing of approximately 0.7 m (i.e., size of the triangular patch). This is similar to the expected noise levels found for LIDAR data (approximately 0.5 m and 0.2 m in the horizontal and vertical directions, respectively).

A pilot study was performed to investigate this limitation of the MIHT algorithm. MR images of a knee joint was used in this pilot study (Figure 4-1a), which were acquired by a 3-telsa MR unit (General Electric Medical Systems, Waukesha, Wisconsin, USA) with a proton density fast spin echo sequence (sagittal, resolution: $0.273 \text{ mm} \times 0.273 \text{ mm} \times 4 \text{ mm}$). Noise in MR images can result in an overall grainy appearance in the image. This means that adjacent pixels can appear to have different signal intensities even if they belong to the same tissue (Figure 4-1b). The MIHT surface matching algorithm was applied to register femoral surfaces generated from this dataset (details about surface digitization and modeling from MRI will be discussed in the next chapter). The results from this pilot study demonstrated that the parameter convergence was rough, with oscillations of the solution found during the last iterations (Figure 4-2). These were caused by the fact that a point could match with either one of two (or more) adjacent patches and could still result in very similar transformation parameters. These

convergence problems should be expected when the MITH algorithm is applied for any types of high density and noisy datasets.

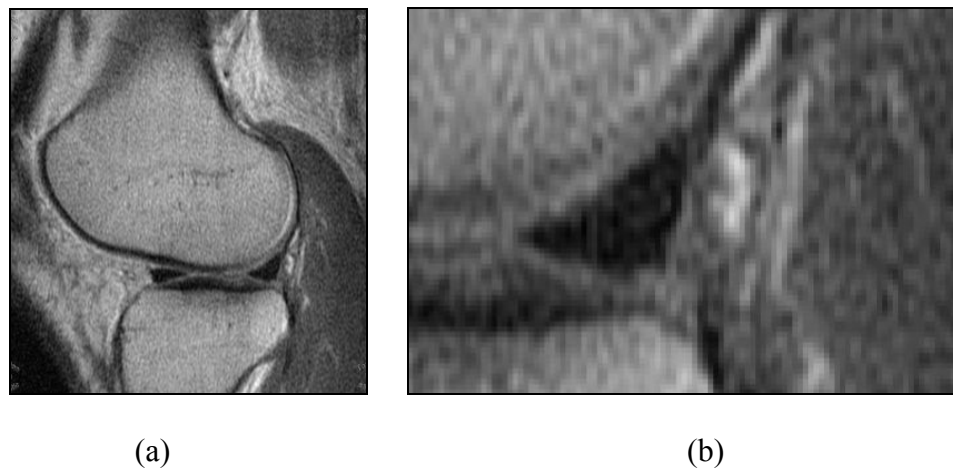


Figure 4-1: MR image of a knee joint acquired by a proton density fast spin echo sequence (a). A zoomed-in portion of the image shows the presence of noise (b).

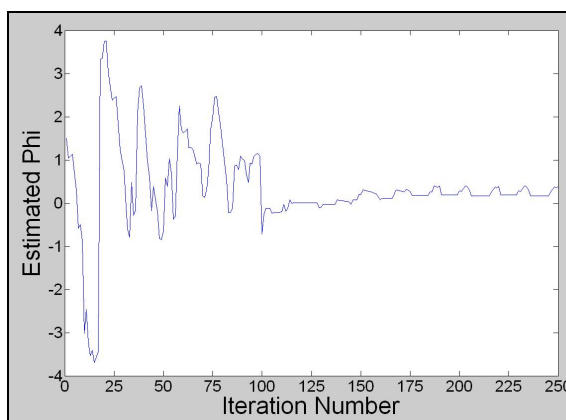


Figure 4-2: Rough convergence for the angle ϕ based on the MIHT approach with the ending iterations showing oscillations between different solutions.

4.3 Modifications to Accommodate High Density and Noisy Datasets

To overcome the limitation of MIHT for working with high density data in the presence of noise, a modification was implemented to the original algorithm to achieve the first specific aim of this thesis research. For this modification, the MIHT algorithm was complemented by the Iterative Closest Point (ICP) algorithm (Besl and McKay, 1992). The ICP algorithm was incorporated as an additional matching strategy to efficiently establish correspondences and solve for the seven transformation parameters.

4.3.1 Iterative Closest Point

The ICP algorithm, originally proposed by Besl and McKay (1992), has been modified by several groups (e.g., Zhang, 1994, Bergevin et al., 1996). In general, with a set of initial approximations for the transformation parameters, the ICP algorithm performs rigid registration of 3D data by iterating through three main steps until the solutions remained constant (i.e. below a threshold value) between iterations:

- 1) Establish correspondence between datasets by identifying conjugate surface features (i.e., find the closest point to a given patch).
- 2) Estimate the transformation parameters relating the first surface to the reference surface by minimizing the summation of normal distances between identified conjugate features.
- 3) Apply estimated parameters to transform the first dataset to the new position.

ICP has shown to yield quick convergence of the parameters and can handle a reasonable amount of normally distributed noise. However, there are some known issues with this algorithm. First, ICP converges quickly to a local minimum thus it is crucial to have good initial approximations that are relatively close to the true values. Also, for the same reason, outliers in the data can affect the results, potentially leading to incorrect registration. As for any registration problem, sufficient surface geometry is also essential for aligning the datasets.

The following sub-section describes the modifications that were implemented in this thesis research by incorporating the ICP algorithm as part of the surface matching approach to overcome the limitation MIHT has with high density data. Conversely, the abovementioned issues of the ICP algorithm are compensated for by the MIHT approach. Thus, these two complementary algorithms are used as the surface matching strategies for the modified surface matching algorithm.

4.3.2 Modified surface matching algorithm with MIHT and ICP

ICP requires good initial approximations for the transformation parameters. The combination of the MIHT and ICP strategies is optimal since the MIHT procedure will ensure the availability of good approximations, which could be further refined through the ICP approach. With the approximate parameters, the ICP algorithm finds the closest patch in the second/reference surface (S_2) for each point in the first surface (S_1) and

considers them as a matching pair. In the implementation of the ICP algorithm for this thesis research, a point and a patch are considered a matching pair if both of the following criteria are satisfied (Figure 4-3):

(i) Shortest normal distance: A point matches a patch when the normal distance between this point and the patch is less than a certain threshold and is also the shortest distance compared to the other patches. The threshold value is set by considering the amount of noise inherent in the involved data.

(ii) Projected point is inside the patch: A point only matches with a patch if its projection onto the patch is inside the polygon defined by its vertices. The decision of whether the projected point is inside or outside the patch is determined by the number of intersections a shooting ray from that point makes with the edges of the patch. An odd number of intersections indicate that the projected point lies inside the patch, while an even number means that it is outside the patch.

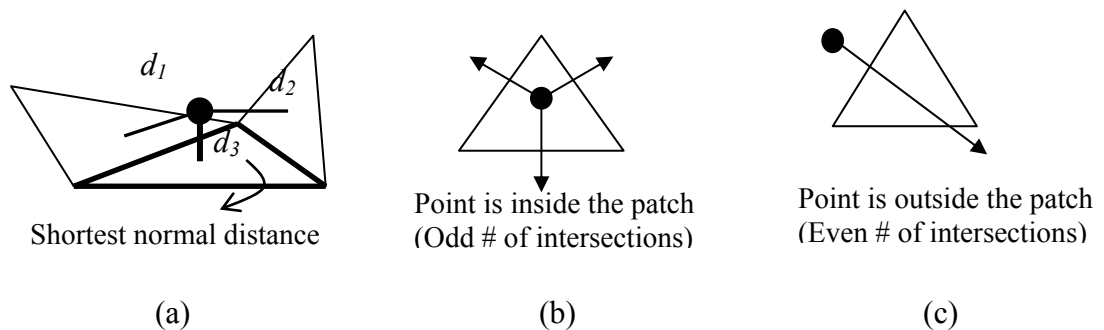


Figure 4-3: Matching criterion (i): shortest normal distance (a) and matching criterion (ii): projected point is inside the patch (b and c).

Using the resulting matches between the points in S_1 and the patches in S_2 , the ICP procedure estimates an updated solution vector for the seven parameters through a least squares adjustment process by minimizing the summation of normal distances between the matches. The estimated transformation parameters from the adjustment are then applied to transform the entire points in S_1 . From this, updated matching pairs between S_1 and S_2 are derived, which are then used to update the solution vector. This procedure is repeated in this manner until convergence occurs, where the estimated parameters do not significantly change between two successive iterations. This convergence condition can be checked by comparing the estimated variance components from the least squares adjustment between consecutive iterations. If the differences between them are less than a predefined threshold, then convergence is reached. For this ICP procedure, identified unmatched points based on the matching criteria can be classified as changes or blunders. Similar to MIHT, these non-matches are excluded from the adjustment process for the parameter estimations thus resulting in a highly robust algorithm. Figure 4-4 summarizes the surface matching methodology of the combined MIHT and ICP approach.

The outcome measures from the original approach are also derived for the MIHT/ICP approach for quantitative and qualitative analyses of the results. These measures include the estimated transformation parameters, estimated variance component, RMS of the normal distance, and a list of the matching and non-matching points.

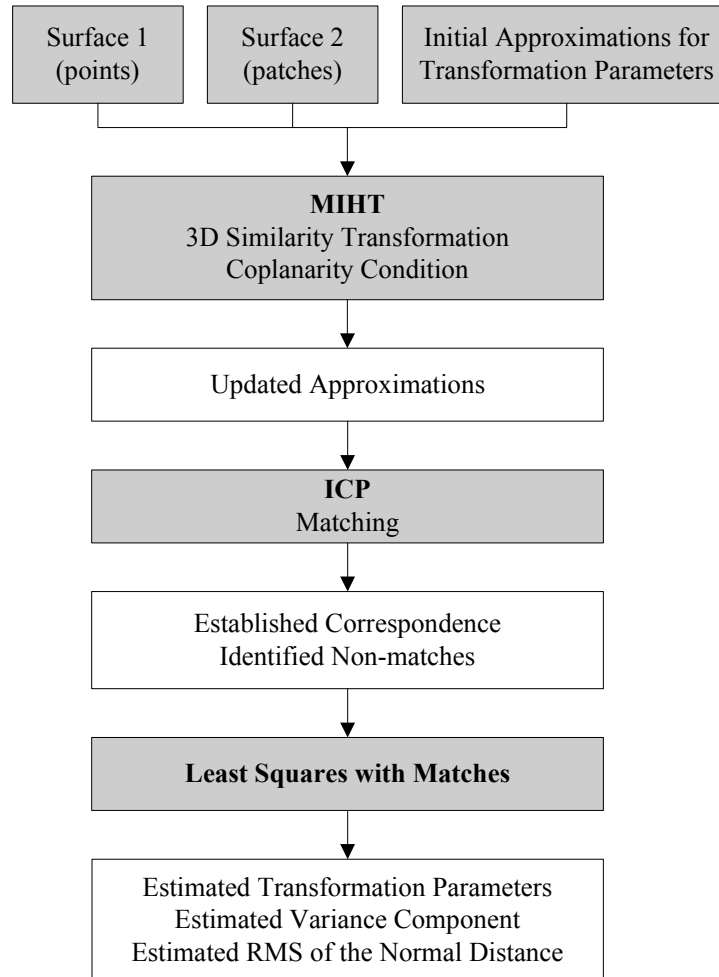


Figure 4-4: Surface matching algorithm with the combined MIHT/ICP approach.

For comparison of the original and the modified algorithm, the MIHT/ICP approach was applied to the MR dataset used in the pilot study for the investigation of the MIHT limitation (refer to section 4.2). Evaluation of the convergence of the parameter based on the MIHT approach and the combined MIHT/ICP approach clearly shows that ICP complements MIHT and refines the convergence of the parameter (Figure 4-5). Also, MIHT is utilized here to provide good initial approximations for the ICP algorithm. Thus,

a smaller number of MIHT iterations is required (10 iterations versus 250 iterations, Figure 4-5), which also speeds up the total process time of the algorithm (1 minute for the MIHT/ICP approach versus 1 hour for the MIHT approach).

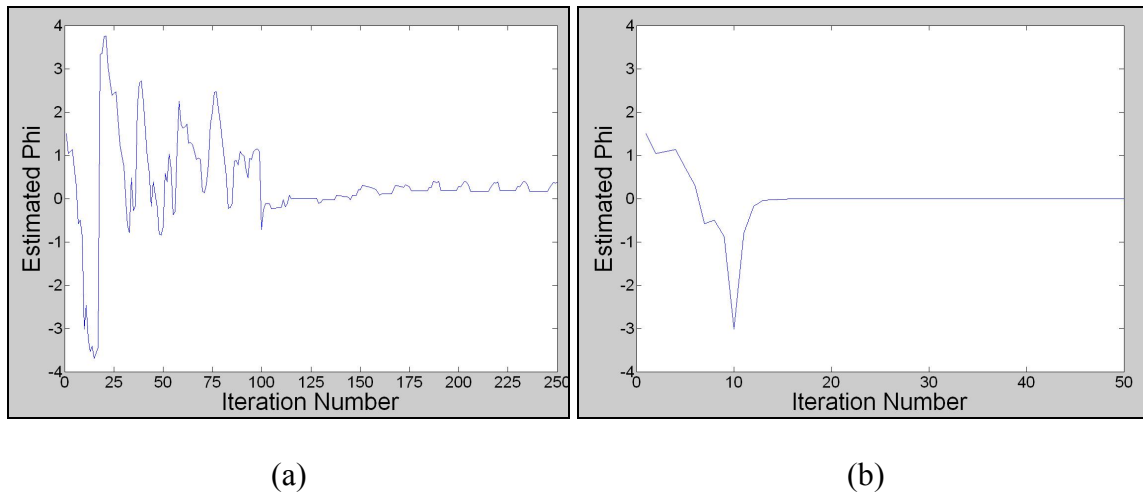


Figure 4-5: Convergence for the angle ϕ using only the MIHT approach (250 iterations) (a) and using the combined MIHT/ICP approach (10 MIHT with 40 ICP iterations) (b).

4.4 Geomatics Applications

The modified algorithm was applied to high density datasets acquired by Geomatics engineering techniques to verify its operation with high density data. This section includes the details and results of three Geomatics engineering applications with the modified algorithm, including: 1) LIDAR data of an urban city, 2) facial measurements using stereophotogrammetry, and 3) close-range laser scanning of a small object. The results from these applications demonstrate that the modified algorithm can be used to accurately register high density 3D datasets. The implications of these results on the efficacy of the combined MIHT and ICP algorithm for MRI applications are discussed.

4.4.1 Light Detection and Ranging Data of Urban City

LIDAR systems have been rapidly emerging as a fast, accurate, and cost-effective technology for acquiring high density 3D data representing physical surfaces. LIDAR systems are directly geo-referenced using global positioning systems (GPS) combined with high-end inertial navigation systems (INS), resulting in direct and accurate acquisition of 3D coordinates of irregularly distributed object space points at high density (Wehr and Lohr, 1999). Modern LIDAR systems can also capture intensity images over the mapped objects. As a result of these advances, LIDAR is being more extensively used in mapping and geographic information system applications, and can be combined with photogrammetric systems to provide complementary and complete surface information (Habib et al., 2004).

This application demonstrates the feasibility of the modified surface matching algorithm to register overlapping LIDAR datasets. To validate the surface matching algorithm, results were compared to ones derived using linear features that were accurately and reliably extracted from the same LIDAR dataset. The extraction of the linear features commenced with the identification of planar patches by plane fitting to LIDAR point clouds. Subsequently, neighboring planar patches with different orientation (e.g., two rooftops) were intersected to produce the linear features. This procedure resulted in linear features that were higher in accuracy than the LIDAR data itself. Therefore, registration by utilizing linear features can provide highly accurate results (Habib et al.,

2005). Differences between surface matching and linear features results should be within the noise level of the LIDAR data in order to validate the surface matching algorithm.

4.4.1.1 Data and Experiments

The utilized LIDAR data covers an urban area in Brazil and is given with respect to the World Geodetic System 1984 (WGS84) reference frame. This dataset was captured by an Optech ALTM 2050 airborne laser scanner (The Optech Incorporated, Toronto, Canada) from an average flying height of 975 m. The point density for these laser scan strips was approximately 2.24 points/m² (~0.7 m point spacing, i.e., high density). According to the flight and sensor specifications, this data was expected to have a horizontal accuracy of 0.5 m and a vertical accuracy of 0.15 m. Two adjacent and partially overlapping LIDAR strips were used for the registration, which mainly covered buildings, vegetations (e.g., trees), roads, and other man-made structures (Figure 4-6). The two strips or surfaces, S_1 and S_2 , comprised of 44,156 and 22,799 points, respectively. The 22,799 points of S_2 were further processed to generate 45,520 triangular patches based on Delaunay triangulation in MATLAB (The Mathworks, Inc., Natick, MA, version 6.5) (Figure 4-7b). The nature of LIDAR data acquisition substantially limited the number of points captured on the vertical facets of buildings (blank areas in Figure 4-7a). The modified surface matching algorithm was applied to register the points from S_1 to the patches of S_2 .

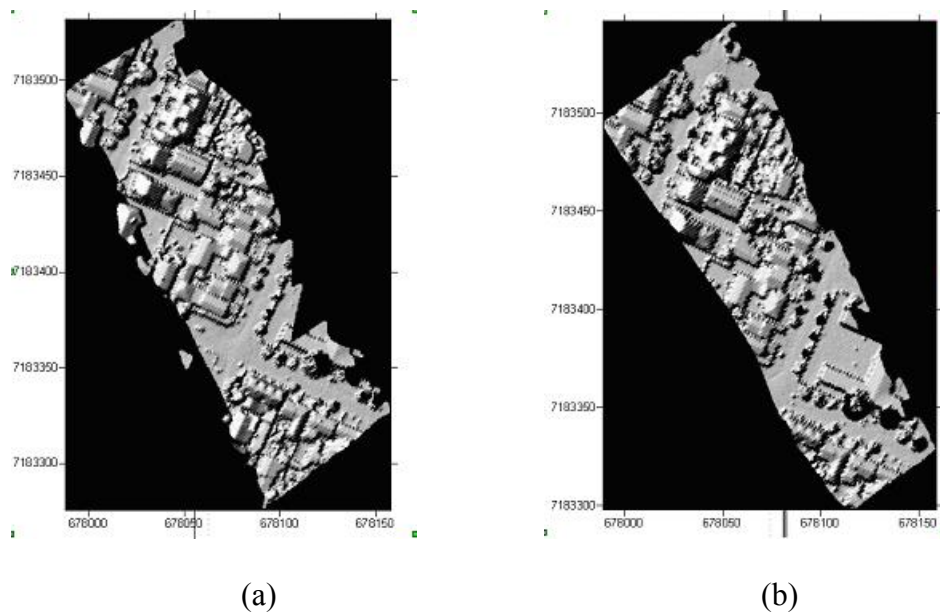


Figure 4-6: Overlapping LIDAR range images over an urban area: first (a) and second surfaces (b).

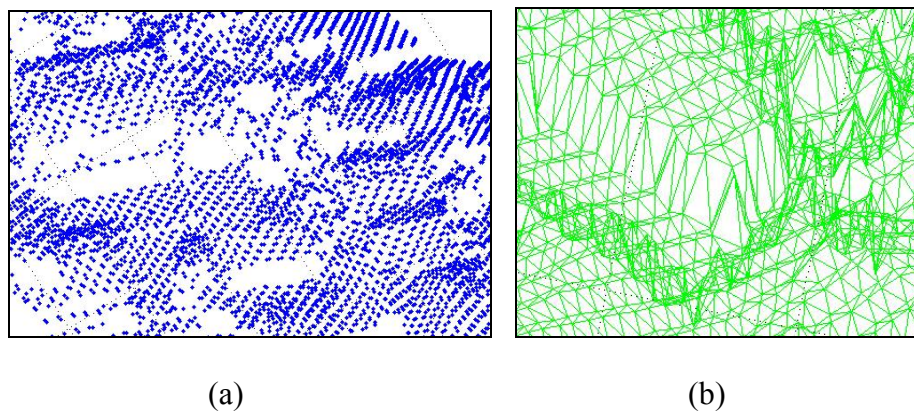


Figure 4-7: Sections of the first LIDAR surface represented by 44,156 points (a) and of the second surface modeled by 45,520 triangular patches (b).

4.4.1.2 Surface Matching Results and Discussion

The registration results with the proposed surface matching algorithm are summarized in Table 4-1. A distance threshold of 0.5 m was used for classifying matched points. This

threshold was chosen by considering the point density and noise levels of the data. Since the two overlapping LIDAR strips were given relative to the same reference frame, WGS84, the transformation parameters (X_T , Y_T , Z_T , ω , φ , κ , S) relating these strips should assume the values of 0 m, 0 m, 0 m, 0° , 0° , 0° , and 1, respectively. However, such values would only be valid if there were no biases present in the data acquisition system. For the MIHT procedure, the cell sizes for the accumulator arrays ranged from 1.0 m to 0.2 m for the translations, 1.0° to 0.5° for the rotations, and 0.10 to 0.01 for the scale factor. The large numbers of points and patches in this experiment required the algorithm approximately 1 day to complete with a 3 GHz Pentium 4 processor (Intel, Santa Clara, CA, USA).

Table 4-1: Initial approximations, expected parameters, estimated transformation parameters, and registration results of the LIDAR data.

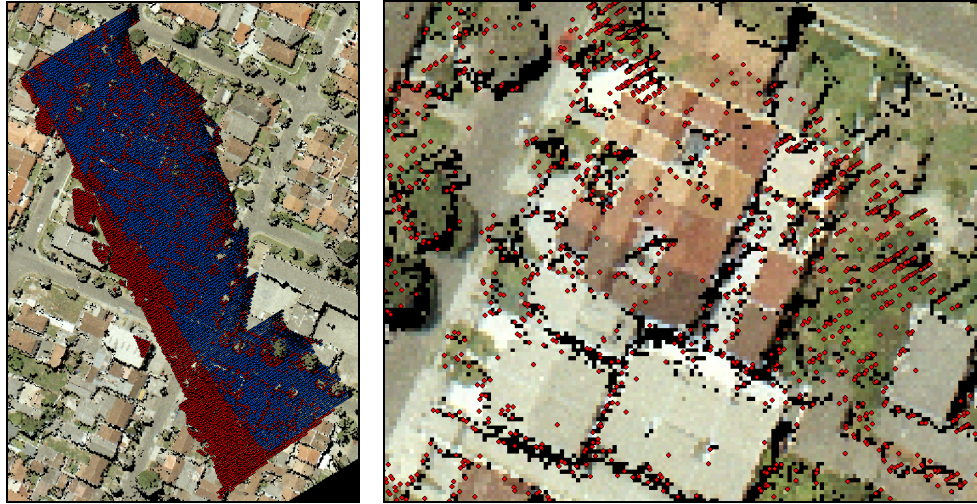
	X_T (m)	Y_T (m)	Z_T (m)	S	ω ($^\circ$)	φ ($^\circ$)	κ ($^\circ$)
Initial Approximations	3.000	-3.000	3.000	0.900	-3.000	3.000	-3.000
Expected Parameters	0.000	0.000	0.000	1.000	0.000	0.000	0.000
Estimated Parameters (\pm Standard Deviation)	-0.660 (1.26e-3)	-0.367 (1.55e-3)	0.007 (2.44e-3)	1.001 (2.20e-5)	-0.017 (6.40e-5)	0.002 (1.14e-4)	0.003 (1.80e-5)
Estimated Variance Component	0.122						
RMS of the Normal Distances	0.142 m						

The initial approximations (Table 4-1) were chosen to be significantly different from the expected values to test the performance of the proposed algorithm. The RMS of the normal distances between the matched point-patch pairs was 0.142 m, which indicated a

successful registration, considering the horizontal (0.5 m) and vertical (0.15 m) accuracies of the involved data. Importantly, rough initial approximations led to accurate estimations of the transformation parameters by the modified algorithm. This strongly demonstrates the ability of the MIHT algorithm to produce good estimates for the ICP algorithm, which in turn produces accurate overall matching results. The deviations of the estimated transformation parameters from the expected values indicated that some biases existed between the two strips. The larger deviations for X_T and Y_T might result from bore-sighting biases between the GPS/INS unit and the laser system. However, these biases were still within the noise level in the data.

Qualitative analysis of the results further verified the accuracy of the registration. The matched (blue) and unmatched (red) points in S_1 were overlaid on top of an ortho-photo, a rectified photographic map, of the target area (Figure 4-8a). A large portion of the overlapped area was classified as matches (blue points, 86%), with a small section of non-overlapping area on the left edge correctly classified as non-matches (red points). Closer investigation of a smaller portion of the unmatched points within the overlap area indicated that they mainly located along building boundaries and around areas with vegetation (e.g., trees) (Figure 4-8b). This observation is reasonable, as physical surface representation using triangular planar patches is not valid at building boundaries where laser points might not land exactly on the edges of the building, so the patches are formed by vertices on the ground and roof tops resulting in slanted building walls (Figure 4-7b). Similarly, in vegetation areas, LIDAR rays can reflect off the treetops or penetrate

through to reach lower levels of vegetation or the ground, thus irregularly shaped triangles are formed that incorrectly model the physical shapes of the surface.



(a)

(b)

Figure 4-8: Matched (blue) and unmatched-points (red) of the first surface (S_1) displayed on an ortho-photo of the target area (a), with the unmatched-points located mainly along edges of the buildings and vegetated areas (b).

To validate the accuracy of the surface matching algorithm for registering LIDAR data, the estimated transformation parameters were compared to ones obtained using manually extracted and identified conjugate linear features from the same dataset (conducted in a parallel study by our research group, Lee et al. (2005)). 164 conjugate lines were extracted from the two LIDAR strips by plane fitting and plane intersections. These features were used in a line-based absolute orientation procedure to solve for the seven transformation parameters relating the strips by minimizing the normal distances between conjugate lines.

A comparison of the estimated transformation parameters from this line-based absolute orientation (Table 4-2) with the results from the surface matching algorithm (Table 4-1) indicates that the transformation parameters from both approaches are similar (average difference of 0.2 m for the translations and 0.007° for the rotations), especially when considering the noise level in the LIDAR data and the preprocessing procedure for the derivation of the linear features. As the values for the estimated parameters were within the noise level (0.5 m horizontal and 0.15 m vertical) when compared to ones derived using linear features, the accuracy of the surface matching algorithm was validated. The larger differences between the X_T and Y_T parameters of the approaches suggested that biases did exist especially in the horizontal directions of the LIDAR data. Although surface registration using linear features can produce accurate results, the surface matching procedure directly works with the raw LIDAR point clouds with minimal preprocessing. Furthermore, for regions/surfaces with a limited number of linear features, the presented approach will be more appropriate.

Table 4-2: Transformation parameters derived from on linear features and surface matching for the LIDAR data.

Registration Method	X_T (m)	Y_T (m)	Z_T (m)	S	ω ($^\circ$)	ϕ ($^\circ$)	κ ($^\circ$)
Linear Features & Absolute Orientation (\pm Standard Deviation)	-0.418 (2.98e-2)	-0.209 (2.79e-2)	-0.019 (7.87e-2)	1.000 (2.30e-5)	-0.010 (2.29e-2)	0.017 (3.78e-2)	0.003 (1.30e-3)
Surface Matching (\pm Standard Deviation)	-0.660 (1.26e-3)	-0.367 (1.55e-3)	0.007 (2.44e-3)	1.001 (2.20e-5)	-0.017 (6.40e-5)	0.002 (1.14e-4)	0.003 (1.80e-5)

This study demonstrated that the surface matching algorithm can handle high density data and results were validated with ones derived from manually identified linear features. The algorithm can also be used for quality control of the LIDAR data as the presence of biases was identified.

4.4.2 Stereophotogrammetry for Facial Measurements

Measurements and modeling of human facial features can be found in many fields such as medical applications, person identification and surveillance, and virtual reality applications (D'Apuzzo, 2002). The main objective of these applications is to verify an individual based on their unique facial geometry. Many techniques are available in these fields to acquire facial data, such as laser scanning, video tracking, and photogrammetry. Some of these techniques require expensive and complex equipment, and extensive data-processing procedures. Therefore, low-cost digital cameras can be used in a photogrammetric procedure as a cost-effective approach to provide accurate and reliable facial measurements (Pullivelli, 2005). Low-cost digital cameras, when properly calibrated, can capture stereo 2D images of facial features to accurately reconstruct a 3D human face. This section presents the results of matching facial models obtained based on digital stereophotogrammetry using the modified surface matching algorithm.

4.4.2.1 Data and Experiments

Two Canon EOS Digital Rebel XT cameras (Canon U.S.A., Inc., Lake Success, NY) were used in this experiment to capture stereo-images of facial features (eight mega pixels, pixel size of 6.5 micrometers). The two cameras were mounted approximately 1.5 m apart on a rigid metal frame (Figure 4-9). The subjects were also positioned approximately 1.5 m from the cameras. Both cameras were controlled by a remote control, so that the stereo-images could be taken at the exact same time. This approach is particularly beneficial for facial measurements to eliminate potential movements between the two images. A regularly spaced grid was projected onto the subject to allow identification of conjugate features (i.e., grid points) (Figure 4-10). The 2D image coordinates of these conjugate points were measured on both images using a customized software written in Visual C++ (Microsoft Corporation, Redmond, WA, version 6.0). Through a bundle adjustment algorithm along with camera parameters obtained from proper calibration procedures (e.g., Habib and Morgan, 2003a), the 3D object space coordinates of the grid points were derived to model the face. To increase the density of these surface points, the Thin Plate Spline (TPS) algorithm (Boyd et al., 1999) was used to model the surface and re-sample the points (point density of 2 mm, no smoothing was applied) (Figure 4-11). With a limited number of points measured on the face, details of some facial features (e.g., details of the eyes) were not fully captured and modeled.



Figure 4-9: Two Canon digital cameras mounted on a rigid frame for capturing stereo-images of the face.

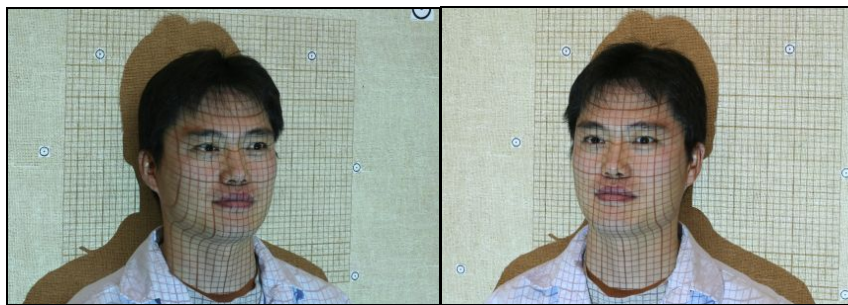


Figure 4-10: Left and right stereo-images of a subject's face, with projected grid points to allow identification of conjugate features.

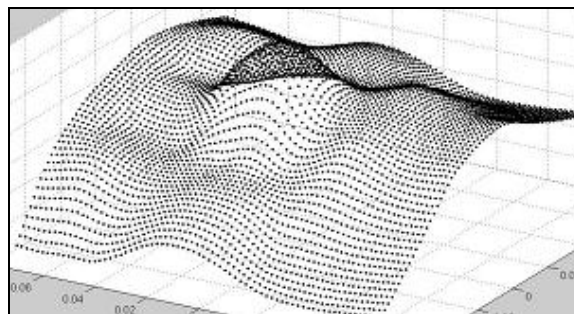


Figure 4-11: Surface model of a human's face generated by the TPS algorithm.

Three male volunteers were used for this study. Table 4-3 and Figure 4-12 present the datasets involved for the experiments. Three experiments were performed to 1) verify that the surface matching algorithm could match temporal datasets and recognize facial models of the same individual, 2) test if the algorithm could detect differences between different facial expressions of the same individual, and 3) identify discrepancies when matching facial surfaces of two individuals. Both quantitative (i.e., RMS distance and percentage of matches) and qualitative (i.e., visualization of the matching results) measures were analyzed for each experiment to determine if the surface matching algorithm was successful in achieving the objectives of the experiments. These were preliminary experiments to verify that the surface matching algorithm can be used to match facial models. To truly quantify the accuracies of the algorithm for facial recognition applications, further investigations with more subjects are needed.

Table 4-3: Involved facial datasets for the three registration experiments performed.

Experiments	Dataset 1	Dataset 2	Objective
1	Subject 1 Time 1 2790 patches	Subject 1 Time 2 6016 points	To test the ability of the algorithm for registering temporal datasets and recognize faces
2	Subject 1 Not Smiling 2790 patches	Subject 1 Smiling 6111 points	To test the ability of the algorithm for detecting changes
3	Subject 2 2100 patches	Subject 3 5922 points	To test the ability of the algorithm to identify different people based on results

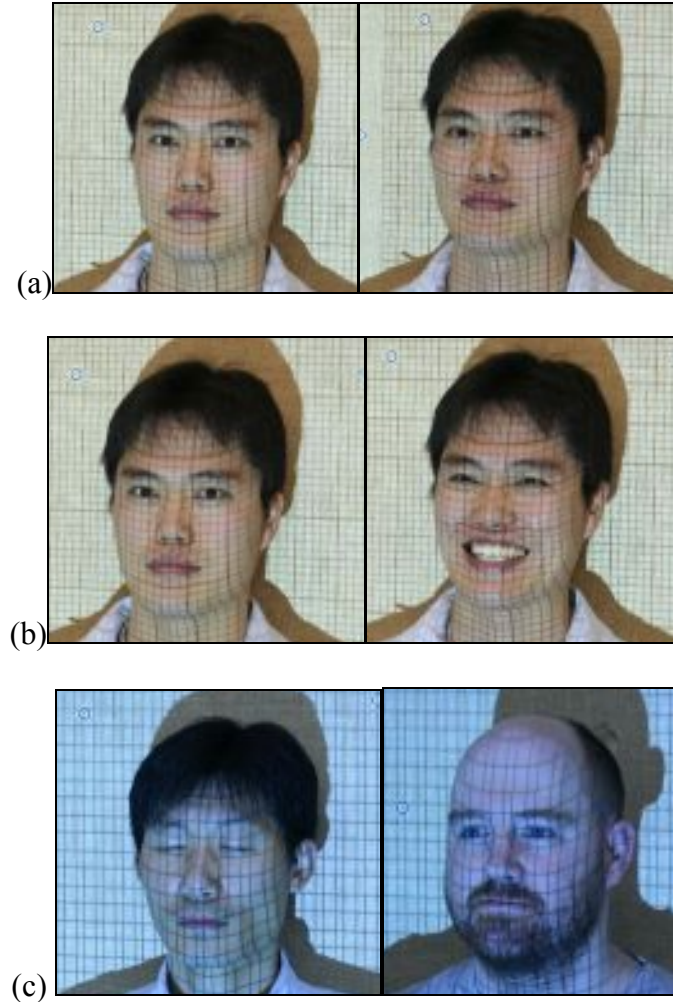


Figure 4-12: Facial images used in the three experiments (two time points (a), non-smiling versus smiling (b), and two different subjects (c)).

4.4.2.2 Surface Matching Results and Discussion

A distance threshold of 2.5 mm was used as the matching criteria for the three experiments. The accumulator array cell sizes ranged from 8 cm to 5 mm for the translations and 2° to $2/3^\circ$ for the rotations. The scale factor was fixed at one as no scale differences were assumed between two facial models. Each experiment required the

algorithm less than two hours to run on a 3 GHz Pentium 4 processor (Intel, Santa Clara, CA, USA).

The first experiment registered two temporal face models from the same subject, and the resulting RMS distance was 0.705 mm. This indicated a high quality of fit when matching temporal datasets that were captured under similar conditions. A large percentage of the points were classified as matches (88%) with the non-matches mainly located around the edges of the surfaces resulting from different surface modeling behaviour of TPS (Figure 4-13). This experiment shows that the algorithm can recognize facial models of the same person when matching datasets collected at different times. The images acquired for these datasets (Figure 4-12a) suggested that there might be some changes with the eyes and surrounding areas. Since the details of these features were not fully captured by the facial models, these differences were not detected by the algorithm.

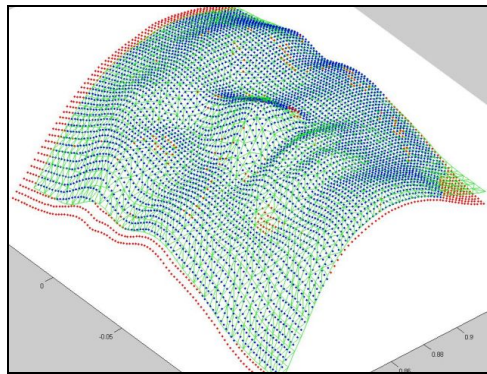


Figure 4-13: Co-registered face models of subject 1 with the green mesh representing the model from the first time point and the points (blue: matches, red: non-matches) representing the second time point.

For the second experiment, the algorithm successfully registered the two face models with a RMS distance of 1.18 mm and 60% of the points were classified as matches. Qualitative analysis of the results indicated that the algorithm identified non-matching points in the areas of the mouth and the cheeks of the subject as expected when a person is smiling (Figure 4-14a). The nose and the forehead of the subject were nicely aligned between the two models. To further confirm these analyses, the non-matches were projected onto the original image of the first subject (Figure 4-14b), which verified that the unmatched points belonged to the mouth and cheeks areas. These results demonstrated that the algorithm can register face models with different facial expressions, and can correctly identify the differences between them.

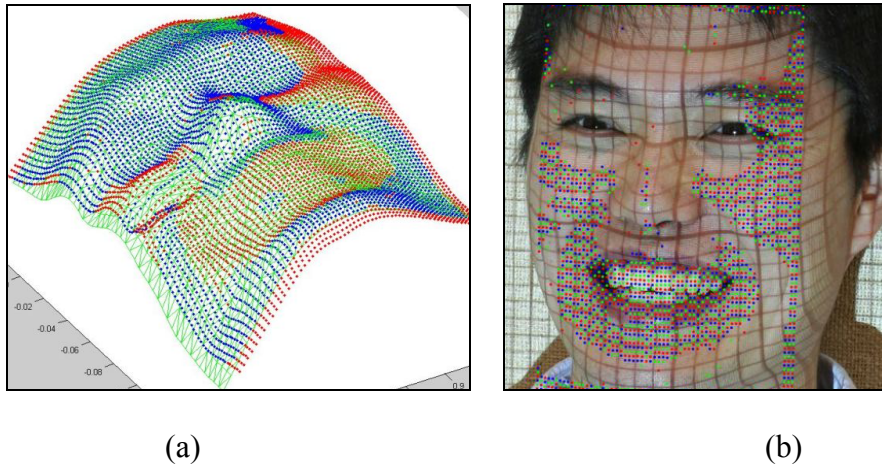


Figure 4-14: Co-registered face models of subject 1 with the green mesh representing the non-smiling face and the blue (matched) and red (unmatched) points representing the smiling face (a); unmatched points projected onto the original image (b).

The third experiment registered facial models of two different people to test whether the algorithm could detect differences in facial features. Although the RMS distance of 2.12

mm indicated well fitted surfaces, qualitative investigation showed that a large percentage of the points (48%) were not matching (Figure 4-15). This was likely because the algorithm would attempt to align the surfaces as well as possible (e.g., align distinct features like the nose) resulting in a small RMS distance between the matched points. Therefore, these results indicated that it is important to not only evaluate the RMS distance, but to also investigate other parameters (e.g., percentage of matches) and analyze the qualitative results. It is clearly shown by Figure 4-15 that the surfaces were generated from two different people and that one subject had a larger forehead (unmatched points) than the other.

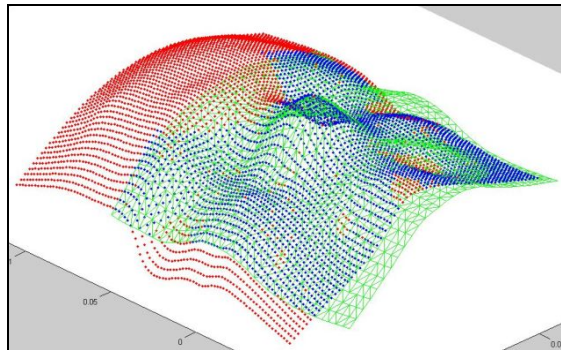


Figure 4-15: Co-registered face models of two different subjects with clear indications of different facial features by the non-matches (red points).

4.4.3 Close-range Laser Scanning of Small Object

The Spin-Image surface alignment technique (reviewed in section 2.5.2.3) utilized a unique idea of matching Spin-Images to identify conjugate points between two overlapping laser point clouds (Guarnieri et al., 2005). By establishing the correspondence, the transformation can be solved to align the laser scanning views as an

initial step to generate a 3D model. The technique was tested with close-range laser scanning data of a rubber cat object (size: 25 cm × 20 cm × 10 cm). A maximum error of 1.45 mm was found for the Spin-Image technique. With the incorporation of the ICP algorithm, the error reduced to 0.87 mm (Guarnieri et al., 2005), an excellent result given the object size. This application shows the comparison between the Spin-Image technique and the proposed surface matching algorithm by applying it to the rubber cat dataset.

4.4.3.1 Data and Experiments

Two laser scan views of a rubber cat object (size: 25 cm × 20 cm × 10 cm, Figure 4-16) were acquired by a ShapeGrabber 100 laser scanner (ShapeGrabber Inc., Ottawa, Canada). The laser precision was 50 μm and the point spacing for the acquired point cloud was approximately 1 mm, resulting in a high density data. A 2 mm point spacing (every second point) was used for surface modeling to reduce the point density. The separate coordinate system of each laser scan view was given with respect to the origin of the scanner unit. One of the scans was further processed to form triangular patches using Delaunay triangulation. The rubber cat surfaces were registered with the surface matching algorithm based on MIHT/ICP and results were compared to the Spin-Image technique. Specifically, the transformation parameters, the RMS distance, the percentage of matches, and the process time were compared between the two approaches. If the

difference between the RMS distances of the two techniques was within the noise level of the data, then it indicated that the two methods produced comparable matching results.

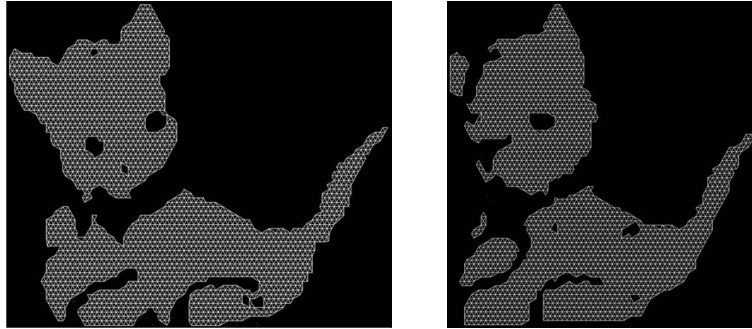


Figure 4-16: Two views of a rubber cat object acquired by a close-range laser scanner.

4.4.3.2 Surface Matching Results and Discussion

The surface matching algorithm took 5 hrs 11 min to process with a 3 GHz Pentium 4 processor (Intel, Santa Clara, CA, USA). The accumulator array cell sizes set at 2 mm to 1 mm for the translations and 2° to $5/6^\circ$ for the rotations. Scale factor was fixed at one. The algorithm aligned the two views together with a RMS distance of 0.203 mm, based on a distance threshold of 0.6 mm. The estimated transformation parameters and quality of fit of the surfaces were compared to the ones derived using the Spin-Image technique, as summarized in Table 4-4 (Figure 4-17). The transformation parameters and distances were similar between the two methods, with an average difference of 0.33 mm for the translation parameters and 0.18° for the rotations. The proposed surface matching technique also resulted in a larger percentage of matches (difference of 2.7%) and a slightly smaller RMS distance (difference of 0.091 mm). This difference of 90 μm was around noise level of the data, thus indicated that both surface matching techniques

produced similar results. However, the surface matching technique required up to half the processing time of the Spin-Image technique.

Table 4-4: Comparisons of the registration results between the proposed surface matching algorithm and the Spin-Image technique.

Parameters	Proposed Algorithm	Spin-Image Technique	Difference
X_T (mm)	-0.125	0.188	-0.313
Y_T (mm)	9.465	9.182	0.284
Z_T (mm)	9.603	9.992	-0.389
ω ($^\circ$)	-30.854	-30.947	0.093
φ ($^\circ$)	-1.017	-0.918	-0.099
κ ($^\circ$)	0.320	-0.018	0.338
% of Matches	70.5%	67.8%	2.7%
RMS Distance (mm)	0.203	0.294	-0.091

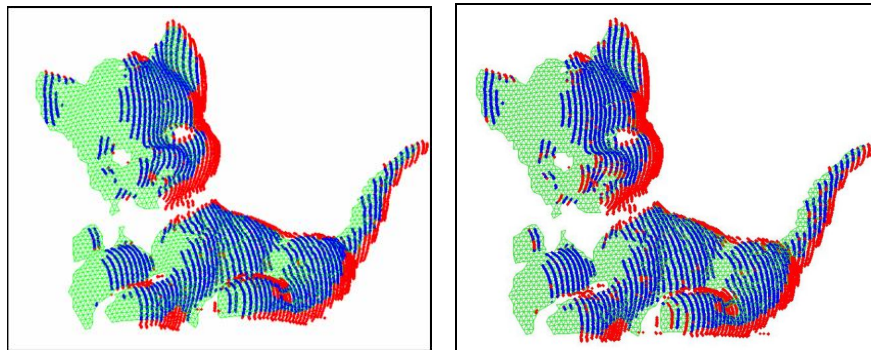


Figure 4-17: Co-registered laser scanning views with the proposed surface matching algorithm (a) and with the Spin-Image technique (b) (green mesh represents the reference scan, blue points are the matches and red points are the non-matches for the second scan).

This application shows that the proposed surface matching algorithm can produce accurate results by comparison with a different technique of similar accuracy. The results also indicate that it can be successfully applied to align high density laser scanning views for 3D model generations.

4.5 Summary

This chapter describes the modification of the proposed surface matching algorithm with the incorporation of the Iterative Closest Point algorithm to complement the modified iterated Hough transform approach. Experimental results from the three Geomatics applications verified that the modified algorithm can successfully register high density 3D data acquired by remote sensing systems. The first application showed that the algorithm can be used to identify existing biases between overlapping LIDAR strips for quality control purposes. The algorithm could also detect changes between facial models for person recognition. The third application showed improvement of the proposed algorithm over an existing technique for matching laser scanning views. Overall, these successful applications indicate that the algorithm has strong potential to function well with non-uniform applications such as those associated with anatomical joint structures generated from high density 3D MR data.

Chapter Five: Registration of 3D MR Data

5.1 Introduction

The suitability of the proposed surface matching algorithm for registration with anatomical joint structures is explored in this chapter for the second specific aim of this research. The data, image processing procedures, and results of registration of knee joint surfaces generated from MRI with the proposed surface matching algorithm are presented. These experiments aimed to verify whether the proposed algorithm can be used to align with acceptable accuracy 3D MR datasets acquired under different conditions.

5.2 Data Acquisition and Descriptions

This data was collected in collaboration with a parallel study of PFPS using MRI (Connolly, 2005). Ethics approval was obtained for this study from the Conjoint Health Research Ethics Board, University of Calgary, for performing health research on human subjects (Appendix A). Written informed consent (Appendix B) was also obtained from each subject prior to imaging. The dataset was acquired with a 3-telsa MRI unit (General Electric Medical Systems, Waukesha, Wisconsin, USA) located at the Seaman Family MR Research Centre, Foothills Medical Centre, Calgary, Canada (Figure 5-1). All imaging sessions were operated by trained MR technologists.

A general purpose flex coil was used for imaging to enhance the image quality. This coil could be positioned in close proximity to the knee without interfering with knee positions. It helped to reduce the noise captured (i.e., increase SNR) and improve tissue contrast (Figure 5-1). One subject (Subject 1, age 25 years) with a healthy knee condition (no knee pain or injury one year prior to study) was imaged at 0° and 30° flexion angles (Figure 5-2). Four additional female subjects (Subject 2-5, age 26.3 ± 4.6 years) with healthy knees conditions were imaged at 0°, 15°, 30°, and 45° flexion angles. A balanced steady-state free precession (SSFP) sequence was chosen for all the subjects. Imaging parameters were selected in a pilot study by a radiologist to maximize the contrast between tissues in the knee joint (e.g., cartilage, synovial fluid, and bone) while maintaining a short scan time. At 0° flexion, the parameters set for the sequence were TR = 7 ms, TE = 2 ms, and flip angle = 40°. Thirty-six contiguous sagittal images were acquired with an in-plane resolution (i.e., image pixel size) of 0.625 mm (FOV = 16 cm × 16 cm, 256 × 256 matrix) and 3.0 mm across-slice resolution (i.e., slice thickness), with a total scan time of approximately 1 min 55 sec (Figure 5-3a). At higher flexion angles (15°, 30°, and 45°), the knees were under physiological loading conditions, using a custom design loading apparatus (Ronsky, 1994) with the subjects pushing on a foot pedal and holding at approximately 12% of the maximum force they could apply (Figure 5-1). The imaging parameters were set at TR = 17 ms, TE = 3 ms, and flip angle = 90°, resulting in a scan time of 2 min 17 sec. Sagittal images were also acquired with an image resolution of 0.625 mm × 0.625 mm × 3.000 mm (FOV = 16 cm × 16 cm, 256 × 256 matrix) (Figure 5-3b).



Figure 5-1: Subject imaged with the 3-telsa MRI unit and a flex coil at the Seaman Family MR Research Centre, Calgary.

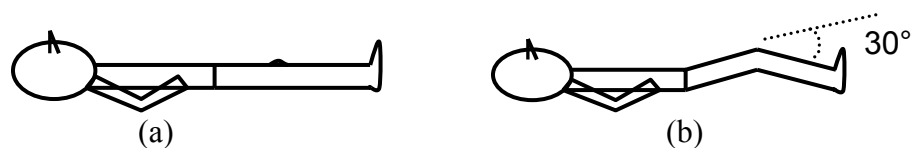


Figure 5-2: Subject positioned at 0° knee flexion (full extension) (a) and 30° knee flexion (b).

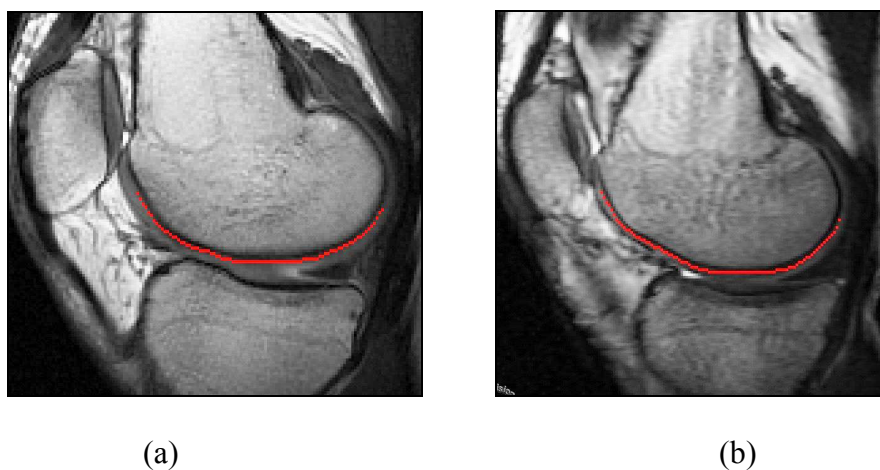


Figure 5-3: MR images (sagittal balanced SSFP sequence) of a healthy knee at full extension (a) and with the knee at 30° flexion under loading condition (b). The red lines were the manually digitized points for the femoral bone-cartilage interfaces.

5.3 Feature Segmentation

To perform surface matching with the proposed algorithm, surfaces of interest, such as the bone-cartilage interface of the femur, were digitized from the MR images. Digitization was performed manually for each image slice using the commercial software SliceOmatic (TomoVision, Montreal, Canada), that has been successfully employed by our research group (e.g. Connelly, 2005). Although semi- and automatic segmentation techniques could potentially reduce the processing time for the digitization, Sobel and Non-Maxima Suppression edge detection algorithms were tested on this dataset and did not produce satisfying results. Since intensity values between bone, cartilage, and fluid were similar, false edges were detected and intensive editing was required after automatic segmentation. The optimal segmentation approach was not investigated as it was not the focus of this thesis research. Therefore, manual digitization using SliceOmatic was performed.

For each subject, femoral condyle surfaces (bone-cartilage interface) were digitized (Figure 5-3). Digitization criterion was based on selecting the pixels between the cortical bone (dark grey) and cartilage (light grey). The manual digitization process produced contours formed by points with 3D coordinates (Figure 5-4). In addition, digitized points for the patellar bone and cartilage surfaces, as well as femoral bone and cartilage of the patellofemoral articulating area were obtained from a parallel study for the same datasets at the higher flexion angles (Figure 5-5) (Connolly, 2005).

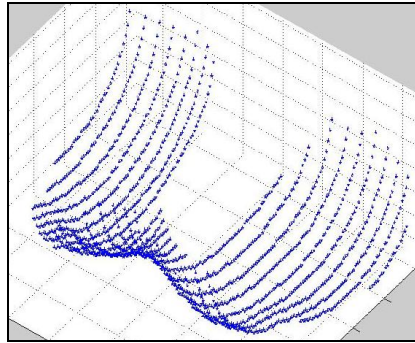


Figure 5-4: Contours of the femoral condyle surface formed by digitized points of the MR image slice.

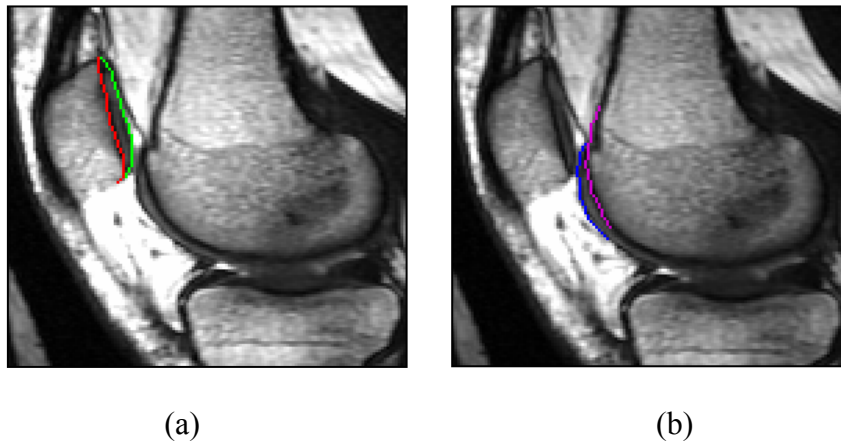


Figure 5-5: Digitized bone (red for patella, purple for femur) and cartilage (green for patella, blue for femur) surfaces of the articulating area of the patellofemoral joint (Connolly, 2005).

5.4 Surface Modeling

The across slice resolution was significantly worse than the image resolution with the optimized imaging sequences. To produce more evenly distributed surface point clouds, the TPS algorithm (Boyd et al., 1999) was applied to the digitized surface contours to densify the point clouds and resample the surface. Since TPS could not model a surface

with the same XY coordinates but different Z coordinates, only the distal ends with mainly the anterior portions of the femoral condyles and groves were manually digitized and modeled for the registration. For the femurs, a re-sampling interval of 1.0 mm was used to balance out the in-plane and across-slice resolution. A smaller sampling interval could be used but this would result in a large number of surface points thus increase the run times of both the TPS and the surface matching algorithm. For the smoothing factor, the effects of the amount of smoothing were investigated in a previous study (Moss, 2001) for the femoral and patellar surfaces of porcine specimens with MRI. No significant differences were found for smoothing factors ranging from 0.25 to 1.45. A smoothing factor of 0.6 was chosen for the relatively smooth surface of the femur (Figure 5-6a). For the rougher patellar surfaces, a smoothing factor of 0.275 was used with the sampling interval also set at 1.0 mm (Figure 5-6b). No investigations on the smoothing factor were performed here as it was beyond the scope of this thesis research.

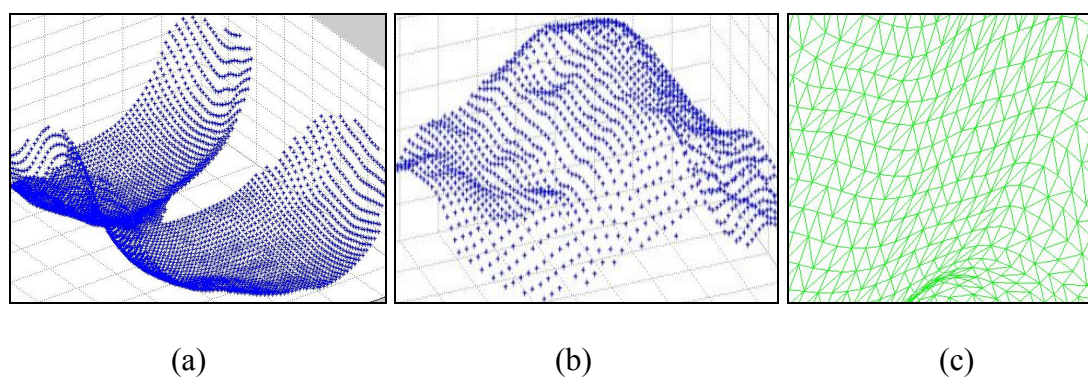


Figure 5-6: Femoral (a) and patellar surface (b) resampled and modeled by TPS (figures are not to scale), and a section of the triangular patches formed by Delaunay triangulation using the resampled points (c).

Since the proposed algorithm requires the reference surface to be modeled as a triangular mesh, the point clouds were further processed using Delaunay triangulation in MATLAB (The Mathworks, Inc., Natick, MA, version 6.5) to generate triangular patches (Figure 5-6c).

5.5 Registration Experiments

The main objective of the registration experiments with the femoral and patellar surfaces was to verify whether the surface matching algorithm, based on MIHT/ICP, can be used to successfully align high density 3D MR datasets. The capability of the algorithm to match identical surfaces (i.e., surface generated from the same digitization of one scan) was initially evaluated to ensure no errors were introduced to the results by the registration algorithm. Experiments were also performed on different bone structures (i.e., femur and patella) to test if the algorithm could successfully register joint surfaces that were captured at different positions and under different conditions. The results from these experiments would verify whether the algorithm could be applied in MR applications to study joint biomechanics and health statuses. Also, the effect of different surface geometry (i.e., femur versus patella) on the matching results would be analyzed. Quantitative measures derived from the surface matching algorithm (e.g., RMS distance and percentage of matches) and qualitative results (e.g., 3D visualization and image mosaics of the matching results) were analyzed for each of the experiments to determine if the registrations were successful.

The capability of the surface matching algorithm to match identical surfaces was evaluated with datasets of Subject 1. Registration was performed between two identical surfaces at the 0° flexion, and also for two surfaces at 30° . The two surfaces for each flexion (one modeled by points and the other by patches) were generated from the same set of digitized points with the same TPS re-sampling and smoothing parameters. For the registrations, the distance threshold was set at 0.4 mm for the matching criterion. The accumulator array cell sizes were set to range from 0.8 mm to 0.5 mm for the translations, 1° to $\frac{1}{2}^\circ$ for the rotations, and 0.1 to 0.01 for the scale factor. Since the surfaces were generated from the same digitization of the same set of scans, the true parameters were zeros for the translations and rotations, and one for the scale factor. Rough initial parameter approximations were set (-4.5 mm, 4.5 mm, -4.5 mm, 4.5° , -4.5° , 4.5° , and 0.9 for X_T , Y_T , Z_T , ω , φ , κ , and S respectively) to test whether the algorithm could still derive the correct parameters. In addition, the identical surfaces should be fitted perfectly with each other after the registration, thus the estimated variance component and RMS distance should be zeros. These two measures would be evaluated to check whether the surfaces did indeed achieve a perfect fit.

For the other four subjects, nineteen registrations were performed between different flexion angles for both the femoral and patellar surfaces (Table 5-1). These bone surfaces were assumed to remain rigid at the different flexions. This was a valid assumption for bone surfaces of healthy subjects over the imaging session (approximately 1 hour), thus the 3D similarity transformation should be sufficient to align the surfaces.

Although digitization may introduce some local changes/errors along the bone surfaces, these changes would be isolated by the proposed algorithm as non-matches and would not be included in the least squares adjustment for the transformation parameters.

Table 5-1: Registration experiments performed for Subject 2 to Subject 5.

Subject	Experiments	Surface	Surface Parameters			
			Surface 1 - Points		Surface 2 – Patches (reference)	
			Flexion (°)	#	Flexion (°)	#
S2	1	Femur	15	4150	0	7456
	2	Femur	30	4107	0	7456
	3	Femur	45	4236	0	7456
	4	Patella	30	1694	15	3238
	5	Patella	45	1829	15	3238
S3	6	Femur	15	3996	0	7456
	7	Femur	30	4145	0	7456
	8	Femur	45	4282	0	7456
	9	Patella	30	1754	15	3394
	10	Patella	45	1789	15	3394
S4	11	Femur	15	3585	0	6540
	12	Femur	30	3690	0	6540
	13	Femur	45	3643	0	6540
	14	Patella	30	1407	15	2807
	15	Patella	45	1485	15	2807
S5	16	Femur	30	3991	15	7954
	17	Femur	45	4202	15	7954
	18	Patella	30	1512	15	2881
	19	Patella	45	1584	15	2881

For the registrations, the scale factor was set at one and was not solved for as MRI, when properly calibrated, captures true scale of objects. Although this was a reasonable assumption, investigations should be performed in the future to confirm if it is valid. The distance threshold was set at 0.4 mm for the matching criterion. The accumulator array

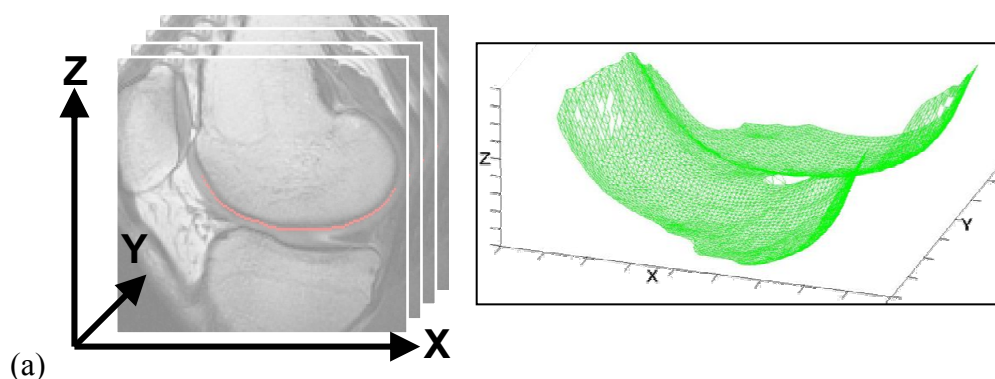
cell sizes ranged from 0.8 mm to 0.3 mm for the translation parameters and 1° to $\frac{1}{2}^\circ$ for the rotations. Images at 0° flexion were not available for Subject 5, so the femur at 15° was used as the reference surface for the registration.

The RMS distance and percentage of matches from each experiment would be evaluated to determine whether the algorithm could successfully register the surfaces. To indicate successful registration, the quality of fit of the surfaces (i.e., the RMS distance) should be around the noise level of the data (i.e., about the size of the MR image pixel: 0.6 mm). For each subject, the MR scans were captured in one imaging session (less than 2 hours), thus a large percentage of the points should be classified as matches. These percentages were evaluated and 3D visualizations of the matches and non-matches would also be performed. Since only a portion of the femoral condyles and groves were used for the femur registrations, it was important to evaluate whether this was sufficient to produce a good alignment of the whole femur. This evaluation was achieved by generating an image mosaic of the two datasets (i.e., superimposition of corresponding image slices). To generate an image mosaic, the image slices from the first surface were transformed with the estimated transformation parameters. The transformed images were then re-sampled based on a nearest neighbour approach (i.e., each re-sampled image voxel was assigned a grey level of its nearest voxel from the transformed image). After this procedure, the transformed images fell onto the same planes as the reference image slices, and corresponding images were superimposed. The alignment of the entire femoral surface could then be directly visualized on the image mosaics.

Although the coordinate systems were uniquely defined for each set of images, they shared similar orientations for the femur (Figure 5-7a), and also for the patella (Figure 5-7b). Table 5-2 provides the definitions of the directional terms for anatomy. The coordinate axes were modified from the original MR coordinate systems so they were compatible for the TPS algorithm. The femur and the patella were defined by different coordinate systems because of the different physical orientation of the surfaces. As a rule of thumb with TPS modeling, the surfaces lie on the XY plane with the height/topographical variations defined along the Z axis. This is because the TPS algorithm describes the Z coordinate of the surface as a function of X and Y (refer to section 2.4). For both surfaces, the Y axis lied along the image slice direction.

Table 5-2: Directional terms for the human body (Van De Graaff and Fox, 1989).

Term	Definition	Example
Anterior	Toward the front	The navel is on the anterior side of the body
Posterior	Toward the back	The kidneys are posterior to the intestine
Medial	Toward the midline of the body	The heart is medial to the lungs
Lateral	Toward the side of the body	The ears are on the lateral sides of the head
Proximal	Toward the main mass of the body	The knee is proximal to the foot
Distal	Away from the main mass of the body	The hand is distal to the elbow



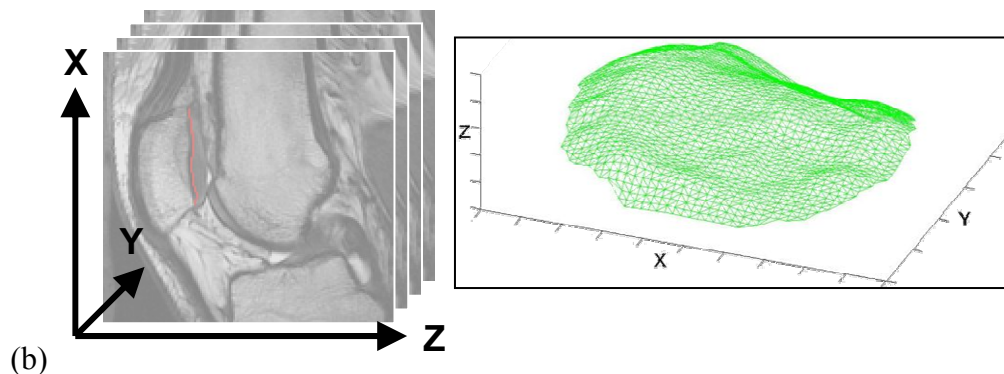


Figure 5-7: Coordinate system for the femur (X: Posterior (+) – Anterior (-), Y: Medial (+) – Lateral (-), Z: Proximal (+) – distal (-)) (a) and for the patella (X: Proximal (+) – Distal (-), Y: Medial (+) – Lateral (-), Z: Posterior (+) – Anterior (-)) (b).

5.6 Results and Discussion

For the registrations between the identical 0° and 30° surfaces for Subject 1, the estimated transformation parameters were zero translations, zero rotations, and scale of one. These results showed that the algorithm correctly estimated the transformation parameters with rough initial parameter approximations. The estimated variances and RMS distances were also zeros for both experiments, which indicated perfectly fitted surfaces. These results confirmed that the surface matching algorithm can accurately register identical surfaces without introducing any errors.

Table 5-3 summarizes the experiments performed on the four subjects and the registration results. The estimated transformation parameters are not reported here as the true values were unknown for these cases and no comparisons were made. The average RMS distance was 0.217 ± 0.035 mm (mean \pm standard deviation (SD)) for the femur and

0.207 ± 0.008 mm for the patella. These values were less than the size of an image pixel (0.625 mm) which indicated a high quality of fit of the surfaces. The average percentages of matches were 63% for the femur and 61% for the patella.

Table 5-3: Registration results for the femoral and patellar surfaces of the four subjects.

Subject	Exp.	Surface	Surface Parameters		Variance	RMS Dist. (mm)	% of Matches	Run Time
			Points	Patches				
			Flexion (°)	Flexion (°)				
S2	1	Femur	15	0	0.060	0.211	62%	4 hr 8 min
	2	Femur	30	0	0.053	0.197	66%	5 hr 28 min
	3	Femur	45	0	0.051	0.203	50%	5 hr 22 min
	4	Patella	30	15	0.040	0.212	54%	38 min
	5	Patella	45	15	0.037	0.202	60%	54 min
S3	6	Femur	15	0	0.068	0.214	49%	3 hr 47 min
	7	Femur	30	0	0.050	0.206	60%	4 hr
	8	Femur	45	0	0.089	0.278	69%	5 hr 34 min
	9	Patella	30	15	0.038	0.209	57%	54 min
	10	Patella	45	15	0.034	0.199	65%	52 min
S4	11	Femur	15	0	0.064	0.204	52%	3 hr
	12	Femur	30	0	0.063	0.209	60%	3 hr 8 min
	13	Femur	45	0	0.124	0.292	64%	5 hr 6 min
	14	Patella	30	15	0.035	0.198	67%	35 min
	15	Patella	45	15	0.037	0.202	58%	36 min
S5	16	Femur	30	15	0.050	0.179	83%	4 hr
	17	Femur	45	15	0.067	0.195	77%	4 hr 47 min
	18	Patella	30	15	0.036	0.203	67%	34 min
	19	Patella	45	15	0.044	0.226	63%	42 min

Registrations with the patella produced smaller estimated variance components and RMS distances than the femur. These results are speculated to be attributed to the more unique geometry formed by the facets and the ridges of the patellar surfaces (Figure 5-8a). These surface features helped to align the patellar surfaces resulting in better qualities of fit than that of the femoral condyles, which are relatively smoothed surfaces with

minimal variations in topography (Figure 5-8b). For the transformation parameters, comparisons between the standard deviations of the translation parameters indicated that Z_T was the most precisely estimated. This was likely because the majority of the surface patches were normal to the Z -axis (refer to Figure 5-7) and thus provided a good geometry for the estimation of Z_T . The femur registrations required the algorithm 3 to 5.5 hours to process with a 3 GHz Pentium 4 processor (Intel, Santa Clara, CA, USA) and the patella registrations required less than 1 hour to process.

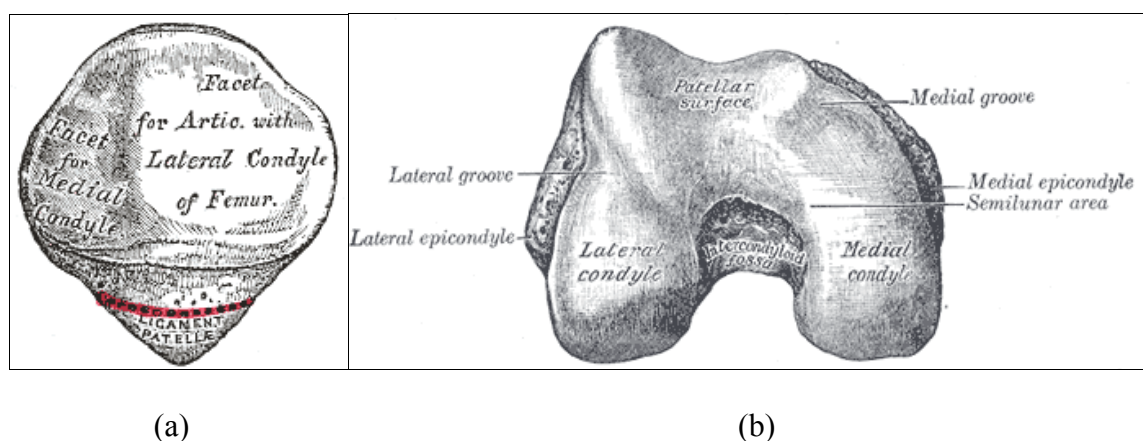


Figure 5-8: Patellar (a) and femoral condyle (b) surfaces (Gray's Anatomy of the Human Body, 2006).

Qualitative assessments of the matching results also confirmed the correctness of the registrations (Figure 5-9). The unmatched points (red) identified on the femoral surfaces were most likely attributable to small errors introduced during the manual digitization and also different behaviours of TPS for the surface modeling. The image mosaics revealed that even though only a small portion of the femur was used for the registration,

corresponding features from other areas of the femur were also well-aligned (Figure 5-10). The qualitative analyses along with the quantitative results discussed previously showed that the surface matching algorithm could register surfaces generated from high density MR data. Digitization errors were also detected thus did not affect the quality of the registration. Although the registration results were satisfactory, the use of TPS for surface modeling has limited the registration to use only a small portion of the femur in this research. If the entire surface is used, the geometry will be improved, thus can potentially improve the accuracy of the registration and increase the number of matching points. The ways to implement these suggestions will be addressed in Chapter Eight as part of the future work for this research.

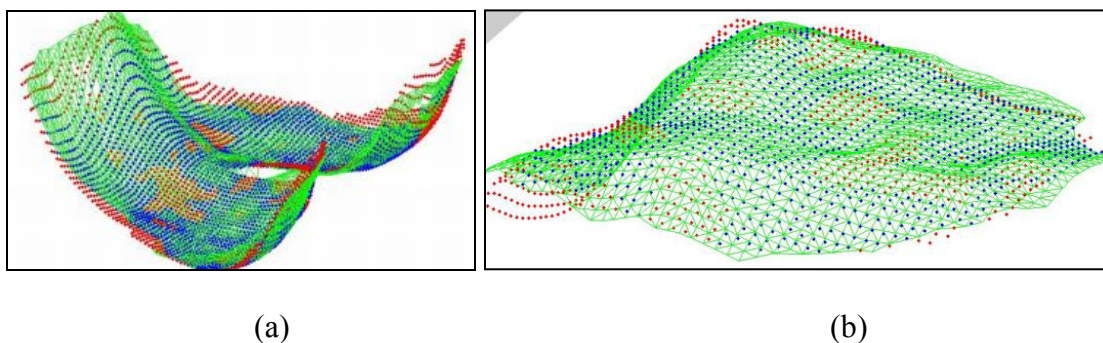


Figure 5-9: Registered femoral surfaces (30° with 0°) (a) and patellar surfaces (30° with 15°) (b) for subject 2, with the green mesh representing the reference surface, and blue points representing the matches and red points the non-matches from the transformed surface (figures are not to scale).



Figure 5-10: Mosaics showing a good match of the femur between the reference image (background: 0°) and its corresponding image from the second dataset (foreground/small windows: 30°).

Since only one bone surface was used for each registration, the other knee joint structures would not be aligned. Figure 5-11 shows the mosaics generated for the registration of a femur from 30° flexion to 0° flexion. Clearly, the tibia and the patella were in different positions. This is expected for different flexion angles and subject re-positioning between the two scans. These observations suggest that the proposed surface matching algorithm can be applied in studies of joint biomechanics, where the movements of joint surfaces (e.g., patella) at different positions and conditions can be quantified after the registration of one (or more) reference surface (e.g., femur). The image mosaics can also help to visualize how these joint structures change in positions.



Figure 5-11: Mosaics showing a good match of the femur but different positions for the tibia and the patella due to the different knee flexion angles (background: 0° and foreground 30°).

5.7 Summary

The surface matching algorithm correctly registered identical surfaces (one set of scans with one digitization) even with rough initial approximations for the parameters. The estimated transformation parameters equalled to the known values, and the surfaces were perfectly fitted together (RMS distances of 0 mm). Femoral and patellar surfaces at different positions (i.e., flexion angles) and conditions (i.e., loading) were also successfully registered for the four subjects. Results indicated high quality of fit of the surfaces (RMS distances equalled approximately $1/3$ of a pixel size). Patellar surfaces have unique geometry formed by multi-oriented facets and ridges thus provided better quality of fit than the smooth femoral surfaces. Qualitative assessments of the results and image mosaics further confirmed the correctness of the registrations. The limitation of TPS to model surfaces with more than 180° curvature (e.g., the femur) resulted in the registrations limiting to using only a small portion of the femur. Nonetheless, mosaics

showed good alignment of other femoral features. The use of a larger surface can increase the geometry, thus increase the accuracy of the registration and improve the overall alignment. The results provided convincing indication that the proposed algorithm is highly accurate. However, no exact measure of the absolute accuracy can be drawn regarding the registration accuracy for knee joint surfaces generated from MRI, while considering also the errors from imaging, digitization, and modeling. To quantify the overall accuracy, a validation study is required. This can be accomplished by comparing results derived from surface matching with ones obtained using fiducial markers based on MRI. Additionally, repeatability studies on the digitization and registration will provide further evaluation for the overall accuracy. These aspects are addressed in Chapter Six.

The research presented in this chapter verified that the proposed surface matching algorithm functions well with high density 3D MR data and can register surfaces with high quality of fit. Thus, it suggests that the algorithm can be applied to study joint biomechanics and to help monitor OA progressions.

Chapter Six: Accuracy Validation and Repeatability

Studies for the Surface Matching Algorithm

6.1 Introduction

The third specific aim of this research is to validate the absolute accuracy of the proposed surface matching algorithm for registering knee joint surfaces, and also to evaluate the repeatability of the manual digitization and registration processes. The results from these studies will verify how accurate and repeatable the registration approach is for MRI data, and thus will provide knowledge about the reliability of the algorithm for applications of in-vivo assessments of joint conditions. This chapter describes details of the experimental procedures, statistical analysis, and results for the validation and repeatability studies.

6.2 Accuracy Validation

Successful registration with the proposed algorithm for knee joint surfaces acquired at different positions (i.e., different flexion angles) and under different conditions (i.e., relaxed versus loaded) has been demonstrated (refer to Chapter 5). The quality of fit of the two registered surfaces was described by the RMS distances between them. The

accuracy of the proposed algorithm has also been previously tested with synthetic data (Habib et al., 2001, refer to section 2.5.3). However, analyses are needed to evaluate the absolute accuracy of the proposed algorithm for matching knee joint surfaces based on MRI, while accounting for errors arising from imaging, surface digitization, and modeling. The objective of this study is to quantify the accuracy of the registration in a realistic setting (e.g., in a clinical study), such that conclusions could be made about the effects of the registration on the results in studies of joint conditions based on MRI. Specifically, the ability of the registration technique to align surfaces with sufficient accuracy to enable detection of cartilage changes on the order of 1-2 mm associated with degenerative joint diseases, and movements of joint surfaces on the order of 1-2 mm and 1-2° for biomechanics studies is explored.

6.2.1 Experimental Design and Setup

To validate the registration accuracy, results should be validated against a gold standard (i.e., known truth) or be compared to results that are obtained from a more accurate method. Since a gold standard is typically unavailable or hard to establish with the registration of anatomical data, the results from the proposed surface matching algorithm for joint surfaces generated from MR images were compared with ones derived using fiducial markers through an absolute orientation procedure.

6.2.1.1 Absolute Orientation Procedure

The absolute orientation is a common procedure used in the field of photogrammetry to relate the model space coordinate to the object space coordinate system with the use of control features such as points or lines. The relationship is typically explained by the 3D similarity transformation with seven parameters (Equation 3-1). These parameters are solved for using an adjustment process by minimizing the differences between the transformed and the conjugate features. In general terms, absolute orientation is an adjustment procedure to determine the transformation parameters relating the coordinate systems associated with two datasets. This procedure is adapted in this study to derive the transformation relating the surfaces using a set of fiducial markers so they can be compared to the ones derived from surface matching.

6.2.1.2 Required Accuracy for Validation

As a rule of thumb for accuracy validation, the accuracy achieved by the fiducial markers should be at least three times better (American Society of Photogrammetry and Remote Sensing, 2004) than the level the surface matching technique can achieve. The RMS distances of the MR surface registrations (refer to section 5.5) were in the range of 0.2 mm and could act as a rough estimate for the accuracy of the surface matching algorithm. Thus, the required accuracy derived from the fiducial markers should reach a level of approximately 0.06 mm or 60 μm (three times better than 0.2 mm). Measurement errors

of the markers measured from the MR images should not exceed this required accuracy level.

6.2.1.3 Joint Specimen

Direct comparisons of the registration between the surface matching technique and absolute orientation, required that the fiducial markers be fixed in position relative to the knee joint during the scanning session. Skin-attached markers on a human subject were not feasible for this purpose, as minimal movements of the skin markers could lead to errors in excess of the millimeter level (Rheinschmidt et al., 1997). Other options considered were in-vivo bone-implanted markers that would be highly rigid in position. However, the invasive manner of this procedure made it ethically un-feasible for this study. Therefore, a cadaver joint specimen was employed as it could avoid any possible movements during the scanning session. Porcine specimens have been previously used for studies with MRI (Moss, 2001) and were adapted also for this validation study.

The porcine stifle joint is similar in size and shape to the human knee joint, and is relatively inexpensive and can be easily obtained. A fresh porcine knee specimen (less than 9 months of age) was obtained from a local abattoir (Red Deer Lake Meats Ltd., Calgary, AB). The joint capsule was maintained intact. The femoral head and trochanters (the proximal end) and the fibula were removed to allow fixation of the bone sections to a frame that was placed inside the MR gantry. Due to the delay between

specimen supply and scanning, the specimen was frozen after preparation but was completely thawed out before scanning. Freezing has been reported to alter tissue contrast levels in MR imaging (Ronsky et al., 2000), thus thawing the tissue should minimize any artifacts. Additionally, as the bone surfaces are used for the registration in this study, minimal effects should be incurred on the results by the freezing and thawing procedures.

6.2.1.4 Fiducial Markers

The type, size, shape, and geometry of the markers were very important for this validation study. The main criteria defined for the markers were:

- 1) Non-ferromagnetic materials to enable imaging with MR,
- 2) Strong homogenous MR signal with minimal MR artifacts,
- 3) Able to be accurately digitized and modeled from the MR images,
- 4) Able to be mathematically represented for the absolute orientation procedure,
- 5) Position fixed with respect to the porcine specimen, and
- 6) Encompassed inside the allowable MR FOV.

Based on satisfying the above criteria, two types of markers were considered and evaluated for this study: spherical markers and linear features. Spherical markers can be reliably captured by the MR image slices as circular cross-sections at any image orientation. The circumference or the edge of each circular cross section can be digitized

from each image slice and a sphere fitting algorithm written in MATLAB (Least Squares Geometric Elements library, NPL Centre for Mathematics and Scientific Computing) can then be applied to the digitized points. This algorithm uses a least squares approach to best-fit a sphere to the point cloud and calculates the 3D centroid of the sphere. The RMS of the residuals between the digitized points and the best-fitted sphere are also calculated. The markers' centroids are used in a point-based absolute orientation procedure to derive the transformation parameters relating the two datasets. One disadvantage of spherical markers is that a small shift in the image slice positions can lead to a small shift in the centroid location especially for small markers that are captured with only a few MR image slices. Also, image slices that are further away from the centre of the sphere will have more diffused edges due to partial volume artifact, thus making it more difficult to digitize. Therefore, generally speaking, the markers should appear on at least five or more image slices.

Linear features have shown to be accurate for registration of 3D geographic data (Habib and Alruzouq, 2004) and are commonly used in neurosurgery for the establishment of a reference frame (e.g., the Olivier-Bertrand-Tipal frame, Tipal Instruments, Montreal, Quebec). Linear markers, in the form of narrow cylinders, can also be reliably captured by MR slices as circular or elliptical shapes, depending on the orientation to the image plane. The points on the edges of these elliptical shapes can then be digitized and ellipse fitting, written in MATLAB (Fitzgibbon et al., 1999), can be used to identify the centre of the cylinder at each cross-section. Finally, 3D line fitting of these centre points with

MATLAB (Least Squares Geometric Elements library, NPL Centre for Mathematics and Scientific Computing) can produce a centerline to represent the marker. For the line-based absolute orientation procedure, the lines are represented by two points, with no requirements for using conjugate points to define conjugate lines (Habib and Morgan, 2003b). Thus, conjugate markers can be represented as lines with different lengths with this approach. However, linear markers are less flexible as their orientations have to be relatively perpendicular to the image plane to avoid very elongated ellipses. Additionally, the diameters of the cylinders must be sufficiently large (e.g, span across a minimum of five pixels) such that the edges are clearly defined and the centers can be accurately determined.

The geometry of any fiducial marker is very important for any form of registration to allow accurate estimations for the transformation parameters. For spherical markers, a minimum of three markers are needed to derive the seven parameters, with more markers increasing the redundancy and improving geometry. The markers cannot be co-linear as this will result in an under-determined solution. Similarly, for linear markers a minimum of three markers at varying orientations are required and the marker configuration must not be coplanar. With limited imaging FOV, there is a substantial challenge in optimizing the position of the joint specimen apparatus together with the markers while considering the geometry of the setup.

A pilot study was performed to investigate the above issues and to quantify the accuracy of determining the centroids and centerlines of the spherical and linear markers respectively. Both types of markers were measured with the FaroArm (FARO Technologies Inc., Lake Mary, FL) located in the Bioengineering Lab of CCIT (Schulich School of Engineering, University of Calgary, Calgary, AB). The FaroArm is a precise measuring device with a reported accuracy of 0.025 mm. The FaroArm measurements were used as an independent measurement to verify the accuracy of the MR measurements of the markers.

To comply with the first design criteria, plastic ping-pong balls (STIGA, China) with diameters of approximately 39 mm were used as spherical markers (Figure 6-1). For an MR image slice thickness of 3.0 mm, the balls would appear in approximately 18 slices. The balls were filled with canola oil (Safeway, Canada) as it can be easily obtained and has shown to produce strong and homogeneous MR signal (Moss, 2001). Ping-pong balls were chosen as they are spherical, easy to find and inexpensive, and the thickness of the plastic is thin and evenly distributed over the inner and outer spherical surfaces. As MR captured the signal of the oil contained inside the balls, it is thus more important for the ball to be spherical on the inside than the outside. Approximately 30 well distributed points were measured on each ball surface with the FaroArm (Figure 6-1) and the CAM2 Measure X software (FARO Technologies Inc., Lake Mary, FL) was used to automatically calculate the centroids and diameters of these balls.

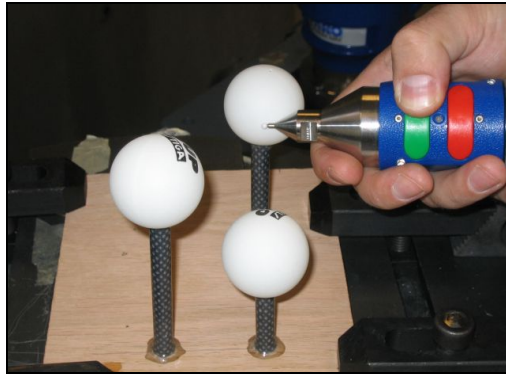


Figure 6-1: Spherical markers (ping-pong balls) being measured with the FaroArm.

For the linear markers, two sizes of circular tubes were used: three fiberglass tubes of 3 mm diameter and three plastic tubes of 5 mm diameter. Two different diameters were tested to analyze the effect the size had on the accuracy of the MR measurements. The different materials of the tubes were not considered and evaluated in this study. The tubes were mounted on a wooden frame with different orientations and positions (Figure 6-2a). One challenge of this set up was to ensure that the tubes were inserted linearly and rigidly into the wooden boards without any bending. The two end points of each tube were measured with the FaroArm (Figure 6-2b) and were used to represent the tubes for subsequent calculations. The tubes were then filled with a gadolinium solution (Magnevist, Berlex Canada), which is a contrast agent that is commonly used in MR imaging to enhance the signal. Although canola oil could produce sufficient MR signal, the gadolinium solution was used here to ensure that strong signals could be captured for the small tubes.

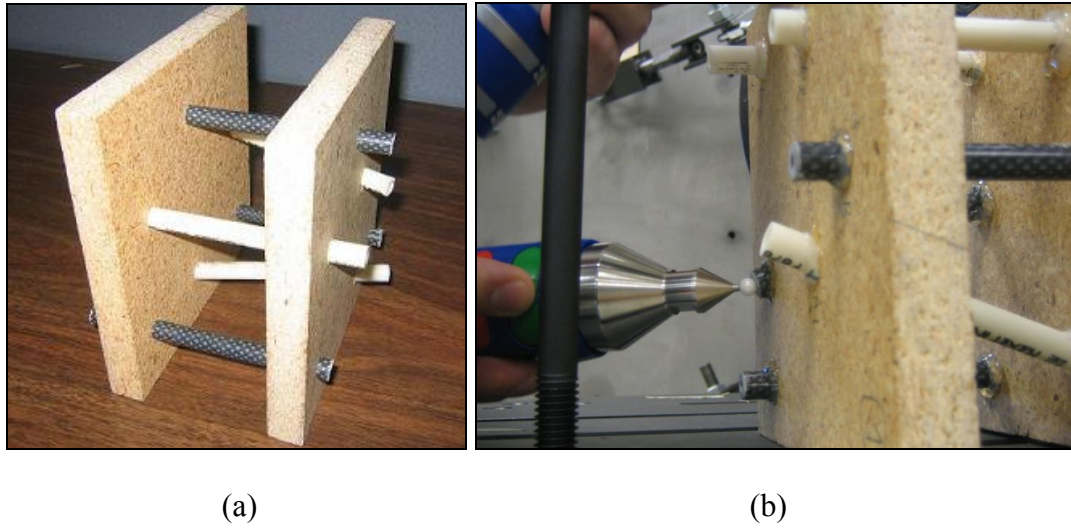


Figure 6-2: Six linear markers mounted on wooden frame (white: 5 mm diameter; black: 3 mm diameter) (a) with end points measured by the FaroArm (b).

For the MR image acquisition, the balanced SSFP sequence was used with the 3-telsa MR unit (sagittal, TR = 4.0 ms, TE = 1.0 ms, flip angle = 40°, FOV = 16 cm × 16 cm, 256 × 256 matrix), resulting in a resolution of 0.625 mm × 0.625 mm × 3.000 mm (Figure 6-3). Several scans were acquired at different frame positions and MR coordinate systems as described in Table 6-1 for each type of markers. The MR coordinate system was defined by setting the origin around the centre of the markers' locations to relate its position to the MR gantry.

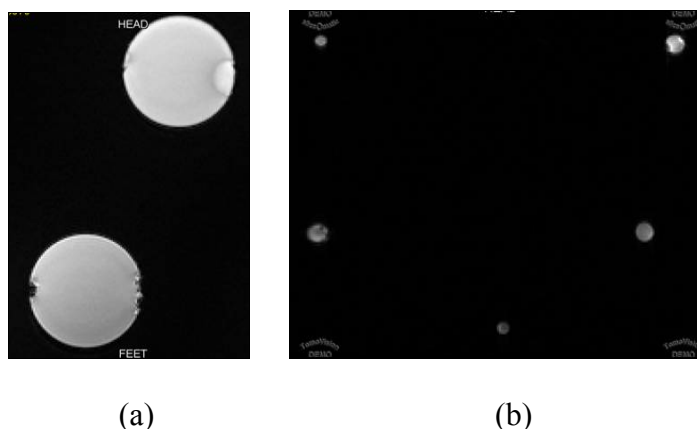


Figure 6-3: MR images of the spherical (a) and linear markers (b) for the pilot study.

Table 6-1: The MR scans acquired for each type of fiducial markers for the pilot study.

Marker	Scan #	Position	Coord. System	Descriptions
Spheres	1	1	1	Markers located at position 1 and the first MR coordinate system was defined
	2	2	1	Markers moved to a different position (position 2) but with the same MR coordinate system (coordinate system 1)
	3	2	2	Markers remained at position 2 but a different coordinate system was set (coordinate system 2)
Lines	4	3	3	Markers located at a new position and with a new coordinate system defined
	5	4	4	Markers moved to a different position (position 4) and a new coordinate system was set

The images revealed that the fiberglass tubes (the smaller circles in Figure 6-3b) did not appear clearly, with one tube completely missing. This finding was probably attributed to the material properties of the tubes and in-complete filling of the gadolinium solution. With high contrast between the markers and the background signal, a semi-automatic digitization algorithm, Non-Maxima Suppression (NMS), written in MATLAB (Moss,

2000), was used to digitize the edges for both types of markers for each of the scans (Figure 6-4). This algorithm is based on two common principles for edge detection: suppression of local non-maxima magnitude of the gradient of the image intensity in the direction of this gradient, and edge detection using the zero-crossings of the Laplacian of the intensities. The centroids and centerlines of the spherical and linear markers were determined using the best-fitting algorithms.

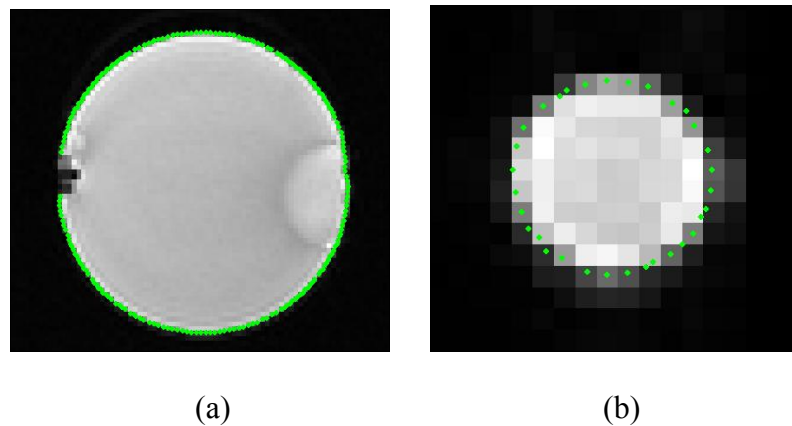


Figure 6-4: Digitized edges (green points) of the spherical (a) and linear markers (b) with NMS (figures are not to scale).

To validate the accuracy of the MR measurements of the markers' centroids and centerlines, point-based and line-based absolute orientations between the FaroArm and MR centroid measurements were performed in MATLAB. The root-mean-square errors (RMSE) were calculated for the X, Y, and Z directions. The RMSE can be mathematically defined using the average and standard deviation (SD) of the errors (i.e., differences between the MR and FaroArm measurements of the markers after absolute orientation):

$$RMSE = \sqrt{(average)^2 + (SD)^2} \quad (6-1)$$

Tables 6-2 and 6-3 present the RMSE results for the spherical and linear markers for each scan, respectively. The average RMSEs were significantly smaller for the spheres than the linear markers by an order of magnitude. The combined average of the RMSEs also indicated that the accuracy for identifying the spherical centroid from MRI would be in the range of 50 μm when considering also the accuracy of the FaroArm measurements. The linear markers showed largest errors in the Y and Z directions (the directions of the image plane) which were most likely attributable to digitization and ellipse fitting errors. Based on these results, the spherical markers were chosen for the validation study, as they were also easier to setup and attach to the joint specimen.

Table 6-2: RMSE of the coordinate differences between FaroArm and MR measurements for the three spherical markers after point-based absolute orientation.

Scan #	RMSE of the Coordinate differences (mm)		
	X	Y	Z
1	0.052	0.057	0.049
2	0.019	0.020	0.018
3	0.009	0.007	0.014
Average	0.027	0.028	0.027

Table 6-3: RMSE of the coordinate differences between FaroArm and MR measurements for five linear markers after line-based absolute orientation.

Scan #	RMSE of the Coordinate differences (mm)		
	X	Y	Z
4	0.176	0.479	0.587
5	0.062	0.263	0.560
Average	0.119	0.371	0.573

produced strong MR signal. However, alterations in signal may arise when imaged together with the porcine specimen. Therefore, although the water appeared bright for this test, it might not be ideal when imaged with the joint tissues that are composed of a high percentage of water. Gadolinium solution thus was chosen as the filler material for the fiducial markers for the validation study.

6.2.1.6 Validation Frame Design and Setup

The validation procedure required a positioning frame to be fabricated to allow fixation of the joint specimen and the markers in rigid positions. Several criteria were defined for this validation frame:

- 1) Non-ferromagnetic materials,
- 2) Adjustable but rigid positioning device to enable different specimen sizes,
- 3) Rigid support provided for the markers and porcine knee specimen, and
- 4) Overall dimensions of device with markers and joint within the allowable MR FOV.

Several designs were proposed for the frame with the final design adapted from one proposed for a parallel study that also uses porcine knee specimen and MRI (Figure 6-6a). The frame dimensions were designed to accommodate an average porcine joint size fit into the MR gantry (dimensions: 72 cm × 22 cm × 32 cm). The frame was constructed entirely with wood, plastic, and nylon. The porcine knee joint was fixed to the bone positioning containers using a construction cement (Quick Plug Hydraulic Cement, DAP,

USA). The specimen was carefully wrapped with plastic wrap (Figure 6-6b) to contain any fluids and to minimize tissue dehydration. Six spherical markers filled with gadolinium solution (Magnevist, Berlex Canada) were rigidly attached to the frame and positioned around the joint (Figure 6-7).

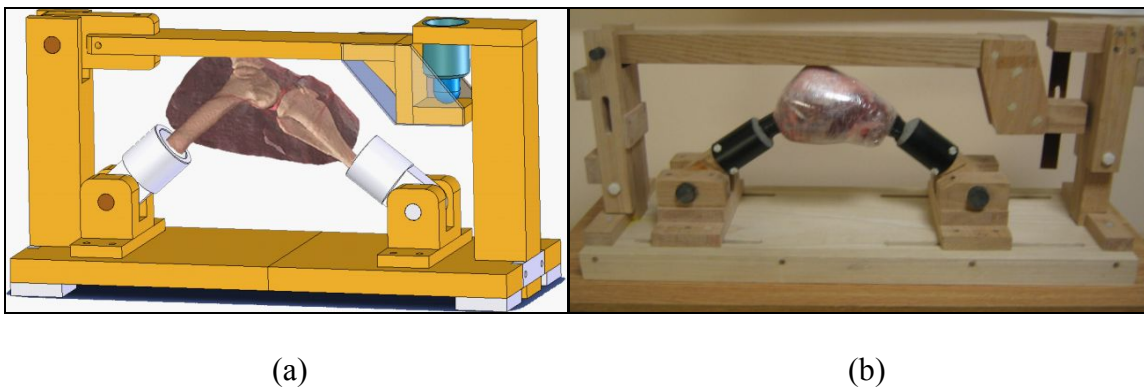


Figure 6-6: Validation frame (a) constructed with wood and plastic (Robu, 2006), and the porcine knee specimen was fixed using construction cement (b).

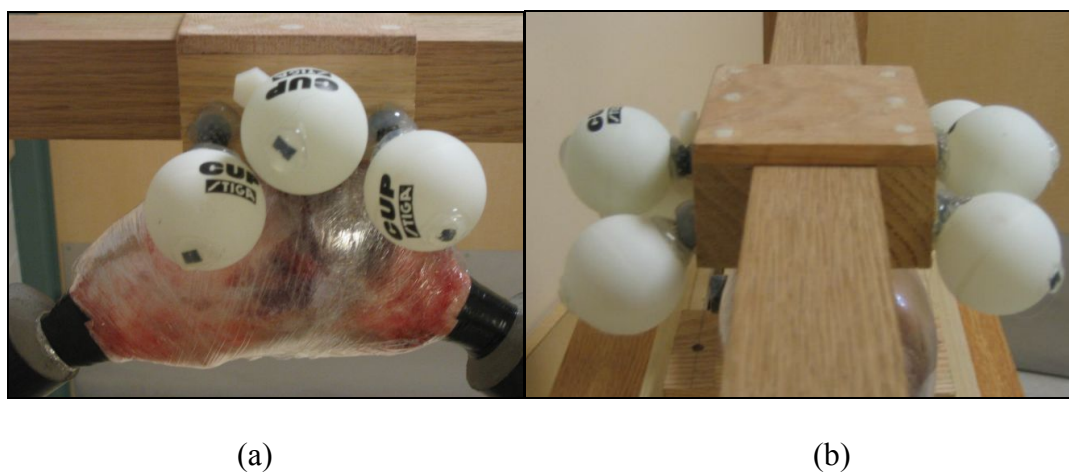


Figure 6-7: Six spherical markers were rigidly attached to the frame with three markers on each side of the joint (a, b).

6.2.2 MR Scanning

Scanning was performed using the 3-telsa MR unit with the general purpose flex coil. Similar to the experiments with MR data of human knee joints (Chapter Five) and the marker pilot studies, the balanced SSFP sequence was also used (sagittal, TR = 5.1 ms, TE = 1.6 ms, flip angle = 40°, resolution = 0.625 mm × 0.625 mm × 3.000 mm). A larger FOV (32 cm × 32 cm, 512 × 512 matrix) was required to encompass the six markers and the knee joint. Consequently, 120 sagittal image slices were acquired. Four scans were taken with this image sequence. The frame was re-positioned between some of the scans and a new coordinate system was also defined for the scans. More descriptions are provided in Table 6-4 for these scans. Figure 6-8 shows an example of the MR images of the porcine joint and spherical markers.

Table 6-4: MR scans acquired for the validation frame with the porcine joint and markers.

Scan #	Position	Coord. Sys.	Descriptions
1	1	1	Frame located at the first position and the first MR coordinate system was defined.
2	2	1	Frame moved to a second position but the same coordinate system was used (coordinate system 1)
3	2	2	Frame remained in position 2, but a new MR coordinate system was set (coordinate system 2)
4	3	3	Frame moved to another position and a new coordinate system was also defined.

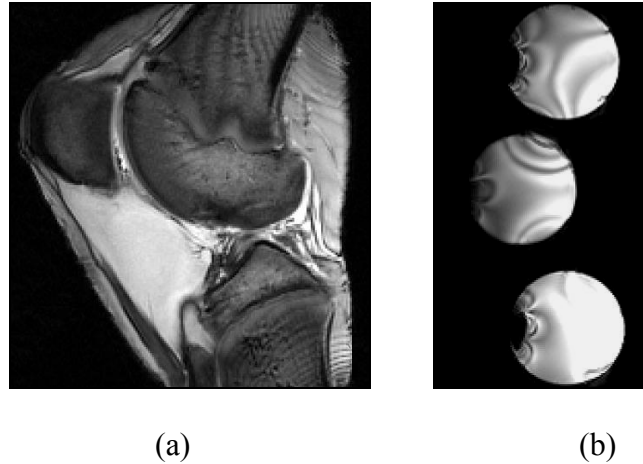


Figure 6-8: MR image of the porcine knee specimen (a) and the spherical markers (b) (figures are not to scale).

6.2.3 Surface Matching and Absolute Orientation Results

Surface registrations with the proposed surface matching algorithm were performed using the porcine femoral surfaces from the different scans as listed in Table 6-5 (refer to Table 6-4 for scan numbers). Digitization and surface modeling were done using the techniques and algorithms as described in sections 5.3 and 5.4. The results indicated well-fitted surfaces with average RMS distances of 0.186 ± 0.011 mm for all the tests. Transformation parameters were estimated for each registration and found small translations and rotations (maximum translation was 4.9 mm and maximum rotation was 1.4°) between different frame positions. The scale factor was fixed as one for the registrations with the assumption that the femoral bone surfaces remained rigid. Qualitative analysis of the matching results confirmed that the registrations were successful, with the non-matches located randomly over the surfaces and around the edges (Figure 6-9). These were speculated to be digitization errors. This is expected as

the cartilage of the young porcine specimen was thin (e.g., femoral cartilage was less than 2 mm) resulting in greater difficulties for identifying the femoral bone-cartilage interface.

Table 6-5: The MR scans (refer to Table 6-4) used for the registrations in the validation study.

Test	Reference Scan #	Transformed Scan #
1	1	2
2	2	3
3	2	4
4	3	4
5	1	3
6	1	4

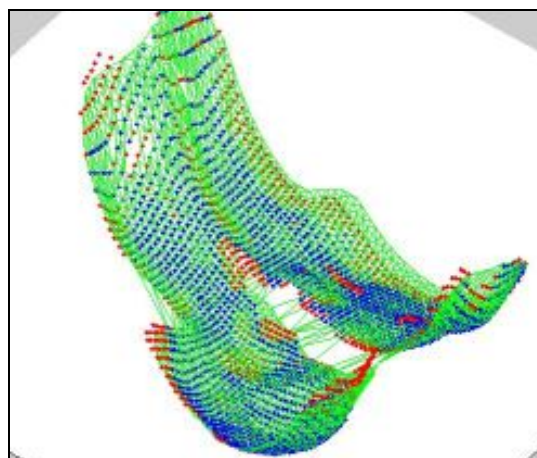


Figure 6-9: Registered femoral surfaces of the porcine specimen with the green mesh representing the reference surface, blue points representing the matches, and red points representing the non-matches.

As anticipated, the spherical marker signals were weaker compared to the ones acquired for the pilot study, when these markers were acquired together with the porcine joint. Also, since the markers were located at the edge of the imaging FOV and positioned in close proximity with each other and the specimen tissue, banding artifacts and distortions

(i.e., markers were less spherical) were present (Figure 6-8b). Therefore, the digitization was manually performed with SliceOmatic, instead of employing the semi-automatic NMS edge detection algorithm that was used for the pilot studies. In addition, only a minimal number of points could be digitized at the edges of each marker (i.e., image slices furthest away from the centroid) due to partial volume effects. Inclusion of these artifacts would lead to errors in the marker measurement thus could directly affect the accuracies of centroid determination. The effects of these artifacts were not investigated as it was beyond the scope of this study.

On average, approximately 300 to 400 points were digitized for each marker. The centroids were determined by applying sphere-fitting to the digitized points. The point-based absolute orientation procedures were performed with the centroids between the same scans as listed in Table 6-5. Transformation parameters and errors/differences of the marker coordinates were derived for each test. The mean errors in the X, Y, and Z directions were found to be zeros for all the tests, thus indicating that there were no biases in the marker measurements. The RMSEs of the errors for the tests (Table 6-6) indicate that the largest errors occurred in the Y direction, presumably as it was along the image slice direction where the largest errors would be expected for centroid determination (refer to Figure 5-7 for the descriptions of the coordinate axes). However, these errors were still within the size of an image pixel (0.625 mm). The combined average RMSE for the coordinates was 0.539 mm. Therefore, it can be concluded that

for these MR scans, the accuracy for the marker digitization and centroid determination was approximately the size of an image pixel.

Table 6-6: The RMSEs of the coordinate differences between the markers after the absolute orientation procedures.

Test	RMSE of Coordinate Differences (mm)		
	X	Y	Z
1	0.077	0.614	0.101
2	0.107	0.561	0.163
3	0.081	0.691	0.178
4	0.101	0.457	0.159
5	0.079	0.231	0.153
6	0.108	0.488	0.202
Average	0.092	0.507	0.159

Unfortunately the accuracy of the marker measurement was insufficient to provide a gold standard for validation (i.e., required accuracy was 60 μm , refer to section 6.2.1.2). Nonetheless, this was the best accuracy that could be achieved using point-based fiducial markers when considering all the error sources with MRI.

6.2.4 Accuracy Analysis and Discussions

The fiducial markers were examined for use as the gold standard and found to provide insufficient accuracy for this purpose. However, the accuracy of the surface matching algorithm could still be evaluated by comparing the surface matching results with the ones obtained from the absolute orientation procedures. One approach for this was to statistically compare the values of the transformation parameters derived from both techniques. Table 6-7 shows the transformation parameters as an example that were

derived from the surface matching algorithm and absolute orientation procedure between two datasets (Test 5 from Table 6-5). However, because there could be correlations between the parameters, statistical analysis between individual parameter values might show significant differences, even though the entire set of parameters could still lead to statistically equal transformation. Therefore, the most appropriate approach to evaluate the registration accuracy was to compare the actual transformations resulting from surface matching and from absolute orientation techniques.

Table 6-7: The transformation parameters derived from surface matching and point-based absolute orientation procedure between two datasets.

Technique	X_T (mm)	Y_T (mm)	Z_T (mm)	ω (°)	ϕ (°)	κ (°)
Surface Matching	-0.857	-0.056	-0.130	-0.523	1.007	-0.154
Absolute Orientation	-0.500	-0.175	-0.410	-0.380	-0.084	-0.058

This comparison was performed by transforming an object with each set of the parameters and evaluating differences in the resulting physical location (i.e., X, Y, and Z coordinates) of that object. A box with dimensions of 100 mm × 160 mm × 100 mm and modeled by 2057 3D points was used. This box covered a similar volume of the combined porcine knee specimen and spherical markers. The points were evenly distributed with the origin of the coordinate system located at the centre of the box (Figure 6-10). The points within box were transformed with each set of transformation parameters derived from surface matching (T_{SM}) and absolute orientation (T_{AO}). Comparisons were made by statistically evaluating how similar the transformed boxes were in their locations (Figure 6-10).

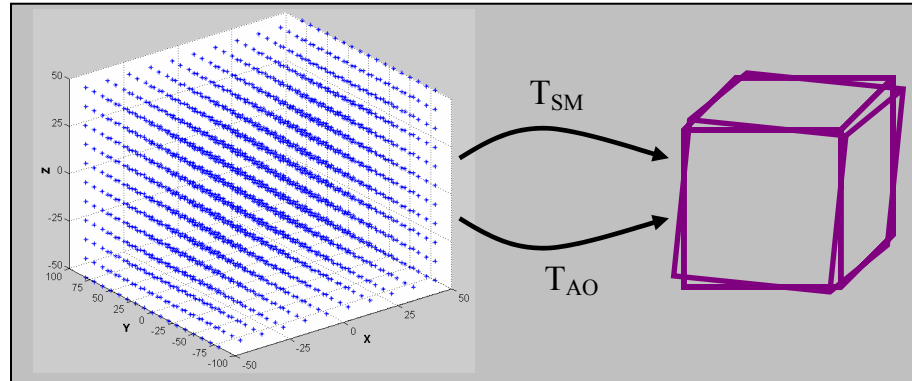


Figure 6-10: 3D coordinates of a box were transformed using parameters from surface matching (SM) and absolute orientation (AO), and the resulting locations were compared.

The differences in the X, Y, and Z coordinates of the box between the two techniques were computed for each test (refer to Table 6-5 for the list of tests), and the RMSE of these differences were computed (Table 6-8). Larger errors (in the range of 0.6 mm) were found in the X and Z directions (the image plane direction, refer to Figure 5-7) with the last test showing the worst results. Investigations were done to attempt to identify the sources of errors for the last test but no apparent reasons were found. The averages of the RMSE were on the order of a pixel size (particularly in the image plane direction), thus were comparable to the accuracy of the marker measurement and centroid determination procedures.

Table 6-8: The RMSEs of the coordinate differences of the box between surface matching and absolute orientation procedure with markers.

Test	RMSE of Coordinate Differences (mm)		
	X	Y	Z
1	0.532	0.255	0.344
2	0.558	0.316	0.389
3	0.709	0.126	0.756
4	0.423	0.191	0.389
5	0.705	0.154	0.676
6	0.954	0.169	0.897
Average	0.647	0.202	0.575

Based on the results and observations from this validation study, it can be inferred that the point-based absolute orientation procedure with spherical markers measured from MRI would not outperform the proposed surface matching technique. Nevertheless, the two techniques were compared and results showed that the proposed surface matching algorithm could match knee joint surfaces generated from MRI with a fit of approximately 1/3 of a pixel size and had an absolute registration accuracy in the range of the size of one pixel.

6.3 Repeatability Studies

Repeatability is the ability of a system or a technique to provide consistent outcomes when used by a single operator. For this research, repeatability studies were needed to understand how consistent the manual digitization and the registration are with the

proposed surface matching algorithm for the same datasets. This section describes the procedures and results for these studies.

6.3.1 Digitization and Registration

The MR scans at 0° and 30° of one subject described in section 5.2 were adapted for this study as they represented different positions and conditions (relaxed versus loaded). The femoral surfaces were manually digitized for each set of scans five times with SliceOmatic on separate days by one operator. These surfaces were then modeled with TPS, using the same surface re-sampling intervals (1.0 mm) and smoothing parameter ($\lambda = 0.6$), which provided ten different surfaces (Figure 6-11). Registrations were then performed with the proposed algorithm between each pair of surfaces in three separate categories: 0° with 0° , 30° with 30° , and 0° with 30° . For the 0° with 0° and 30° with 30° categories, the first digitization was used as the reference surfaces for the registrations. For the 0° and 30° registrations, the 0° surfaces were used as the reference. The registrations yielded four sets of transformation parameters (T in Figure 6-11) for the 0° with 0° and 30° with 30° categories, and five sets of parameters for the 0° with 30° registration.

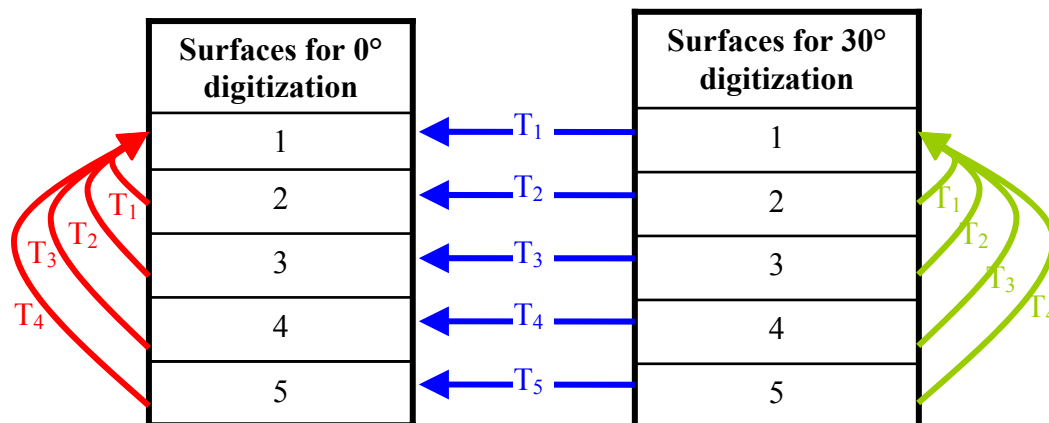


Figure 6-11: Ten surfaces generated from different digitization with arrows indicating each set of registration (red: category 1: 0° with 0°, green: category 2: 30° with 30°; blue: category 3: 30° with 0°).

6.3.2 Repeatability Analysis and Discussion

As potential correlations between the transformation parameters could exist, similar to the validation study, comparisons between individual values might not be suitable for analyzing the repeatability. Therefore, the method used to statistically evaluate the validation study was adapted here, where a box was transformed by multiple sets of parameters and the resulting coordinates of the box were compared. If the digitization and registration were repeatable, these transformed coordinates of the box should be similar. For this study, a box with dimensions of 120 mm × 120 mm × 80 mm and modeled by 1521 3D points was used, which was similar in size to the human patellofemoral joint. The points were transformed with each set of transformation parameters (T) from each category. Comparisons were made by statistically evaluating how similar the transformed boxes were in their locations (Figure 6-12).

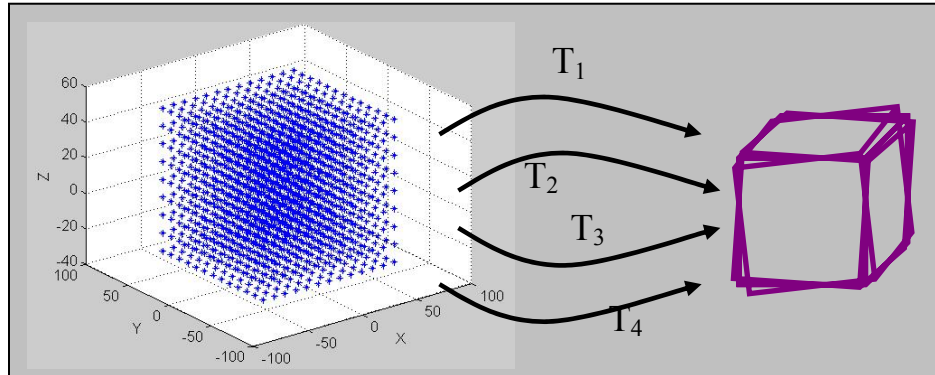


Figure 6-12: The 3D coordinates of a box were transformed with each set of transformation parameters and the resulting locations were compared.

For the comparisons, the differences in the X, Y, and Z coordinates of the transformed points were computed, using the first transformation as a reference. This resulted in three sets of coordinate differences for the first and second categories, and four sets of differences for the 0° and 30° registrations. The RMSEs of all the coordinate differences were calculated for each category and are displayed in Table 6-9. The errors for the Y coordinate were clearly smallest in comparison with X and Z. This was likely because the Y axis lied along the MR image slice direction (refer to Figure 5-7), so the points digitized from an image slice would have a fixed Y coordinate for that image, thus resulting in highly repeatable Y coordinates for the digitization. Also, the RMSEs were smaller for 30° with 30° than the 0° with 0° registrations, likely because the MR images of the 30° flexion were clearer for this particular dataset, and thus were easier to digitize repeatably. As expected, the errors for the 0° with 30° registrations appeared to be higher as they were caused by combined digitization errors from both 0° and 30° MR scans.

Table 6-9: RMSEs of XYZ coordinate differences of the box between the transformations for the repeatability study.

Categories		RMSE of Coordinate Differences (mm)		
		X	Y	Z
1	0° with 0°	0.230	0.118	0.253
2	30° with 30°	0.130	0.059	0.171
3	0° with 30°	0.250	0.134	0.286

Overall, the RMSEs, in the range of 0.2 mm, showed that the manual surface digitization and registration for MR knee joint surfaces with the proposed surface matching algorithm were highly repeatable, considering the MR image resolution (0.625 mm × 0.625 mm × 3.000 mm) of the involved datasets.

To confirm the results and conclusions obtained from the methodology of comparing coordinate differences of a box after transformation, the Analysis of Variance (ANOVA) was also performed for the transformed X, Y, and Z coordinates of the box for each registration category using the statistical program R (The R Foundation for Statistical Computing, version 1.8.1). These statistical tests could determine whether there were any differences between the means of these coordinates within a category. The results could provide evidence about the repeatability of the digitization and registration procedures. The null hypothesis was defined as follows for each category:

- H_0 : Equal means for the coordinates of the transformed cube

A small p -value (e.g., < 0.05) from the ANOVA test would provide convincing evidence that at least one of the coordinate mean was different than the others. Table 6-10

summarizes the ANOVA test results for the X, Y, and Z coordinates at each category. The large p -values ranging from 0.872 to 0.985 indicate that the means of the coordinates were statistically equal for the registrations of each categories, thus confirm that the registration was repeatable based on different surface digitization.

Table 6-10: ANOVA results for the XYZ coordinates of the box for the three registration categories.

Categories		p -values		
		X	Y	Z
1	0° with 0°	0.872	0.985	0.961
2	30° with 30°	0.981	0.952	0.961
3	0° with 30°	0.898	0.969	0.969

The results from the statistical analysis indicated that the digitization and registration procedures were highly repeatable for the femoral surfaces from MR images. This means that the digitization and registration results did not depend on the time the data was processed by a single operator. Repeatability is an indication of reliability, thus the results further confirms the efficacy of the surface matching algorithm for biomechanics and OA studies with MRI. The findings from the study also implies that the digitization and registration procedures will also be highly repeatable for patellar surfaces, as the patella was shown to produce better quality of fit than the femoral surface for registration (refer to section 5.6). For other joint tissues, such as the cartilage surfaces, more studies will be needed to investigate the repeatability, as the signal contrast for identifying these surfaces may be different than the bone surfaces. Importantly, the image quality and signal contrast can directly affect the repeatability of the registration as was found in this

study. In this study, the digitization was performed by a single operator with experience in manual digitization of joint surfaces using SliceOmatic. Inter-observer reliability needs to be investigated in the future with novice operators and minimal training.

6.4 Summary

A validation study was presented in this chapter to quantify the absolute accuracy of the surface matching algorithm for registering actual clinical MRI data of joint surfaces, while taking into account the imaging environment and numerous error sources (e.g., digitization and surface modeling). The proposed approach was to validate surface matching results of a porcine knee specimen with ones derived using spherical markers based on a point-based absolute orientation procedure. However, results indicated that the accuracy of the marker measurements and representation from MRI was not sufficient to act as a known truth for the validation. Nevertheless, comparisons were made between the two techniques and revealed that the surface matching algorithm could achieve an absolute accuracy of approximately the size of an image pixel for the registration of joint surfaces generated from MRI.

Repeatability studies were also presented to evaluate the repeatability of the manual digitization procedure and registration algorithm for MRI. Femoral surfaces of a human subject were used for this study and results showed that the digitization and registration were highly repeatable, with errors in the range of approximately 1/3 of a pixel size. The

signal contrast for other joint tissues such as cartilage is different than bone surfaces, thus the results found for bone surfaces can not be directly implied for other tissue types. Future studies should be conducted for other joint structures.

The results from the validation and repeatability studies presented in this chapter confirmed that the proposed surface matching algorithm is able to align surfaces with sufficient accuracy (i.e., an image pixel size, which is typically in the sub-millimeter level) to enable detection of cartilage changes on the order of 1-2 mm associated with degenerative joint diseases, and movements of joint surfaces on the order of 1-2 mm and 1-2° for biomechanics studies. The validation study provides a quantitative measure to describe the absolute registration accuracy of the proposed algorithm for 3D MR data, which can be used to quantify the effect of the registration on results for MR applications (i.e., errors introduced by registration). This advances over other technique such as the elastic registration developed by Stammberger et al. (1999) (refer to section 2.5.1.3) as no measures were reported in their study to directly quantify the registration accuracy and how the technique affected their results.

Chapter Seven: Applications of In-Vivo Studies of Degenerative Joint Conditions

7.1 Introduction

The capability of the proposed algorithm of producing a registration accuracy of approximately the size of one image pixel for joint surfaces generated from MRI has been demonstrated. Additionally, the manual digitization and the surface matching procedures were highly repeatable. These results thus suggest that the algorithm is feasible for accurate in-vivo studies of joint biomechanics and joint health status. Three applications with the proposed algorithm are presented in this chapter: 1) register temporal MR data to verify the feasibility of the algorithm to detect changes in cartilage volume associated with OA, 2) quantify patellar movement with respect to the femur based on the transformation parameters, and 3) quantify changes in contact area locations between the patellar and femoral cartilage at different knee flexion angles. The first application is useful in assisting with non-invasive longitudinal monitoring of OA. The two remaining applications assist in understanding the role that joint position and contact may play in conditions such as patellofemoral pain, patellar dislocation and chondromalacia. Combined, these applications will provide evidence in support of the importance of registration for in-vivo assessments of joint conditions.

7.2 Registration for Disease Monitoring

The first application employed the proposed algorithm to register temporal datasets to help in the detection of longitudinal changes in cartilage volume for monitoring OA progression. This was a collaborative study with Drs. J. Jaremko and R. Lambert (University of Alberta, Edmonton, AB, Canada) and the work has been accepted for publication (Jaremko et al., 2006). With successful registration, cartilage volume can be automatically calculated for the subsequent scans within the same regions of the interest defined for the baseline/first scans. Successful application of this technique avoids the need for the tedious and time-consuming process to manually re-measure cartilage volume for each set of scans. Thus, with the help of the proposed surface matching algorithm, this application presents a rapid approach for monitoring temporal cartilage volume changes. Studies were done on temporal data of both healthy knees and knees with established OA to verify the feasibility and reliability of the proposed methods for registering temporal datasets and conducting cartilage volume measurements.

7.2.1 Data

The dataset for this study was supplied by Dr. R. Lambert and Dr. J Jaremko, University of Alberta. The data was acquired with a 1.5-telsa MR unit (Symphony, Siemens AG, Munich) located in Edmonton, Canada. A T1-weighted 3D spoiled gradient-echo fat-saturated sequence was employed for this dataset (sagittal, TR = 42 ms, TE = 10 ms, flip angle = 20°, FOV = 16 cm × 16 cm, 512 × 512 matrix) with a resolution of 0.3125 mm ×

0.3125 mm × 1.0 mm and a scan time of approximately 32 minutes. This sequence showed cartilage as a bright structure with diminished signal for surrounding tissues (Figure 7-1). Two groups of subjects participated in this study. Institutional ethics were approved and written informed consents were obtained from each subject prior to imaging. Knees of nine healthy subjects, with no signs of symptoms of OA, were imaged at full extension at two time points within an interval of two weeks. The second group included three patients with knee OA, who were undergoing a clinical trial for experimental OA therapy (patients were participants in either treatment or control group). The investigators were blinded as to whether the individual OA subject was under treatment or whether he/she was part of the control group. Subjects in the OA group also had images of their knees imaged at full extension, with four scans at six-month intervals up to two years. Table 7-1 summarizes the subject information.



Figure 7-1: Image of a healthy knee at full extension acquired by a 1.5T MRI unit with a T1-weighted 3D spoiled gradient-echo fat-saturated sequence.

Table 7-1: Information of the subjects with normal knees and knees with OA.

Normal	Sex	Age	Knee	
N1	M	48	L	
N2	F	42	R	
N3	M	41	L	
N4	M	41	R	
N5	M	39	R	
N6	M	34	R	
N7	F	33	R	
N8	F	28	R	
N9	F	23	L	
Mean ± SD		36.6 ± 7.8		

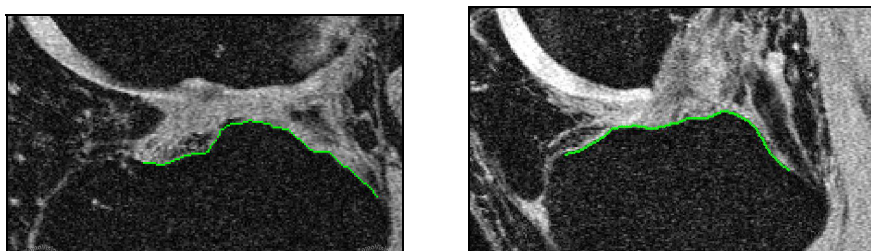
OA	Sex	Age	Knee	Comments
OA1	Unknown	59	L	Moderate OA
OA2	Unknown	65	R	Severe OA
OA3	Unknown	71	L	Severe OA

7.2.2 Methods

The tibial intercondylar eminence (located between the two tibial plateaus) was digitized and used for the surface registration. Only the intercondylar eminence was used due to its unique shape of providing sufficient geometry for registration. Additionally, this structure is unlikely to change in shape between the temporal scans. The small size of the surface resulted in a much faster digitization process. To evaluate the feasibility and reliability of the registration and cartilage measurement techniques, four hypotheses were defined for this study: (1) accuracy of surface registration would not be impaired in patients with advanced OA despite local changes between scans (e.g., osteophyte growth), (2) surface registration using the intercondylar eminence would be faster than and equivalent in accuracy to digitization of the entire tibial plateau, (3) semi-automatic digitization would lead to comparable registration accuracy and cartilage volume

measurement as manual digitization, and (4) speed and inter-scan reliability of cartilage volume measurement using surface registration would be at least comparable to results reported by others in normal subjects.

For the nine normal subjects, digitization of the intercondylar eminence was done manually using SliceOmatic (Figure 7-2a). To test the second hypothesis, the entire tibial plateaus were digitized for two normal subjects (N2 and N5) and one OA patient (OA2). Due to the high contrast between the tibial bone surface and surrounding tissues (Figure 7-1), scans of two normal subjects (N2 and N5) were also digitized with a custom-written semi-automatic digitization program based on Canny edge detection in MATLAB (The Mathworks, Inc., Natick, MA, version 6.5) (Figure 7-2b). For the three OA patients, the tibial surfaces were digitized with the semi-automatic Canny edge detection. For subject OA2, tibial surface was also manually digitized using SliceOmatic. To test the third hypothesis, surface matching results and cartilage volume measurements obtained from the manual and semi-automatic digitization were compared for subjects N2, N5, and OA2.



(a)

(b)

Figure 7-2: Digitized tibial intercondylar eminence (green line) manually by SliceOmatic (a) and with semi-automatic digitization using Canny edge detection (b).

The MR resolution of the scans was adequate ($0.3125 \text{ mm} \times 0.3125 \text{ mm} \times 1.0 \text{ mm}$), thus no surface re-sampling was required. The baseline scans (i.e., first time point) were used as the reference surface for the registration. The intercondylar eminence surfaces from the subsequent scans (or the tibial plateau surfaces when testing the second hypothesis) were registered to the baselines using the surface matching algorithm, with the distance threshold set at 0.25 mm for the matching process. The resulting transformation parameters were then used to align the subsequent scans into the same reference frames as the baseline scans. The RMS of the normal distances was evaluated to quantify the quality of the registration. A RMS distance around the image noise level (i.e., image pixel size: 0.3125 mm) would indicate satisfying registration results. Changes in the RMS distances were used to compare the registration between the two subject groups (first hypothesis), and to evaluate the effects of different surface types and digitization techniques (second and third hypotheses).

To select and calculate the cartilage volume, a custom supervised algorithm written in MATLAB (The Mathworks, Inc., Natick, MA, version 6) was used. With this algorithm, a roughly defined region of interest (ROI) was drawn to enclose the medial tibial cartilage for each sagittal image slice of the baseline scan (Figure 7-3a), with extra care paid to select the junction between the tibial and femoral cartilage. The cartilage selection process took approximately eight minutes for a trained user. Since the subsequent scans were aligned to the baseline scans after registration, the same ROIs selected based on the baseline scans could then be automatically transferred to the

subsequent scans without any re-measuring. Smoothing and intensity enhancement were then applied to the images to improve the contrast between the cartilage and surrounding tissues (Figure 7-3b). Based on Otsu's method (1979), an automatically calculated optimal threshold was applied to select the cartilage voxels within the ROIs (Figure 7-3c), and the volume of the cartilage was calculated by summing all the voxels. The cartilage volumes obtained for each patient were compared by computing the mean and standard deviations (SD) of the difference in volume between scans. The coefficient of variation (CoV) was also computed to evaluate the inter-scan reliability (fourth hypothesis). The CoV is defined as the ratio of the standard deviation to the mean value. The differences in the cartilage volume changes caused by the use of different digitization techniques were evaluated for the third hypothesis.

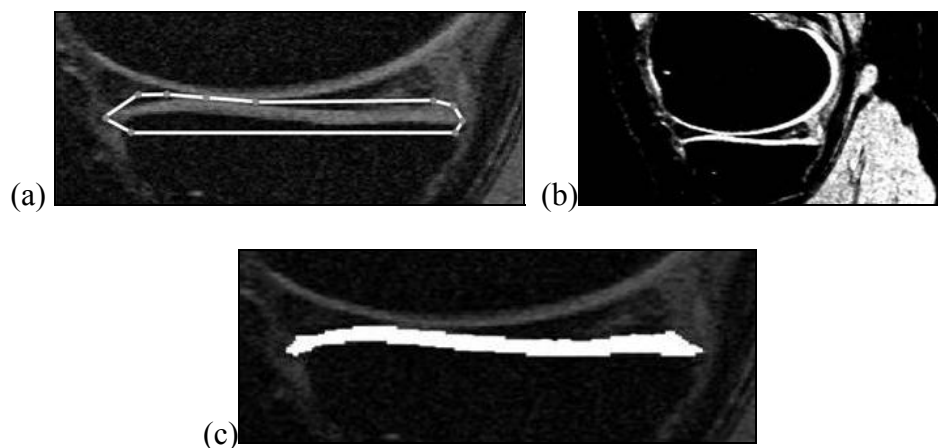


Figure 7-3: ROI selected to enclose tibial cartilage (a); image enhancement applied to increase cartilage contrast (b); automatic thresholding selected cartilage voxels within the ROI (c).

7.2.3 Results and Discussion

The registration of the tibial surfaces of both healthy subjects and OA patients were successful, and the results with cartilage volume changes are summarized in Table 7-2 and Table 7-3. The average RMS distance for the nine normal subjects was 0.121 ± 0.003 mm (mean \pm SD), with a coefficient of variation (CoV) of 2.6%. For the OA patients, even in the presence of osteophytes, the registration produced highly fitted tibial surfaces (0.122 ± 0.004 mm, CoV = 3.2%). These results indicate that the surface matching algorithm can allow good registrations (RMS distance \approx 1/3 of a pixel size) for both healthy knees and knees with OA using the intercondylar eminence surfaces, thus confirmed the first hypothesis. Changes such as the growth of osteophyte that are important for clinical diagnostic purposes were reliably detected. These were subsequently excluded by the algorithm, thus allowing accurate registration of OA knee surfaces.

Table 7-2: Tibial surface registration results and medial tibial cartilage volume changes for the nine healthy subjects.

Subject	RMS Distance (mm)	Volumes (mm ³)			Volume Difference*
		Time 1	Time 2	Mean	
N1	0.120	3297	3479	3388	5.4%
N2	0.120	1920	1967	1943	2.4%
N3	0.125	2187	2117	2152	-3.3%
N4	0.122	2038	2062	2050	1.2%
N5	0.125	2068	2085	2076	0.9%
N6	0.120	2453	2393	2423	-2.5%
N7	0.117	1736	1836	1786	5.6%
N8	0.124	1124	1166	1145	3.7%
N9	0.117	1896	1881	1889	-0.8%
Mean:	0.121			Mean:	1.4%
CoV:	2.6%			CoV:	3.2%

* Volume difference as a percentage of the mean volume

Table 7-3: Tibial surface registration results and medial tibial cartilage volume changes for the OA patients.

Subject	Scans (with scan 1 as a reference)	RMS Distance (mm)	Volume Difference*
OA1	2	0.127	-1.9%
	3	0.117	4.9%
	4	0.125	-4.8%
OA2	2	0.125	-22.2%
	3	0.125	-9.6%
	4	0.117	-21.0%
OA3	2	0.121	20.6%
	3	0.119	10.3%
	4	0.119	16.6%
	Mean:	0.122	
	CoV:	3.2%	
* Volume difference as a percentage of the mean volume with the first scan as the reference scan.			

The entire tibial surfaces for subjects N2, N5, and OA2 were registered, to evaluate the potential difference when a larger surface was used for matching (second hypothesis). The results indicated that using the intercondylar eminence has minimal effect, increasing the average RMS distance from 0.122 mm to 0.127 mm (3.5%). These results confirm that using only the uniquely shaped intercondylar eminence is sufficient for registration. This enables a substantial reduction in digitization time, thus enabling a more feasible technique for widespread clinical application.

For the same three subjects, comparisons were made between manual digitization and the semi-automatic technique based on Canny edge detection (third hypothesis). The semi-automatic Canny technique reduced the digitization time from twenty minutes to seven

minutes. The RMS distances also improved on average by 0.06 mm (Table 7-4). Therefore, semi-automatic Canny edge detection can efficiently digitize bone surfaces from MR images for and produce accurate registration.

Table 7-4: The effects of digitization techniques on the registration and cartilage volume changes for normal and OA subjects.

Subject	Scans	RMS Distance (mm)		Cartilage Volume Changes			
		Manual	Canny	Manual		Canny	
				mm ³	%	mm ³	%
N2	1 & 2	0.120	0.110	46.8	2.4	22.2	1.1
N5	1 & 2	0.125	0.111	17.8	0.9	8.5	0.4
OA2	2 & 4	0.129	0.125	-53.7	-4.1	14.3	1.2

Cartilage volumes obtained for the temporal scans were compared by computing both in absolute terms and as a percentage relative to the mean volume for all the scans. For the nine healthy subjects, the cartilage volume remained relatively unchanged over the two week interval (Table 7-2) with an inter-scan variation of $1.4 \pm 3.2\%$, (i.e. inter-scan CoV of 3.2%). Small cartilage volume differences were expected for subjects with healthy knee over a two-week time interval. These results were similar to other published studies (e.g., Raynauld et al., 2003, Cicuttini et al., 2004), thus the fourth hypothesis was confirmed. For the OA patients, large variations were found in cartilage volume between the three subjects (Table 7-3). These variations were speculated to be attributed to blinded therapeutic effects from the clinical trials and difficulties with selecting the thin tibial cartilage of OA knees. The increase in the volume for OA3 was probably caused by inclusion of femoral cartilage in the selected regions of interest.

To determine the effect registration had on the volume calculations, cartilage volumes obtained based on the registration using manual digitization and Canny edge detection were compared to test the third hypothesis (Table 7-4). This comparison revealed that a difference in 0.01 mm RMS distance from the registration resulted in less than 2% change in cartilage volume for healthy subjects. However, for the OA patient, a small RMS distance difference of 0.004 mm led to a 5% change in the cartilage volume measurement. This could be due to partial volume artifact where the largest effects could be found at edges of the cartilage. For the thin cartilage of the OA patients, a large proportion of the cartilage voxels were located at the edges. Further investigations are needed to truly understand the effects that digitization and registration have on the cartilage volume measurements with MRI for both healthy and OA patients.

The proposed methods for cartilage volume measurement based on registration with tibial surfaces digitized using the semi-automatic technique required approximately 22 minutes of user supervision for a pair of temporal MR scans (seven minutes for surface digitization for each scan and eight minutes for ROI selection on baseline scan). This is an improvement over other existing techniques that require over an hour in processing time (Eckstein et al., 2004, Glaser et al., 2003, Raynauld et al., 2003).

To conclude, the results showed that the surface matching algorithm can successfully register temporal MR datasets of both healthy knees and knees with OA with using only a small portion of the tibial surface. Differences in the surface digitization technique

resulted only in small differences in the registration and cartilage volume results for the normal subjects. The proposed technique required a short processing time and the inter-scan reliability of cartilage volume measurement was found to be comparable to other studies. With successfully registered tibial surfaces, cartilage volumes were automatically measured on the temporal scans within the same regions selected on the baseline scans, resulting in an efficient approach. With more testing of healthy and OA patients, and further refinements of the algorithms, the proposed methods can ultimately be adapted in a clinical setting to detect cartilage loss and to determine the disease stage and rate of progression, which can lead to more effective therapeutic interventions for treatment of OA.

7.3 Patellar Tracking

In order to understand the relationship of joint injuries and the development of OA, joint biomechanics have to be studied to understand the effects injuries have on the joints. For the patellofemoral joint, the tracking of the patella during knee flexion and the contact mechanics between the patella and the femur should be studied to help understand the effects injuries and disorders such as patellofemoral pain syndrome have on the biomechanics of joint. This application used the transformation parameters derived from the surface matching algorithm to directly and quantitatively track the relative movements of the patella with respect to the femur during knee flexion. This approach enabled the patellar movements between flexion angles to be quantified in terms of three

rotations and three translations, relative to a reference position. This quantification will enable comparison with in-vitro patellofemoral studies using similar measures to quantify patellar tracking throughout a range of knee flexion.

7.3.1 Data

The dataset of the four female subjects (Subject 2 to 5) acquired by the 3-telsa MR unit (refer to section 5.2) was also used for this application. To summarize, the subjects had no known knee problems, and MR scans were acquired with the knees positioned at different flexion angles and under physiologic loading conditions. For this application, the sagittal scans at 15°, 30°, and 45° flexion were used (balanced SSFP sequence, TR = 17 ms, TE = 3 ms, and flip angle = 90°, 0.625 mm × 0.625 mm × 3.000 mm).

7.3.2 Methods

Anterior and distal portions of the femoral condyle and the patellar bone surfaces for each subject at each flexion angle were digitized using SliceOmatic, and resampled and modeled using the TPS algorithm (refer to sections 5.3 and 5.4 for details). To quantify the patellar movements, the femur at 15° flexion was used as the reference position. Therefore, the surface matching algorithm was first applied to align the femoral surfaces at 30° and 45° to the reference frame of 15° flexion, which resulted in two sets of transformation parameters (TF in Figure 7-4a) relating the femurs for each subject. These two sets of parameters were then applied to transform the patellar surfaces at 30°

and 45° flexions to the reference frame of the femur at 15° (Figure 7-4a). At this point, all the patellar surfaces were given with respect to the 15° femoral reference frame (Figure 7-4b, Figure 7-5). To track the relative movements of the patella between flexion angles, the patellar surface at 15° was further registered to the transformed patellar surface at 30°, and the transformed 30° surface was registered to the one at 45° (Figure 7-4b). The two sets of transformation parameters (TPs in Figure 7-4b) were then used to directly quantify the relative changes in the 3D movements of the patella with respect to the femur during knee flexion. The scale factor was fixed at one for all the registrations as MR captured the true scale of the object.

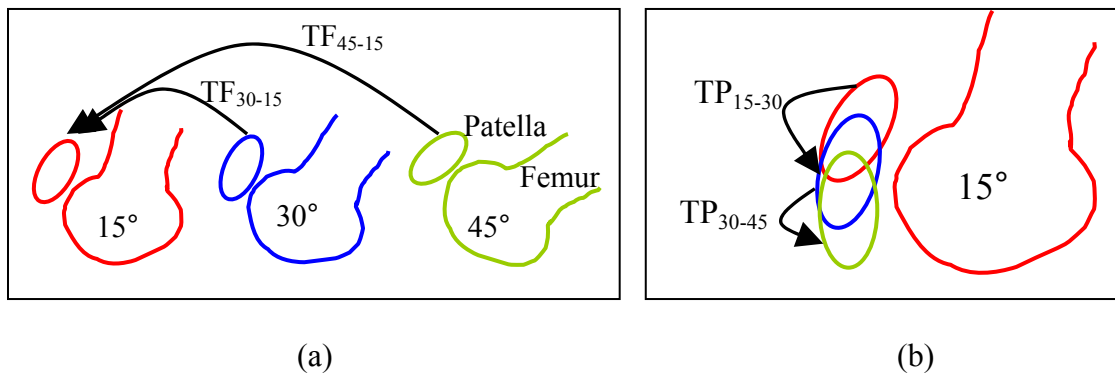


Figure 7-4: Patellar surfaces at 30° and 45° transformed to the reference frame of 15° femur, using transformation parameters (TF) derived from surface registration, which related the 45° and 30° femurs to the 15° femur (a). The patellar surface at 15° was registered to the transformed patellar surface at 30°, and the one at 30° was registered to the one at 45° (b). The resulting parameters (TP) were used to quantify the patellar movement with respect to the 15° femur (b).

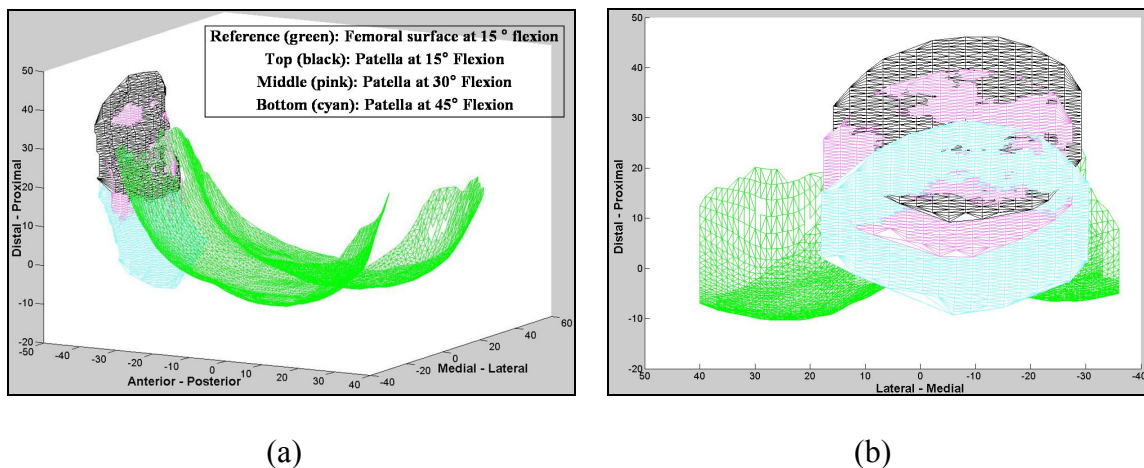


Figure 7-5: Patellar surfaces at different flexion angles with respect to the reference frame of the femoral surface at 15° flexion (3D view (a), 2D front view(b)) (units are in millimeters).

Four of the transformation parameters (Y_T , ω , φ , and κ) were related to the patellar tracking system and terminologies established by van Kampen and Huiskes (1990) (Figure 7-6). Y_T described the patellar shift, ω represented the tilt, φ represented the patellar flexion, and κ described the rotation. The X_T and Z_T parameters provided information about the proximal-distal and posterior-anterior translations of the patella during flexion, which were not reported by van Kampen and Huiskes (1990).

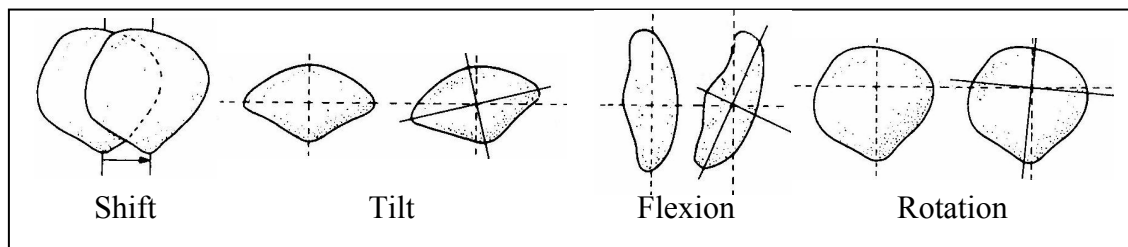


Figure 7-6: Patellar tracking system adapted from van Kampen and Huiskes (1990).

7.3.3 Results and Discussion

The registrations with the proposed algorithm for the femoral surfaces were successful, with an average RMS distance of the eight registrations (two registrations per each subject) of 0.191 ± 0.010 mm (approximately 1/3 of the pixel size). Visual evaluation of a mosaic image formed after aligning two corresponding images from the 15° (reference) and 30° flexions also showed high quality of fit (Figure 7-7). For the patella registrations, the average RMS distance was 0.207 ± 0.006 mm. This slight increase in error may be attributed to the process of first transforming the patellae with parameters derived from the femoral registration, thus any error propagations would directly affect the patellar registration. Based on the accuracy validation results from the previous chapter, translations with magnitudes above the size of an MR image pixel (0.625 mm) were considered detectable patellar movements during flexion. For patellar tilt, flexion, and rotation, values with magnitudes above 1.4° were considered to be detectable. This was determined from the extent of the patellar surface and image pixel size (Figure 7-8).

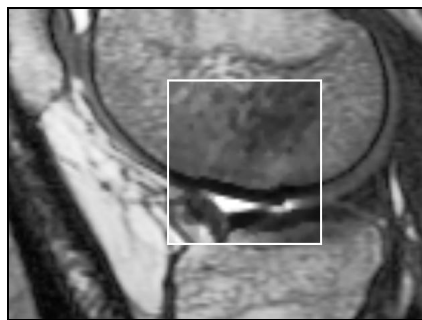


Figure 7-7: Mosaic shows a good match of the femur between the reference image (background, 15° flexion) and its corresponding image from the transformed dataset (foreground/small window, 30° flexion).

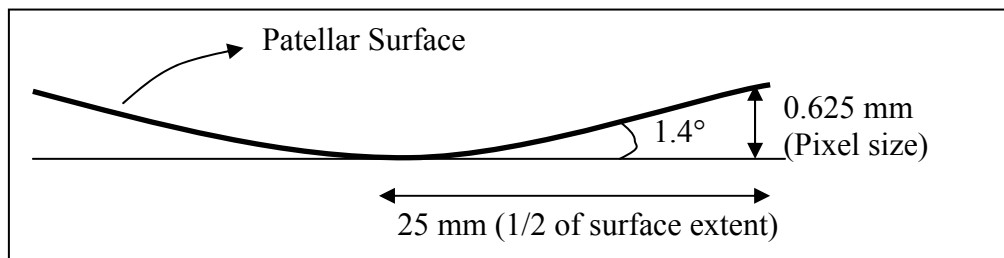


Figure 7-8: Detectable patellar translations and rotations based on the RMS distance from the registration.

The patellar tracking results are reported in Table 7-5 (15° to 30° flexion) and Table 7-6 (30° to 45° flexion). While variations in the tracking patterns were found among the four subjects, some trends can also be observed during flexion. First, the patella moved distally with respect to the femur for the four subjects as expected during knee flexion. Exceptions were found for subjects 4 and 5 where the patella moved proximally or remained in relatively the same location from 15° to 30° (Table 7-5). This result may reflect differences in the “seating” of the patella in the femoral groove between 15° to 30°, as reported by Fulkerson and Hungerford (1990). Medial-lateral shifts were observed for three subjects (S3, S4, and S5), with opposing directions between 15° to 30° and 30° to 45° of flexion for S4 and S5. This opposing trend was also reported by van Kampen and Huiskes (1990) based on cadaveric studies and by Patel et al. (2003) using MRI measurements. These results also show significant posterior translations (up to 11.7 mm) at higher flexion angles (Table 7-6). Posterior patellar translation is also anticipated, as the patella slides through the femoral groove with increasing knee flexion. The patellae tilted slightly both in the medial and lateral directions for subject 4. All subjects had significant superiorly anterior flexions (average of 12.4° for the four

subjects) from 30° to 45° of knee flexion. These results agreed with those reported by van Kampen and Huiskes (1990) and Patel et al. (2003). Small medial and lateral rotations were shown for three subjects with varying trends between them, as opposed to van Kampen and Huiskes' in-vitro results where consistent small medial rotations were found in three specimens while increasing gradually with increase in flexion angles. Conflicting results were reported by Patel and coworkers (2003), where consistent increase in lateral rotations during in-vivo knee flexion based on MR measurements was found. Clearly more research is required in this area to revoke these conflicting results and to determine the characteristic values and trends in tracking parameters to describe patellar movements. It is also important to note that the six transformation parameters are interrelated. Thus, it is crucial to analyze all six parameters to fully understand the 3D movement of the patella.

Table 7-5: Transformation parameters and relative patellar movements from 15° to 30° knee flexion.

		15° to 30°											
		Transformation Parameters											
		X _T (P-D)		Y _T (M-L Shift)		Z _T (Po-A)		ω (Tilt)		φ (Flexion)		κ (Rotation)	
Knee		(mm)	Dir.	(mm)	Dir.	(mm)	Dir.	(°)	Dir.	(°)	Dir.	(°)	Dir.
S2	Right	-5.088	D	-0.001	N	1.270	Po	1.076	N	0.830	N	-0.031	N
S3	Left	-4.115	D	2.515	M	-1.968	A	1.084	N	-3.543	Po	-4.084	L
S4	Left	3.617	P	-1.482	L	1.902	Po	1.570	M	5.511	A	-0.331	N
S5	Right	0.154	N	0.888	M	-0.053	N	-0.344	N	-1.294	N	1.529	M

Direction: P – Proximal; D – Distal; M – Medial; L – Lateral; Po – Posterior; A – Anterior; N – No Movement
 Patellar tracking system adapted from van Kampen and Huiskes (1990):

- Positive X_T, Y_T, and Z_T indicate proximal, medial, and posterior translations respectively
- Positive ω, φ, and κ indicate medial tilt, superiorly anterior flexion, and medial rotation respectively

Table 7-6: Transformation parameters and relative patellar movements from 30° to 45° knee flexion.

		30° to 45°											
		Transformation Parameters											
		X_T (P-D)		Y_T (M-L Shift)		Z_T (Po-A)		ω (Tilt)		ϕ (Flexion)		κ (Rotation)	
Knee		(mm)	Dir.	(mm)	Dir.	(mm)	Dir.	(°)	Dir.	(°)	Dir.	(°)	Dir.
S2	Right	-3.730	D	0.172	N	5.723	Po	0.587	N	9.837	A	-4.901	L
S3	Left	-8.622	D	-0.020	N	11.677	Po	-0.422	N	19.429	A	1.958	M
S4	Left	-3.474	D	1.157	M	4.698	Po	-3.517	L	11.541	A	-0.155	N
S5	Right	-4.714	D	-1.138	L	2.860	Po	-1.300	N	8.807	A	1.534	M

Direction: P – Proximal; D – Distal; M – Medial; L – Lateral; Po – Posterior; A – Anterior; N – No Movement

Patellar tracking system adapted from van Kampen and Huiskes (1990):

- Positive X_T , Y_T , and Z_T indicate proximal, medial, and posterior translations respectively
- Positive ω , ϕ , and κ indicate medial tilt, superiorly anterior flexion, and medial rotation respectively

Overall, this application demonstrated comparable patellar tracking results with other published works and has shown trends in the patellar movement during knee flexion. Compared to van Kampen and Huiskes' study (1990), this study provided additional results on proximal-distal and anterior-posterior translations of the patella based on the X_T and Z_T parameters. It also showed how registration with the proposed surface matching algorithm can be utilized to quantify in-vivo 3D patellar tracking pattern based on MRI. This tracking pattern can be used as a measure to identify abnormal patellofemoral kinematics and patellar malalignment, thus allowing further understanding of joint injuries and disorders, and the effects of surgical and therapeutic procedures. This can

provide further insights about the relationships between injuries, joint biomechanics, and the development of OA.

7.4 Changes in Contact Area Locations

In addition to the study of patellar tracking patterns, registration can also be applied to study the contact patterns between the patellar and femoral cartilage during knee flexion. The objective of this application is to demonstrate how the proposed algorithm can be applied to directly quantify the relative movements of the cartilage contact area on the patellar surfaces. By analyzing the patellofemoral contact mechanics, abnormal behavior may then be identified and thus help to understand the underlying causes of joint disorders and diseases.

7.4.1 Data

The same dataset used in the previous application was also used for this study. The images were obtained under physiologic loading conditions. Consequently, the patella should be “seated” within the femoral groove, in contact with the femoral cartilage. These loading conditions enable studies of the patellofemoral contact mechanics to be conducted.

7.4.2 Methods

The patellar and femoral bone and articulating cartilage surfaces (refer to section 5.3 and Figure 5-5) were used in this application. The proposed algorithm was applied to register the patellar bone surfaces at 30° and 45° flexions to the one at 15°. This approach yielded two sets of transformation parameters for each subject. Next, the patellar and femoral cartilage surfaces at 30° and 45° knee flexions were transformed using the above parameters so that they were given with respect to the patellar bone surfaces at 15° flexion.

To determine the contact regions between the patellar and femoral cartilage, the TPS algorithm was used to calculate the contact areas based on a proximity measure. Points on the cartilage surfaces were considered in contact if the normal distance, or a proximity value, projected at each surface point from the patellar cartilage surface onto the femoral cartilage surface was less than a predefined threshold (Baker, 2002). Although in the ideal case contact regions should have normal distances or proximity values of zeros, proximity measure has to be adapted to classify points of contact, due to MR distortions and partial volume effects, errors introduced by segmentation and surface modeling, and limitations with achievable image resolution. The upper and lower limits of the proximity threshold were set to be -1.4 mm and 1.4 mm, respectively (Baker, 2002). A negative proximity indicated a space between the two surfaces, while a positive proximity indicated overlapping surfaces. Based on this proximity approach, TPS was used to calculate the contact areas between the patellar and femoral cartilage, and to map

the areas onto the patellar cartilage surfaces. The centroids of the contact area were also calculated in the medial-lateral direction and in the proximal-distal direction (Figure 7-9). This 2D centroid was used to represent the location of the contact area, and its relative movements from 15° to 30° and 30° to 45° flexion was directly quantified since the surfaces were aligned to the same reference frame. Similar to previous application, a movement of the contact area centroid with a magnitude above the size of an image pixel (0.625 mm) was considered a detectable change.

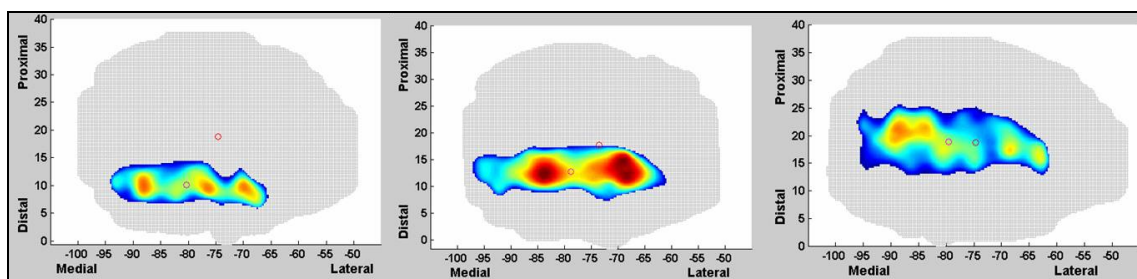


Figure 7-9: Cartilage contact areas (color maps) on the patellar surfaces at 15°, 30°, and 45° flexion after registering to the same reference frames for subject 2 (units are in millimeters).

7.4.3 Results and Discussion

Registration of the patellar bone surfaces at 30° and 45° flexion to the reference surface at 15° resulted in an average RMS distances for the four female subjects of 0.207 ± 0.009 mm. The results (Table 7-7) show that the contact area centroids moved proximally with respect to the patellar surfaces as the patellae moved distally with increasing flexion angles (more prominent from 30° to 45° flexion). The exceptions were at 15° to 30° flexion, where the contact area moved distally for subject 4 and no detectable movement was found for subject 5. These results directly reflect the tracking of the patella (Table 7-

5 and 7-6) for the four subjects as reported in the previous section. Connolly (2005), Ronsky (1994), and Patel et al. (2003) found the same patterns of contact area movements in the proximal-distal direction based on MR measurements. In the medial-lateral direction, the measured movements of contact areas were smaller, with subject 5 displaying a different pattern than the other three subjects. All subjects demonstrated medial-lateral contact area movements with opposing directions from 15° to 30° and from 30° to 45° knee flexions. Patel et al. (2003) also reported similar patterns for medial-lateral shifts of the cartilage contact areas. Importantly, the shifts, tilts, flexions, and rotations of the patella can all contribute to changes in contact locations on the patellar cartilage.

Table 7-7: Movements of contact area centroids from 15° to 30° flexions and from 30° to 45° flexions for four female subjects.

	Knee	15° to 30°				30° to 45°			
		Proximal-Distal		Medial-Lateral		Proximal-Distal		Medial-Lateral	
		Mag. (mm)	Dir.	Mag. (mm)	Dir.	Mag. (mm)	Dir.	Mag. (mm)	Dir.
S2	Right	2.808	P	1.527	L	5.996	P	0.834	M
S3	Left	2.213	P	1.432	L	7.895	P	0.646	M
S4	Left	1.198	D	1.797	L	4.073	P	1.023	M
S5	Right	0.085	No	0.651	M	3.469	P	1.600	L
Direction: P – Proximal; D – Distal; M – Medial; L – Lateral; N – No Movement									

This application showed how registration can be used for studies of the contact mechanics of the knee joint, thus providing further insights into the effects joint injuries and diseases have on the biomechanics of the joint. The suggested method for the detection of movement based on the quality of surface fit (i.e., RMS distance) is a reliable

and quantifiable approach that can be customized for different applications, reflecting the individual characteristics of each set of images, surface types, and registrations.

7.5 Summary

The proposed surface matching algorithm was used in three applications to demonstrate its feasibility for in-vivo studies of joint biomechanics and joint health status. The first application showed that with accurate registration, cartilage volume can be rapidly measured for multiple temporal scans to allow monitoring of OA progression. The surface matching algorithm was then applied for patellar tracking to help understand joint kinematics during knee flexions. This application showed that the six transformation parameters can directly quantify 3D patellar movements. Registered patellar surfaces were also used to measure relative changes in cartilage contact area locations at different flexion angles. The results from these applications not only verified that the proposed algorithm can accurately register joint surfaces generated from MR data, but further confirmed that registration can provide significant benefits for in-vivo study of joint injuries as it allows direct measurements and comparisons of joint properties.

Chapter Eight: Conclusions and Future Work

8.1 Conclusions

The knee joint is the largest and most complex joint of the human body, thus joint injuries and diseases are very common and can significantly affect patients' quality of life. Specifically, OA, a degenerative joint disease, is associated with many risk factors but the exact pathology is unknown. Therefore, to increase understanding of OA, quantitative assessments of joint properties and biomechanics, as well as monitoring of disease progression are needed.

Many techniques such as photogrammetry and radiography have been used to study joint properties. Among them, MRI has emerged as a safe, flexible, and non-invasive medical imaging technique that can allow accurate measurements of joint properties with high data resolution. Since the subject can be positioned differently and anatomical changes occur over time, registration, a process to align datasets, is a necessary procedure for the analysis and direct comparison of MR data. This research aimed at developing a registration technique based on matching knee joint surfaces generated from MRI to help with the in-vivo quantitative assessments of joint biomechanics and joint health status. A novel approach was introduced to translate techniques originally developed in the field of

Geomatics engineering for biomedical applications. The research objective was reached with four specific aims:

SA1) Investigate whether the proposed surface matching algorithm can work with high density data in the presence of noise, implement necessary modifications, and perform verifications using Geomatics engineering applications.

SA2) Apply the modified surface matching algorithm to register 3D MR data of knee joint structures acquired at different positions and under different alignment and loading conditions.

SA3) Validate the registration accuracy obtained with the algorithm, and analyze the repeatability of the digitization and registration algorithm for matching knee joint surfaces generated from MR data.

SA4) Apply the modified surface matching algorithm to register 3D MR data of healthy and pathologic knees to aid in the in-vivo study of joint biomechanics and joint health status.

The proposed surface matching algorithm, originally developed by Habib et al. (2001) for geographic data, can simultaneously estimate the transformation parameters and establish correspondence between two surfaces. The registration paradigm is defined as follows for the proposed algorithm:

- 1) Primitives: points and triangular patches for the two surfaces
- 2) Transformation function: 3D similarity (rigid transformation with seven parameters: $X_T, Y_T, Z_T, \omega, \varphi, \kappa,$ and S)

- 3) Similarity measure: Coplanarity condition (corresponding point and patches are coplanar)
- 4) Matching strategy: MIHT (voting scheme to find the best estimates of the parameter and identify corresponding point and patch pairs)

The proposed algorithm can work with surfaces at any orientation and performs matching by minimizing normal distances between corresponding surface elements. It is also a robust algorithm as it performs local matching to identify and exclude discrepancies prior to the application of the least squares adjustment of the parameters. To describe quantitatively the quality of fit of the surfaces, a RMS of normal distance is derived from the matches after applying the estimated parameters.

With the first specific aim, results indicated that with high density data such as MRI, the proposed algorithm might not converge to a final solution. Therefore, the ICP algorithm was added to complement the MIHT approach and refine the convergence of the parameters. MIHT provides a set of good estimates to initialize the ICP algorithm. ICP then performs matching locally to establish correspondence and estimate the parameters by minimizing the summation of normal distances. This new modified algorithm was verified with high density 3D data collected using Geomatics engineering means (i.e., LIDAR, photogrammetry, and close-range laser scanning). The results demonstrated that the algorithm could successfully register high density data and identify discrepancies between two surfaces. The accuracy of the surface matching results was evaluated with

results based on linear features of the same data, and have found to be comparable. The modified algorithm also showed improvement over another registration technique for matching the close-range laser scanning views.

For SA2, the modified algorithm was applied for knee joint surfaces generated from MR images, to verify its feasibility for in-vivo assessments of joint conditions. Four female subjects with healthy knees were imaged with a 3T MRI unit and femoral condylar and patellar surfaces were manually digitized from the image slices. A Thin Plate Spline algorithm was employed for surface modeling and re-sampling. Registrations were then performed with the modified algorithm between identical joint surfaces (same scan), as well as surfaces captured at different positions (i.e., different flexion angles) and under different loading conditions (i.e., loading versus not-loading). The identical surfaces were correctly registered with RMS distances of 0.0 mm. High qualities of fit were also found between the co-registered surfaces at different positions with average RMS of normal distances of 0.217 mm and 0.207 mm between the femoral and patellar surfaces, respectively. The patellar surfaces produced better registration results due to their unique geometry formed by facets and ridges with varying orientation. Qualitative analysis confirmed the high quality for the registrations and was also justified for the identified non-matches. Although only the femoral condyles were used for the registration, a good alignment was shown for the other regions of the femurs.

The accuracy of the surface matching algorithm for registering MR imaged joint surfaces was validated by comparing the transformation results from surface matching with ones derived using fiducial markers. A porcine knee specimen was used for surface matching which was fixed in position relative to spherical markers that were filled with gadolinium solution. To compare the results, a box modeled by 3D points was transformed with each set of transformation parameters and the resulting locations (i.e., X, Y, and Z coordinates) of the box were compared. Although MR artifacts and distortions led to small errors in the marker measurements and representations, comparisons were made and indicated that the surface matching algorithm had an absolute accuracy of approximately a pixel size of the MR image. Repeatability studies were also performed for the manual digitization and the registration processes. Two MR scans (0° and 30° flexions) were digitized five times each and registrations were performed between each set of digitization (categories: 0° with 0° , 30° with 30° , 0° with 30°). A box modeled by 3D points was transformed with each set of the parameters and the coordinate differences of the points were computed. The root-mean-square errors of the coordinate differences in the range of 0.2 mm suggested the high repeatability of the digitization and registration processes. ANOVA statistical analyses were also conducted on the transformed coordinates of the box. The *p*-values suggested that the mean coordinates were statistically similar within each category, thus confirmed that the digitization and registration were repeatable.

The final specific aim was to apply the accurate and repeatable algorithm for applications of in-vivo studies of joint biomechanics and health status. The modified algorithm was

used in three applications: 1) registration of temporal data for monitoring of OA, 2) patellar tracking using the transformation parameters during knee flexion, and 3) change detections of patellofemoral cartilage contact locations. In the first application, tibial cartilage volumes were automatically calculated for temporal MR datasets after successful registrations of the tibial intercondylar eminence. Volume changes quantified for healthy subjects were comparable to other published results and this technique was shown to be more time-efficient than others.

In the second application, in-vivo 3D patellar tracking patterns were directly described by the six transformation parameters (three translations and three rotations) for four subjects during knee flexion. Registration was performed first for the femurs. Patellar surfaces were then transformed to the 15° femoral reference frame and relative patellar movements were described by registering the transformed patellar surfaces. Results demonstrated medial-lateral patellar movements during knee flexions, in agreement with ones based on cadaveric studies.

The last application detected migrations of the patellofemoral contact area locations on registered patellar surfaces for the four subjects. Contact areas were calculated using the Thin Plate Spline algorithm based on a proximity measure after transforming the patellar and femoral cartilage surfaces to the same reference frame. Centroids of the contact areas were used as a measure to quantify movement and results reflected favorably with the patellar tracking patterns. These applications showed that registration is an important

procedure for in-vivo studies of joint conditions and the proposed surface matching algorithm is feasible for these studies.

Overall, this research project is significant as it demonstrated how Geomatics engineering techniques can be applied to biomedical applications, as both fields work with similar form of spatial data and share similar problems for their applications. Also, this research shows that the surface matching algorithm, based on the MIHT and ICP approaches, can accurately register surfaces generated from MRI and be applied to applications for in-vivo studies of joint biomechanics and health status. This can lead to better diagnosis, monitoring, and treatments for OA, thus can also improve the quality of life for patients. Although this research only shows preliminary work and results, it provides convincing support that the proposed algorithm can be applied to a wide range of applications for not only studies of OA, but also to other areas in both the Geomatics and medical imaging fields.

8.2 Future Work

Since the speed or the efficiency of the proposed algorithm was not a concern of this research, the first proposal for future work is to improve the overall efficiency of the registration technique by applying the surface matching methodology in a coarse-to-fine strategy. This can be done by first using a generalized version of the surfaces (i.e., general shape of the surface without local topography) to derive approximate values for

the transformation parameters with the MIHT approach. The resulting parameter estimates can be further improved by restarting the process with less-generalized versions of the surfaces (i.e, higher sampling resolution with more details). This process would be repeated while increasing the resolution and reducing the MIHT iterations thus reducing the overall process time for the algorithm. Another similar approach to improve efficiency is to first use smaller regions of the surfaces (i.e., smaller number of points and patches) to derive parameter estimates with the MIHT algorithm. This can reduce the execution time for the MIHT, thus can significantly improve the overall efficiency. It is important to note that the surface regions should be representative of the entire surface topography to allow accurate estimation of the parameters. The ICP algorithm can then use these estimates and the entire surfaces of interest to efficiently solve for the transformation parameters and correspondences. By improving the efficiency of the proposed registration methodology, it can be extended for clinical applications and be adapted into other studies in the future.

Another future focus is to improve the surface digitization and modeling techniques. Manual digitization with SliceOmatic was mainly used in this research, and has shown to be repeatable and to produce accurate registration. Semi-automatic digitization techniques based on Non-Maxima Suppression was used for the spherical markers in the validation pilot study and the Canny edge detection were used for tibial surfaces acquired using 3D spoiled gradient-echo fat-saturated sequence. If the image contrast permits, semi-automatic digitization with minimal editing can reduce processing time and does

not require a well-trained operator. Therefore, for future applications, semi-automatic or automatic digitization techniques can be employed to improve efficiency of the proposed methodology, and can also become more clinically applicable. For surface modeling, the TPS algorithm was employed to resample and smooth the 3D surface data. As reviewed in section 2.4, the main limitation of the TPS is that it cannot work with surfaces that curve around more than 180° (i.e., same XY coordinates with different Z values), using the planar projection. That was why only the femoral condyles were used in this study, instead of the entire bone surfaces for registration. To overcome this limitation, a polar coordinate system can be adapted in TPS instead of the Cartesian coordinate system, so that surface points can be defined using radius and angle. Another solution is to use different algorithms or programs for the surface modeling procedures. Commercial software such as SolidWorks (SolidWorks Corporation, Concord, MA) and Pro/Engineer (Parametric Technology Corporation, Needham, MA) have 3D modeling capabilities and can produce surfaces as triangular meshes. These software have a significant learning curve and require training. However, the potential benefit associated with implementing alternate surface digitization is worth while to investigate for future applications. It is important to use modeling software that can provide surface characteristics (e.g., surface normals) such as the TPS algorithm so joint properties (e.g., cartilage thickness) can be directly derived for in-vivo studies of joint conditions.

The visualization of the registration results can also be improved for future extension of this research. The 3D figures of the co-registered surfaces in this research were

generated using MATLAB, which has limited capabilities in terms of 3D visualization. Also, the image mosaics were formed by re-sampling the transformed image set onto the image slice locations of the reference set, thus do not provide the most accurate representation of the results. For future works, 3D computer aided design models of the joint surfaces can be formed using software such as the Visualization Toolkit to provide a more visually pleasing representation of the results. This is also beneficial for applications in clinical setting. Animations or movies can also be created for applications such as patellar tracking so qualitative explanations of joint biomechanics can be offered during knee motions. This is particularly attractive for clinical practitioners and for diagnostic purposes.

Due to time constraints and the scope of this research, further investigations and studies to improve the accuracy validation approach and results were not performed. In the validation study, the fiducial markers were scanned together with the porcine knee specimen and have resulted in artifacts and noise, which have decreased the accuracy of marker digitization and the absolute orientation results. In the future, further investigations should be performed to quantify and compensate for these effects. To allow a true validation of the surface matching accuracy and the effects of imaging and processing procedures, a gold standard of the transformation parameters is needed. This can be obtained by precisely controlling and quantifying the movement (e.g., measured by the Coordinate Measurement Machine which has an accuracy up to 0.5 μm) of the specimen and markers between scans. This movement (e.g., shifts and rotations) can

then be decomposed into the six translational and rotational parameters of the 3D similarity transformation and act as the known truth. The assumption that MRI can capture objects at its true scale should be tested in the future. The repeatability study was based on the femoral bone surface. Thus, extensions to other joint structures are needed. In addition, inter-observer variability should also be tested for the digitization and registration approaches.

The final future recommendation is to expand the presented applications and apply the proposed surface matching algorithm to a wider range of applications. First of all, larger sample sizes should be included in the MR applications so that statistically supported findings can be made. For the study of cartilage volume changes for OA, more patients and a controlled experimental setup are needed to reduce the variability of the results. Also, a validation study is needed to analyze the accuracy of the registration approach for measuring cartilage volume using MRI. For the patellar tracking and contact area locations applications, both healthy subjects and subjects with knee disorders (e.g., PFPS) can be included so that comparisons can be made between groups and atypical tracking pattern and contact mechanics can potentially be identified based on the results. For the contact area location, the centroid is only a crude measure thus it might not be the most ideal measure to use. More investigations are needed to determine the best methods for representing contact area locations. The femoral geometry is also an important factor for the contact mechanics of the patellofemoral joint and should also be investigated in the future. In addition to these applications, the proposed surface matching algorithm can

also be applied for other studies such as determining hip implant movements and for other forms of 3D data such as optical imaging.

References

- Ahmed A.M., Burke D.L., and Yu A., "In-vitro measurement of static pressure distribution in synovial joints – part II: retropatellar surface," *Transactions of the ASME*, 105: 226-236, 1983.
- Altman R., Brandt K., Hochberg M., Moskowitz R., Bellamy N., Bloch D.A., et al., "Design and conduct of clinical trials in patients with osteoarthritis: recommendations from a task force of the Osteoarthritis Research Society. Results from a workshop," *Osteoarthritis and Cartilage*, 4(4): 217-243, 1996.
- Altman R.D., Fries J.F., Bloch D.A., Carstens J., Cooke T.D., and Genant H., "Radiographic assessment of progression in osteoarthritis," *Arthritis and Rheumatism*, 30(11): 1214-1215, 1987.
- Andriacchi T.P., Mundermann A., Smith R.L., Alexander E.J., Dyrby C.O., and Koo S., "A framework for the in vivo pathomechanics of osteoarthritis at the knee," *Annals of Biomedical Engineering*, 32(3):447-457, 2004.
- Ateshian G.A., Soslowsky L.J., and Mow V.C., "Quantitation of articular surface topography and cartilage thickness in knee joints using stereophotogrammetry," *Journal of Biomechanics*, 24: 761-776, 1991.
- Baker N.S., "In-vivo quantification of patellofemoral joint contact force using a mathematical model," *Master of Science Dissertation*, University of Calgary, Calgary, Canada, 2002.
- Bergevin R., Soucy M., Gagnon H., and Laurendeau D., "Towards a general multi-view registration technique," *IEEE Transactions on Pattern Analysis and Machine Intelligence*, 18(5): 540-547, 1996.
- Besl P. and McKay N., "A method for registration of 3-D shapes," *IEEE Transactions on Pattern Analysis and Machine Intelligence*, 14: 239-256, 1992.
- Boyd S.K., Ronsky J.L., Lichti D.D., Salkauskas D., and Chapman M.A., "Joint surface modeling with thin-plate splines," *Journal of Biomechanical Engineering*, 121: 525-532, 1999.
- Brown L.G., "A survey of image registration techniques," *ACM Computing Surveys*, 24 (4): 325-376, 1992.

Burgkart R., Glaser C., Hyhlik-Durr A., Englmeier K.-H., Reiser M., and Eckstein F., "Magnetic resonance imaging-based assessment of cartilage loss in severe osteoarthritis," *Arthritis and Rheumatism*, 44: 2072-2077, 2001.

Cheng R.W.T. and Habib A.F., "Stereo-photogrammetry for generating and matching facial models," *Machine Vision and Applications Journal*, 2006. (submitted)

Cheng R., Habib A., Frayne R., and Ronsky J., "Registration of knee joint surfaces for the in-vivo study of joint injuries based on magnetic resonance imaging," Proceeding of SPIE Conference on Medical Imaging, San Diego, USA, February 2006.

Cheng R.W.T., Jaremko J.L., Lambert R.G.W., Habib A.F., and Ronsky J.L., "Efficient MRI knee cartilage volume estimation via tibial plateau surface registration," Proceeding of the 52nd Annual Meeting of the Orthopaedic Research Society, Chicago, USA, March 2006.

Cheng R.W.T., Frayne R., Ronsky J.L., and Habib A.F., "Matching strategy for co-registration of surfaces acquired by magnetic resonance imaging," CD Proceeding of the International Geoscience and Remote Sensing Symposium, Seoul, Korea, July 2005.

Cicuttini F., Forbes A., Morris K., Darling S., Bailey M., and Stuckey S., "Gender differences in knee cartilage volume as measured by magnetic resonance imaging," *Osteoarthritis and Cartilage*, 7: 265-271, 1999.

Cicuttini F., Hankin J., Jones G., and Wluka A., "Comparison of conventional standing knee radiographs and magnetic resonance imaging in assessing progression of tibiofemoral joint osteoarthritis," *Osteoarthritis and Cartilage*, 13: 722-727, 2005.

Cicuttini F.M., Wluka A.E., Wang Y., and Stuckey S.L., "Longitudinal study of changes in tibial and femoral cartilage in knee osteoarthritis," *Arthritis and Rheumatism*, 50: 94-97, 2004.

Cohen Z.A., McCarthy D.M., Kwak S.D., Legrand P., Fogarasi F., Ciaccio E.J., and Ateshian G.A., "Knee cartilage topography, thickness, and contact areas from MRI: in-vitro calibration and in-vivo measurements," *Osteoarthritis and Cartilage*, 7: 95-109, 1999.

Connolly K., "In-vivo characterization of patellar tracking in normal and patellofemoral pain syndrome," *Master of Science Dissertation*, University of Calgary Press, Calgary, Canada, 2005.

D'Apuzzo N., "Measurement and modeling of human faces from multi images," *International Archives of Photogrammetry and Remote Sensing*, 34(5): 241-246, 2002.

Dieppe P.A., Cusshnaghan J., and Shepstone L., "The Bristol 'OA500' study: progression of osteoarthritis (OA) over 3 years and the relationship between clinical and radiographic changes at the knee joint," *Osteoarthritis and Cartilage*, 5: 87-97, 1997.

Disler D.G., Recht M.P., and McCauley T.R., "MR imaging of articular cartilage," *Skeletal Radiology*, 29: 367-377, 2000.

Ebner H. and Ohlhof T., "Utilization of ground control points for image orientation without point identification in image space," *The International Archives of Photogrammetry and Remote Sensing and Spatial Information Sciences*, 30(3/1): 206–211, 1994.

Eckstein F. and Glaser C., "Measuring cartilage morphology with quantitative magnetic resonance imaging," *Seminars in Musculoskeletal Radiology*, 8(4): 329-53, 2004.

Eckstein F., Heudorfer L., Fabert S.C., Burgkart R., Englmeier K.-H., and Reiser M., "Long-term and resegmentation precision of quantitative cartilage MR imaging (qMRI)," *Osteoarthritis and Cartilage*, 10: 922-928, 2002.

Eckstein F., Reiser M., Englmeier K.-H., and Putz R., "In vivo morphometry and functional analysis of human articular cartilage with quantitative magnetic resonance imaging – from image to data, from data to theory," *Anatomy and Embryology*, 203: 147-173, 2001.

Felson D.T., Lawrence R.C., Dieppe P.A., Hirsch R., Helmick C.G., Jordan J.M., et al., "Osteoarthritis: new insights – Part 1: The disease and its risk factors," *Annals of Internal Medicine*, 133(8): 635-646, 2000.

Felson D.T., McAlindon T.E., Anderson J.J., Naimark A., Weissman B.W., Allabadi P., et al., "Defining radiographic osteoarthritis for the whole knee," *Osteoarthritis and Cartilage*, 5: 241-250, 1997.

Fitzgibbon A., Pilu M., and Fishter R.B., "Direct least square fitting of ellipses," *IEEE Transactions on Pattern Analyses and Machine Intelligence*, 21(5): 476-480, 1999.

Fulkerson J.P. and Hungerford D.S., *Biomechanics of the Patellofemoral Joint, Disorders of the Patellofemoral Joint* (Eds. Fulkerson JP, Hungerford DS), Baltimore: Williams & Wilkins, 25-41, 1990.

Glaser C., Burgkart R., Kutschera A., Englmeier K.H., Reiser M., and Eckstein F. "Femoro-tibial cartilage metrics from coronal MR image data: technique, test-retest

reproducibility, and findings in osteoarthritis," *Magnetic Resonance in Medicine*, 50(6): 1229-1236, 2003.

Graichen H., Eisenhart-Rothe R.v., Vogal T., Englemeir K.-H., and Eckstein F., "Quantitative assessment of cartilage status in osteoarthritis by quantitative magnetic resonance imaging," *Arthritis and Rheumatism*, 50: 811-816, 2004.

Gruen A. and Akca D., "Least squares 3D surface matching," ASPRS 2005 Annual Conference "Geospatial Goes Global: From Your Neighborhood to the Whole Planet", Baltimore, Maryland, March 2005.

Guarnieri A., Pontin M., Pirotti F., and Vettore A., "Procedure automatiche per la modellazione 3D," Convegno Nazionale Sifet 2005, Mondello – Palermo, 29-30 Giugno, 1 Luglio.

Haacke, E.M., Brown R.W., Thompson M.R., and Venkatesan R., *Magnetic Resonance Imaging: Physical Principles and Sequence Design*, New York: John Wiley & Sons, Inc., Chapter 4, 59, 1999.

Habib A. and Al-Ruzouq R., "Semi-automatic registration of multi-source satellite imagery with varying geometric resolutions," *Photogrammetric Engineering and Remote Sensing*, 17(3): 325-332, 2005.

Habib A.F. and Alruzouq R.I., "Line-based modified iterated Hough transform for automatic registration of multi-source imagery," *Photogrammetric Record*, 19(105): 1-16, 2004.

Habib A., Cheng R., Frayne R., and Ronsky J., "Surface matching for automated registration of LIDAR and MR imagery," CD Proceeding of the Workshop Italy-Canada "3D Digital Imaging and Modeling: Applications of Heritage, Industry, Medicine and Land", Padua, Italy, May 2005.

Habib A., Cheng R., Kim E-M., Mitishita E., Frayne R., and Ronsky J., "Automatic surface matching for the registration of LIDAR data and MR imagery," *Electronics and Telecommunications Research Institute Journal*, 28(2): 162-174, 2006.

Habib A., Ghanma M., and Mitishita E., "Co-registration of photogrammetric and LIDAR data: methodology and case study," *Brazilian Journal of Cartography*, 56(1): 1-13, 2004.

Habib A., Ghanma M., Morgan M., and Al-Ruzouq R., "Photogrammetric and LIDAR data registration using linear features," *Journal of Photogrammetric Engineering and*

Remote Sensing, 71(6): 699-707, 2005.

Habib A. F., Lee Y., and Morgan M., "Surface matching and change detection using a modified Hough transformation for robust parameter estimation," *Photogrammetric Record*, 17(98): 303-315, 2001.

Habib A. and Morgan M., "Automatic calibration of low cost digital cameras," *Optical Engineering*, 42(4): 948-955, 2003a.

Habib A. and Morgan M., "Linear features in photogrammetry," *Geodetic Science Bulletin*, 9(1): 3-24, 2003b.

Hall S.J., *Basic Biomechanics*, Fourth Edition, New York: McGraw-Hill Companies, Inc., Chapter 8, 239-251, 2003.

Hemler P. F., Sumanaweera T. S., van den Elsen P. A., Napel S., and Adler J. R., "A versatile system for multimodality image fusion," *Journal of Image Guided Surgery*, 1: 35-45, 1995.

Hardy P.A., Newmark R., Liu Y.M., Meier D., Norris S., Piraino d.W., and Shah A., "The influence of the resolution and contrast on measuring the articular cartilage volume in magnetic resonance images," *Magnetic Resonance Imaging*, 18: 965-972, 2000.

Hargreaves B.A., Gold G.E., Beaulieu C.F., Vasanawala S.S., Nishimura D.G., and Pauly J.M., "Comparison of new sequences for high-resolution cartilage imaging," *Magnetic Resonance Imaging*, 49: 700-709, 2003.

Hefzy M.S., Jackson W.T., Saddemi S.R., and Hsieh Y.-F., "Effects of tibial rotations on patellar tracking and patello-femoral contact areas," *Journal of Biomedical Engineering*, 14: 329-343, 1992.

Holderbaum D., Haqqi T.M., and Moskowitz R.W., "Genetics and osteoarthritis," *Arthritis and Rheumatism*, 42(3): 397-405, 1999.

Jaremko J.L., Cheng R.W.T., Lambert R.G.W., Habib A.F., and Ronsky J.L., "Reliability of an efficient MRI-based method for estimation of knee cartilage volume using surface registration," *Osteoarthritis and Cartilage*, 2006. (accepted)

Johnson A.E. and Hebert M., "Using spin images for efficient object recognition in cluttered 3D scenes," *IEEE Transactions on Pattern Analysis and Machine Intelligence*, 21(5): 433-449, 1999.

- Koh T.J., Grabiner M.D., and De Swart R.J., "In vivo tracking of the human patella," *Journal of Biomechanics*, 25: 637-643, 1992.
- Lancaster P. and Salkauskas K., *Curve and Surface Fitting: An Introduction*, London: Academic Press, 1986.
- Laprade J. and Culham E., "Radiographic measures in subjects who are asymptomatic and subjects with patellofemoral pain syndrome," *Clinical Orthopaedics and Related Research*, 414: 172-182, 2003.
- Lee J.-B., Habib A.F., Yu K.-Y., and Kim Y.-I., "Segmentation and extraction of linear features for detecting discrepancies between LIDAR data strips," Proceeding of the International Geoscience and Remote Sensing Symposium, Seoul, Korea, July 2005.
- Maintz J. B. A., van den Elsen P. A., and Viergever M.A., "Comparison of edge-based and ridge-based registration of CT and MR brain images," *Medical Image Analysis*, 1: 151-161, 1996.
- Maintz J.B.A. and Viergever M.A., "A survey of medical image registration," *Medical Image Analysis*, 2(1): 1-36, 1998.
- Moro-oka T., Matsuda S., Hiromasa M., Ryuji N., Ken U., Tsutomu K., et al., "Patellar tracking and patellofemoral geometry in deep knee flexion," *Clinical Orthopaedics and Related Research*, 394: 161-168, 2002.
- Moss R., "Quantification of patellofemoral contact area using MR imaging: a validation and comparative study," *Master of Science Dissertation*, University of Calgary Press, Calgary, Canada, 2001.
- Nishimura D.G., *Principles of Magnetic Resonance Imaging*, Department of Electrical Engineering, Stanford University, 1996.
- Oakley S.P. and Lassere M.N., "A critical appraisal of quantitative arthroscopy as an outcome measure in osteoarthritis of the knee," *Seminars in Arthritis and Rheumatism*, 33(2): 83-105, 2003.
- Oakley S.P., Portek I., Szomor Z., Appleyard R.C., Ghosh P., Kirkham B.W., et al., "Arthroscopy – a potential "gold standard" for the diagnosis of the chondopathy of early osteoarthritis," *Osteoarthritis and Cartilage*, 13: 368-378, 2005.
- Otsu N., "A threshold selection method from gray-level histograms," *IEEE Transactions on Systems, Man, and Cybernetics*, 9(1): 62-66, 1979.

Patel V.V., Hall K., Ries M., Lindsey C., Ozhinsky E., Lu Y., and Majumdar S., "Magnetic resonance imaging of patellofemoral kinematics with weight-bearing," *Journal of Bone and Joint Surgery*, 85A: 2419-2424, 2003.

Periaswamy S. and Farid H., "Elastic registration in the presence of intensity variations," *IEEE Transactions on Medical Imaging*, 22(7): 865-874, 2003.

Postolov Y., Krupnik A., and McIntosh K., "Registration of airborne laser data to surfaces generated by photogrammetric means," *International Archives of Photogrammetry and Remote Sensing*, 32(3W14): 95-99, 1999.

Pullivelli A., "Low-cost digital cameras: calibration, stability analysis, and applications," *Master of Science Dissertation*, University of Calgary Press, Calgary, Canada, 2005.

Raynauld J.P., Kauffmann C., Beaudoin G., Berthiaume M.J., de Guise J.A., Bloch D.A., et al., "Reliability of a quantification imaging system using magnetic resonance images to measure cartilage thickness and volume in human normal and osteoarthritic knees," *Osteoarthritis and Cartilage*, 11: 351-60, 2003.

Rheinschmidt C., van den Bogert A.J., Nigg B.M., Lundberg A., and Murphy N., "Effect of skin movement on the analysis of skeletal knee joint motion during running," *Journal of Biomechanics*, 30: 729-732, 1997.

Ronsky J., "In-Vivo quantification of patellofemoral joint contact characteristics," *PhD Dissertation*, University of Calgary Press, Calgary, Canada, 1994.

Ronsky J.L., Boyd S.K., Lichti D.D., Chapman M.A., and Salkauskas K., "Precise measurement of cat patellofemoral joint geometry with multi-station digital photogrammetry," *ASME Journal of Biomechanical Engineering*, 121: 196-205, 1999.

Ronsky J.L., Hamel J., Canteenwalla Z., Lichti D., and Moss R., "Effects of the freeze-thaw cycle on the thickness and surface contours of articular cartilage," *Archives of Physiology and Biochemistry*, 108: 175, 2000.

Roos E.M., "Joint injury causes knee osteoarthritis in young adults," *Current Opinion in Rheumatology*, 17(2): 195-200, 2005.

Rouet J-M., Jacq J-J., and Roux C., "Genetic algorithms for a robust 3-D MR-CT registration," *IEEE Transactions on Information Technology in Biomedicine*, 4(2): 126-136, 2000.

Ruan C., "MRI artifacts: mechanism and control", Technical Report, 2003.

Sanden A. and Ronsky J.L., "Feature analysis for reconstruction of joint surfaces based on magnetic resonance," Undergraduate Student Research Project, University of Calgary, 2003.

Scarvell J.M., Smith P.N., Refshauge K.M., Galloway H.R., and Woods K.R., "Evaluation of a method to map tibiofemoral contact points in the normal knee using MRI," *Journal of Orthopaedic Research*, 22: 788-793, 2004.

Scheffler D. and Lehnhardt S., "Principles and applications of balanced SSFP techniques," *European Radiology*, 13: 2409-2418, 2003.

Stammler T., Eckstein F., Englmeier K.-H., and Reiser M., "Determination of 3D cartilage thickness data from MR imaging: computational method and reproducibility in the living," *Magnetic Resonance in Medicine*, 41: 529-536, 1999.

Stammler T., Hohe J., Englmeier K.-H., Reiser M., and Eckstein F., "Elastic registration of 3D cartilage surfaces from MR image data for detecting local changes in cartilage thickness," *Magnetic Resonance in Medicine*, 44: 592-601, 2000.

Stoller D.W., *Magnetic Resonance Imaging in Orthopaedics and Sports Medicine*, Second Edition, Philadelphia and New York: Lippincott-Raven Publishers, 1997.

Suh J.-S., Lee S.H., Jeong E.-K., and Kim D.-J., "Magnetic resonance imaging of articular cartilage," *European Radiology*, 11: 2015-2025, 2001.

Tennant S., Willians A., Vedi V., Kinmont C., Gedroyc W., and Hunt D.M., "Patellofemoral tracking in the weight-bearing knee: a study of asymptomatic volunteers utilizing dynamic magnetic resonance imaging: a preliminary report," *Knee Surgery, Sports Traumatology, Arthroscopy*, 9: 155-163, 2001.

Unknown, "American Society of Photogrammetry and Remote Sensing Guidelines Vertical Accuracy Reporting for Lidar Data V1.0", American Society of Photogrammetry and Remote Sensing, 1-20, 2004.

Unknown, "Anatomy of knee," The University of Chicago Hospitals, Retrieved on March 26, 2005, from <http://www.uchospitals.edu/online-library/library.php?content=P00044>.

Unknown, "Explaining spinal anatomy," San Diego Centre for Spinal Disorder, Retrieved on February 8, 2006, from <http://www.sandiego-spine.com/subject.php?pn=spinal-anatomy-024>.

Unknown, "Osteoarthritis," The Arthritis Society, Retrieved on January 29, 2006, from www.arthritis.ca.

Unknown, "The femur and the patella," Gray's Anatomy of the Human Body, Retrieved on February 8, 2006, from <http://education.yahoo.com/reference/gray/subjects/subject?id=60#i256>.

Unknown, "Understanding arthritis," Zimmer, Inc., Retrieved on March 21, 2006, from <http://www.zimmer-latinoamerica.com/z/ctl/op/global/action/1/id/379/template/PC/navid/777>.

Van De Graaff K.M. and Fox S.I., Concepts of Human Anatomy and Physiology, Second Edition, Dubuque and Iowa: WM. C. Brown Publishers, 1989.

van Kampen A. and Huiskes R., "The three-dimensional tracking pattern of the human patella," *Journal of Orthopaedic Research*, 8: 372-382, 1990.

Veress S.A., Lippert F.G., Hou M.C.Y., and Takamoto T., "Patellar tracking patterns measurement by analytical X-ray photogrammetry," *Journal of Biomechanics*, 12: 639-650, 1979.

Vignon E., Conrozier T., Piperno M., Richard S., Carrillon Y., and Fanino O., "Radiographic assessment of hip and knee osteoarthritis. Recommendations: recommended guidelines," *Osteoarthritis and Cartilage*, 7: 434-436, 1999.

Wehr A. and Lohr U., "Airborne laser scanning – an introduction and overview", *ISPRS Journal of Photogrammetry and Remote Sensing*, 54: 68-82, 1999.

Wluka A.E., Wolfe R., Davis S.R., Stuckey S., and Cicuttini F.M., "Tibial cartilage volume change in healthy postmenopausal women: a longitudinal study," *Annals of Rheumatic Diseases*, 63: 444-449, 2004.

Xia Y., "Magic-angle effect in magnetic resonance imaging of articular cartilage. A review," *Investigative Radiology*, 35(10): 602-621, 2000.

Zhang Z., "Iterative point matching for registration of free-form curves and surfaces," *International Journal of Computer Vision*, 13(2): 119-153, 1994.

Appendix A: Ethics Approval

The following two pages contain ethics approvals obtained for the study of patellofemoral pain syndrome (PFPS) by K. Connolly (previous name: K. McLaughlin).

The research described in this thesis employed the MR datasets acquired for this PFPS study.

Foothills Medical Centre
1403 29 Street NW
Calgary, Alberta, Canada T2N 2T9
website www.calgaryhealthregion.ca

Foothills Medical Centre

12 January 2004

Dr. Janet Ronsky
Faculty of Engineering
University of Calgary

Dear Dr. Ronsky:

Re: #17557 – Investigating Joint Contact Characteristics in Patients with Patellofemoral Pain Syndrome

Thank you for submitting an application regarding the above project for review by the Adult Research Committee of the Calgary Health Region (CHR). This will confirm that the committee has granted institutional approval for this project, **contingent on approval by the Conjoint Health Research Ethics Board.**

It is understood from your submission that your study will be entirely funded through external sources and that the CHR will be reimbursed for all research costs associated with this project if applicable. To facilitate a smooth startup of your project, please notify affected departments in the Region well in advance of your intent to initiate this study.

Please note that it is a requirement that you communicate in writing the study results to the CHR Adult Research Committee, and provide any copies of publications arising from the research as well as provide feedback regarding any problems encountered during the course of the study.

Please accept the committee's best wishes for success in your research.

Yours sincerely,



Elizabeth MacKay, MD
Acting Chair, Adult Research Committee

cc: Dr. P. Gu, Conjoint Health Research Ethics Board



FACULTY OF MEDICINE

Office of Medical Bioethics
 Heritage Medical Research Building/Rm 93
 Telephone: (403) 220-7990
 Fax: (403) 283-8524

2004-01-09

Dr. J.L. Ronsky
 Department of Mechanical Engineering
 University of Calgary
 MEB 405
 Calgary, Alberta

Dear Dr. Ronsky:

RE: Investigating Joint Contact Characteristics in Patients with Patellofemoral Pain Syndrome

Grant-ID: 17557

The above-named research project, the revised Consent Form, the questionnaires (PFPS), Subject Journal, Poster and Information letter (Potential Participants) have been granted ethical approval by the Conjoint Health Research Ethics Board (CHREB) of the Faculties of Medicine, Nursing and Kinesiology, University of Calgary, and the Affiliated Teaching Institutions. The Board conforms to the Tri-Council Guidelines, ICH Guidelines and amendments to regulations of the Food and Drug Act re clinical trials, including membership and requirements for a quorum.

The study continues to meet the requirements of the Health Information Act.

You and your co-investigators are not members of the CHREB and did not participate in review or voting on this study.

Please note that this approval is subject to the following conditions:

- (1) you must obtain approval from your appropriate institution where the research project will be conducted (if applicable);
- (2) a copy of the informed consent form must have been given to each research subject, if required for this study;
- (3) a Progress Report must be submitted in one year, 2005-01-09, containing the following information:
 - (i) the number of subjects recruited;
 - (ii) a description of any protocol modification;
 - (iii) any unusual and/or severe complications, adverse events or unanticipated problems involving risks to subjects or others, withdrawal of subjects from the research, or complaints about the research;
 - (iv) a summary of any recent literature, finding, or other relevant information, especially information about risks associated with the research;
 - (v) a copy of the current informed consent form;
 - (vi) the expected date of termination of this project;
- (4) a Final Report must be submitted at the termination of the project.

Please accept the Board's best wishes for success in your research.

Yours sincerely,

Christopher J. Doig, MD, MSc, FRCPC
 Chair, Conjoint Health Research Ethics Board

CJD/am

c.c. Adult Research Committee Dr. P. Gu (information) Research Services Ms. K. McLaughlin
 Office of Information & Privacy Commissioner

Appendix B: Subject Consent Form

The following consent form is provided in courtesy of K. Connolly for the research study of patellofemoral pain syndrome. MR images acquired of the subjects were used in this thesis research.

TITLE: Investigating Joint Contact Characteristics in Patients with Patellofemoral Pain Syndrome

INVESTIGATORS: Dr. Janet Ronsky, Kim McLaughlin
Clinical investigators: Dr. V. Lun, Dr. P. Wiley

This consent form is only part of the process of informed consent. It should give you the basic idea of what the research is about and what your participation will involve. If you would like more detail about something mentioned here, or information not included here, please ask. Take the time to read this carefully and to understand any accompanying information. You will receive a copy of this form.

BACKGROUND

Patellofemoral Pain Syndrome (PFPS) is a common disorder of the patellofemoral joint characterized by pain on the anterior aspect of the knee. Reports from different sports medicine clinics have shown that knee problems account for 23 to 31% of all injuries and complaints, where pain conditions related to the patellofemoral joint are the most common. It is difficult to define PFPS as patients experience variety of symptoms from PF joint with different levels of pain and physical impairment. The initial treatment plan often includes quadriceps strengthening and temporary activity modification. Physiotherapy involving strategic strengthening of the quadriceps through a six week training regime has proven to be effective, with roughly 60 to 80% of patients experiencing pain reduction after treatment.

One of the major contributing factors of PFPS is malalignment of the lower extremity and/or the patella. This may cause the patella to have unusual tracking patterns and in turn, changing the points of contact between the undersurface of the patella and the femur which causes pain. It is suspected that by strengthening the muscles, the tracking of the patella is altered which reduces pain. Results of this study will provide new knowledge regarding the differences occurring in patients before and after treatment with respect to patella tracking.

WHAT IS THE PURPOSE OF THE STUDY?

The main objective of this study is to observe the differences in patellofemoral joint contact characteristics before and after a quadriceps strengthening regime in patients who have been successful with treatment. In addition, comparisons will be made to healthy individuals who are free of knee pain.

WHAT WOULD I HAVE TO DO?

You will have a pre-study clinical assessment of knee joint function, conducted by either Dr. Victor Lun or Dr. Preston Wiley. The standard clinical assessment, including a typical radiograph (for subjects in the PFPS group only), will determine that PFPS is the suspected cause of knee pain and not some other pathology.

You will be requested to attend a magnetic resonance imaging (MRI) training session at the University of Calgary Health Science Center lasting approximately 1/2 hour. The purpose of this training session is to familiarize you with the set-up that will be used during the MR scans and to determine the level of force that can be comfortably maintained for approximately 2.5 minutes (the length of one scan for a given angle).

During the MRI training session, you will be requested to complete an electromyography (EMG) session which will last approximately 1 hour. Surface electrodes will be placed on your leg in three locations over the quadriceps and hamstring muscle groups to measure muscle activity. The skin in the area of electrode application will be shaved to remove hair and rubbed with alcohol to remove surface skin oil. You will be asked to perform a step-up/down task while muscle activity is recorded.

Following successful training in (2), you will complete various MRI scans conducted at the Seaman Family MR Research Centre. This will be on a separate day from the training session. You will lie on the knee flexion device, and the affected limb will be imaged once at 0°, 15°, and 30° of flexion. During the scan, you will be requested to maintain a submaximal contraction (the force determined in 2). A pair of instrumented goggles will be worn to give visual feedback so a constant force can be maintained. The time involved to complete the MRI study is approximately 1.5 hours.

You will be asked to follow an 8-week quadriceps muscle strengthening and stretching regime using a commonly assigned protocol for treatment of PFPS. A questionnaire regarding knee pain will be completed before and after treatment.

Steps 3 and 4 will be repeated after the physical training regime has been completed.

** If you are signing this consent form as part of the healthy group of subjects, you will complete steps 1-4. **

WHAT ARE THE RISKS?

MR imaging is non-invasive and there are no known health risks associated with MR imaging for participants who meet the inclusion criterion. You will be asked to lie on a narrow table which slides into a large tunnel-like tube within the scanner. There is no pain associated with MR imaging. The primary discomfort is the possible claustrophobic feeling that some experience from being inside the scanner. The machine produces loud thumping and humming noises during normal operation. Ear plugs will be given to you to reduce the noise. A technologist will observe you during the entire procedure and may be spoken to through an intercom in the scanner.

The EMG surface electrode application procedure may cause a slight stinging of the skin before the electrodes are applied. Your skin may be red for a short time after the electrodes are removed. There are no other risks associated with surface EMG testing.

During plain radiographs, exposure to x-rays will be maintained as low as reasonably achievable. Therefore, the risk associated with the radiograph portion of this study will be minimal.

ARE THERE ANY REPRODUCTIVE RISKS?

There are no reproductive risks associated with this study.

WILL I BENEFIT IF I TAKE PART?

If you agree to participate in this study there may or may not be a direct medical benefit to you. Your PFPS may be improved during the study but there is no guarantee that this research will help you. The information we get from this study may help us to provide better treatments in the future for patients with PFPS.

The benefits of the study to you include a detailed quantitative assessment of your patellofemoral joint contact in the affected limb before and after treatment. Study participants will be made aware of their individual assessments, as well as the overall findings of the study, as available.

DO I HAVE TO PARTICIPATE?

Subjects will agree to participate on a volunteer basis only. Participants may withdraw from the study at any time without jeopardizing their healthcare. To withdraw, contact either Dr. J. Ronsky or Kim McLaughlin to inform them of their decision.

WILL I BE PAID FOR PARTICIPATING, OR DO I HAVE TO PAY FOR ANYTHING?

No payment will be given for participating in the study. Participants will be reimbursed for expenses associated with parking at the University of Calgary Health Science Center.

WILL MY RECORDS BE KEPT PRIVATE?

Patient confidentiality will be maintained by referring to the participants as individual MRI study numbers only. The reference list to correlate participant names and MRI study numbers will be maintained confidentially by the principal investigator. The MRI study data will be transferred directly to digital tape, a backup copy obtained, and then removed from the main Seaman Family MR Research Centre database. Access to data will be limited to authorized individuals only (Dr. Ronsky and Kim McLaughlin), for assessment purposes. Upon completion of the study, all data files related to the study will be removed from the workstations and saved to CD. This data will be maintained by the principal investigator for a period of seven years. The information will be destroyed following a period of seven years.

IF I SUFFER A RESEARCH-RELATED INJURY, WILL I BE COMPENSATED?

In the event that you suffer injury as a result of participating in this research, no compensation will be provided to you by the University of Calgary, the Calgary Health Region or the Researchers. You still have all your legal rights. Nothing said in this consent form alters your right to seek damages.

SIGNATURES

Your signature on this form indicates that you have understood to your satisfaction the information regarding your participation in the research project and agree to participate as a subject. In no way does this waive your legal rights nor release the investigators, or involved institutions from their legal and professional responsibilities. You are free to withdraw from the study at any time without jeopardizing your health care. If you have further questions concerning matters related to this research, please contact:

Dr. Janet Ronsky: (403) 220-8134

If you have any questions concerning your rights as a possible participant in this research, please contact Pat Evans, Associate Director, Internal Awards, Research Services, University of Calgary, at 220-3782.

Participant's Name

Signature and Date

Investigator/Delegate's Name

Signature and Date

Witness' Name

Signature and Date

The University of Calgary Conjoint Health Research Ethics Board has approved this research study.

A signed copy of this consent form has been given to you to keep for your records and reference.